Charles University in Prague
Faculty of Science
Biochemistry Department

The Study of Model Membrane Systems, Proteins and Protein-Membrane Interactions Using Various Fluorescence Techniques

Ph.D. Thesis

Martin Štefl

Supervisor: Prof. RNDr. Jiří Hudeček, CSc.
Supervisor-consultant: Prof. Dr. Martin Hof, DSc.

Prague 2012

DECLARATION

I declare that I have worked independently under the supervision of Prof. RNDr. Jiří Hudeček, CSc. and Prof. Dr. Martin Hof, DSc. and all literature has been properly cited. This work or its substantional part has not been used to obtain another academic degree.

In Prague,.....

….....

Martin Štefl

ACKNOWLEDGEMENT

First, I would like to thank my parents and all my family for the support they were to me during my university studies. I am also much obliged to my brother Honza and grandmother Marta for text corrections.

I would like to express my thanks to Prof. Jiří Hudeček for having me as a PhD student and helping me with all the issues concerning PhD studies.

I would like deeply address my gratitude to Prof. Martin Hof for introducing me to the fluorescence and his laboratory. I highly appreciate friendly and inspiring atmosphere you are keeping in the laboratory. I would like also thank you, Martin, for your support in order to find the place and finances for my research fellowship.

Further I would like to thank Prof. David M. Jameson for giving me the opportunity to work in his group in such a nice place in the World. I am very grateful to you, Dave, for adopting and introducing me and Jana to Hawai'i.

I am not going to mention all the people here, but I really thank all of my colleagues here in Prague and in Honolulu for helping me with trying to find solutions to all the problems we were facing so many times.

I would like to express my deep love and respect to Jana.

Last I would like to acknowledge Grant Agency of Charles University (grant No. 3130/2011), Ministry of Education of the Czech Republic for a stipend and grant (LC06063) and to Specific University Research Project No. 33779266.

Table of Contents

Abstract Membrane rafts (also referred as nanodomains) are membrane structures responsible for many cell processes. Their characterization is challenging because of the transparency, dynamics and small size of those structures. Moreover, high variability of cells makes the study of membrane rafts even more complicated. In order to simplify the studies of membrane processes including the formation of those rafts often model membranes like Giant Unilamellar Vesicles (GUVs) and Supported Phospholipid Bilayers (SPBs) are used. In this Thesis new fluorescent tools for studying such membrane processes were developed, tested, or improved.

Specifically, the phasor plot, an approach applicable to the analysis of the fluorescence lifetime data, was theoretically and experimentally tested and afterwards applied to the characterization of the membrane nanodomains in GUVs. First, we introduced the phasor plots to the excitation state processes like solvent relaxation and Förster resonance energy transfer (FRET) in lipid vesicles. We also employed the phasor plots in protein-ligand interaction, protein folding and denaturation studies. Finally, the phasor plot analysis of FRET data in combination with Fluorescence Correlation Spectroscopy (FCS) was used in characterization of membrane nanodomains in terms of the size, mobility and mechanisms of formation. We succeeded for the first time to determine the size and dynamics of nanodomains in GUVs smaller than 20 nm in radius. Our findings allowed us to make general conclusion on the mechanism of raft formation. The lateral diffusion on SPBs of a weakly bound blood coagulation protein was the second membrane process being studied. By developing a 2-color z-scan FCS approach using pulsed interleaved excitation, we were able to simultaneously characterize this protein diffusion and lipid diffusion. Although the protein diffusion is about two times slower that the lipid diffusion, the lipid composition and protein concentration dependencies suggest that both processes are to some extend coupled.

1 List of abbreviations

τ_D^{app}	Apparent diffusion time
$\langle \boldsymbol{r}^2(t) \rangle$	Mean square displacement
A	Acceptor of fluorescence
a (T)	Area per lipid at a given temperature
a_0	Area per lipid molecule
ATP	Adenosin triphosphate
BLMs	Black Lipid Membranes
BODIPY	Boron –Dipyrrin fluorescence dye
c_s	Surface concentration of fluorescent molecules
CtxB	Cholera toxin subunit B
D	Donor of fluorescence
D	Diffusion coefficient
D_{eff}	Effective diffusion coefficient
DENS	2-Diethylamino-5-naphthalenesulfonic acid
DiD	1,1'-Dioctadecyl-3,3,3',3'-Tetramethylindodicarbocyanine Perchlorate
DiO	3,3'-Dioctadecyloxacarbocyanine Perchlorate
DOPC	1,2-dioleoyl-*sn*-glycero-3-phosphocholine
DOPS	1,2-dioleoyl-*sn*-glycero-3-phosphoserine
DPH	1,6-diphenyl-1,3,5-hexatriene
Δz	Relative position in the detection volume
E_a	Activation energy
EGFP	Enhanced Green Fluorescent Protein
ER	Endoplasmic Reticulum
f	Frictional coefficient
F	Frequency
FCS	Fluorescence Correlation Spectroscopy
F_d	Steady-state intensity obtained from donor
$F_d(uni)$	Intensity of donor when D/A are distributed uniformly in membrane
FLIM	Fluorescence Lifetime Imaging Microscopy
FRAP	Fluorescence Recovery After Photobleaching

$G(\tau)$	Autocorrelation function
GdHCl	Guanidin hydrochloride
g_i	Real coordinate of the phasor plot
GM1	Ganglioside GM1
GPI-	Glycosilphosphatidylinositol linked anchor
GPMVs	Giant Plasma Membrane Vesicles
GTP	Guanosine triphosphate
GUVs	Giant Unilamellar Vesicles
$I(0)$	Fluorescence intensity in time t=0
$I(t)$	Fluorescence intensity in time t
IAEDANS	5-((2-Iodoacetyl)-amino)naphthalene-1-sulfonic acid
ICS	Image Correlation Spectroscopy
k	Rate constant
K_a	Distribution constant of acceptor
k_B	Boltzmann constant
K_d	Distribution constant of donor/Dissociation constant
k_{nr}	Rate constant of non-radiative processes
k_r	Rate constant of radiative processes
λ	Excitation wavelength
L_d	Liquid disordered phase
LDL	Low Density Lipoprotein
L_o	Liquid ordered phase
MD	Molecular Dynamics
MSD	Mean Square Displacement
n	Refractive index
N	Particle number
N_0	Number of fluorescence particles in the beam waist
NBD	4-Chloro-7-Nitrobenz-2-Oxa-1,3-Diazole(4-Chloro-7-Nitrobenzofuran)
No	Number of measurements
PE	diacyl-*sn*-glycero-3-phosphosethanolamine
POPC	1-palmitoyl-2-oleoyl-*sn*-glycero-3-phosphocholine
Q	Quantum yield

Ras	Individual protein from Ras-protein family
RICS	Raster Image Correlation Spectroscopy
SD	Standard Deviation
s_i	Imaginary coordinate of the phasor plot
SPBs	Supported Phospholipid Bilayer
Sph	Bovine sphingomyelin
SPT	Single Particle Tracking
Src	Proto-oncogene tyrosine-protein kinase
SUVs	Small Unilamellar Vesicles
t	Time
τ	Fluorescence lifetime
T	Average fraction of fluorophores in triplet state
t_0	Intercept
τ_D	Diffusion time
TIR/FPPR	Total internal reflection with fluorescence pattern photobleaching recovery
Tmt	Miscibility transition temperature
τ_r	Fluorescence lifetime of the radiative processes
T_{r+nr}	Sum of radiative and non-radiative fluorescence lifetimes
τ_T	Intersystem corssing relaxation time
α	Anomalous exponent
η	Viscosity
ω	Spatial parameter of confocal volume

2 Introduction

Biological membranes play a crucial role in living organisms. The structural organization of biological membranes, which consists of a hydrophobic core and a hydrophilic surface, creates an extraordinary system and plays a part in the crucial role of maintaining a non-equilibrium state between the cell's extracellular and intracellular environment. Biological membranes also control the exchange of energy, ions, substrates, metabolites and also information between the intracellular and extracellular environment. In order to fulfil those roles, the membrane contains two lipid leaflets, the inner and outer leaflet, in which various proteins, protein complexes, membrane channels and membrane receptors are incorporated. Furthermore, membranes associate a wide variety of compounds essential for cellular processes. Phospholipids within the membrane are composed of long hydrophobic acyl chains (that fill the centre of the membrane) and smaller hydrophilic head groups, which are exposed to the cell cytosol or extracellular matrix. Since biological membranes are very complex systems, the ongoing investigation of the dynamics and interplay between all the components proves to be very difficult; nevertheless, it is very important to achieve a good understanding of all the involved processes.

The basic concept of the fluid mosaic model proposed by Singer and Nicolson [1] assumes randomly distributed components in the membrane, and thus a free diffusion within the plane of the membrane. However, recent studies have revealed that biological membranes are in fact not homogeneous but instead contain nanodomains (rafts), which differ in both protein and lipid composition as well as structural and dynamical properties [2-4]. This means that the examination of their structure is more complicated than previously expected. To enable defined biophysical studies of those membranes, two main types of membrane model systems have been introduced; Supported Phospholipid Bilayers (SPBs) and Giant Unilamellar Vesicles (GUVs). SPBs are very stable planar systems, prepared usually by the spreading of Small Unilamellar Vesicles (SUVs) on a hydrophilic surface such as mica or glass [5; 6]. On the other hand, GUVs represent free-standing bilayers of an approximately spherical shape with similar size as eukaryotic cells and are most commonly prepared by electroformation from dried lipid films [7-10].

The fluorescence seems to be a very suitable phenomenon in biological, biochemical and biophysical studies because of its high sensitivity and non-invasiveness. The parameters of typical fluorescence studies are fluorescence intensity, lifetime or anisotropy. When speaking about lateral mobility in the membranes, one of the most relevant dynamical parameters is their lateral diffusion coefficient *D*. It can be determined for lipids, proteins and other membrane associated molecules. The diffusion of proteins and lipids is affected by their interactions with the cytoskeleton and the presence of domains. As a result the dependence of lateral diffusion on lipid and protein composition of the membrane is in the focus of many researchers.

2.1 Keystones of biomembranes – lipids

For better understanding of biomembranes in terms of functioning and organization, chemical and physical properties, which are based on chemical structure of lipids, have to be considered. In general, lipids are organic molecules created from polar headgroup and hydrophobic acyl chains. In aqueous solution lipid self-assemble to structures (micelles, bicelles, bilayers, ….), where hydrophobic parts are hidden inside and hydrophilic headgroups interact with surrounding water molecules. This self-association of lipids is mainly driven by so called hydrophobic effect. The basic principle of such effect can be explained by thermodynamics. When considering one lipid molecule in aqueous solution, the hydrogen bonded water structure surrounds hydrophobic hydrocarbon lipid chain forming a highly organized cage. Self-associating of hydrophobic domains minimizes contact of the non-polar acyl chains' surface with aqueous solution and, thus, highly organized water molecules are relaxed via entropy driven process reaching minimum energy system. The polar headgroups interact with neighboring polar parts and water molecules form energetically stable system with hydrophobic core and hydrophilic surface [11].

There are three basic structural organizations, which result from hydrophobic effect and depend on chemical structure and conformation of involved lipids (Fig. 1). The most common in cell membranes is lipid (or phospholipid) bilayer with two parallel phospholipid leaflets. The lipids hydrophobic acyl chains are oriented inside and polar headgroups outside of the bilayer. Phospholipid bilayers are created from inverted cone shaped lipids, which by themselves are not so heavily present in the nature as lipid bilayers are. However, the presence of proteins in membranes (50%, in some cases up to 70%) favors the membrane organization towards the phospholipid bilayer structure. Second structural organizations are micelles, which are spherical structures composed of cylindrically shaped lipids structured in only one layer with polar headgroups exposed to the polar solvent. Last structural organization, cubical, has very high variability in geometrical structures and shapes of involved lipids. Cubical organization is very rare and there are only two cubic phases available in aqueous environment [12]. As mentioned above, biological membranes are organized into phospholipid bilayers hence my Thesis is focused on the characterization

of those bilayers.

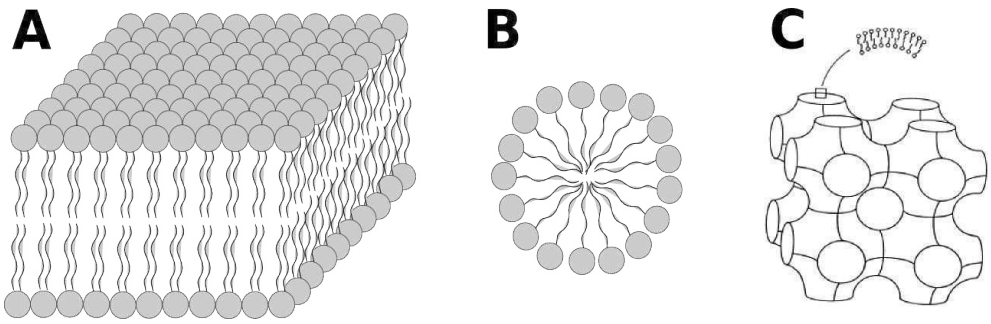

Figure 1 Schematic depiction of membrane polymorphism. Lipid bilayer is created from two lipid leaflets (A), micelles contain cylindrical shaped lipids with acyl chains hidden inside (the figure illustrates the cross-section of the sphere) (B) and cubic structure can form various membrane organizations depending on the solvent (C, taken from [13]).

The lipid organization gives the membrane its basic property, the impermeability for polar molecules. Differences in lipid headgroup region, however, are very important from the functional point of view. Moreover, saturation and unsaturation of acyl chains is a key factor for the rigidity of membranes. Saturated lipids form regions with lower rigidity because of lower hydrodynamic radius in axial plane and, thus, higher packing capability of lipids.

In plasma membranes, there are many different kinds of lipids (up to 600 [14]) which can be divided into three basic categories (Fig. 2): I) glycerophospholipids, II) sphingolipids and III) sterols. Shortly, the glycerophospholipids are lipids derived from the glycerol, where two hydroxyl groups are substituted by acyl chains of different length and degree of saturation, and third hydroxyl group is linked via phosphatidyl group with another polar molecule (e.g. ethanolamine, choline, serine). The sphingolipids are derivatives of sphingosine or ceramide, and mainly differ in the molecular composition of polar headgroup (e.g. choline, sugars). The sterols are highly hydrophobic planar structures with four hydrocarbon rings, and have great impact on membrane organization and subcompartmentalization.

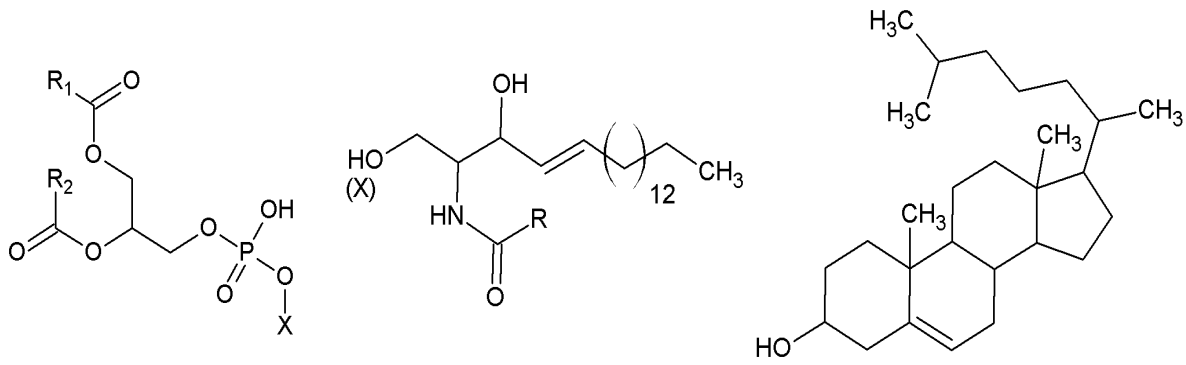

Figure 2 Chemical structures of general glycerophospholipid (left), ceramide or sphingolipids (middle) and cholesterol (right). R corresponds to acyl chains, X is any polar headgroup molecule.

High variability of lipids is a phenomenon very often discussed in the literature [15; 16]. It is believed that higher diversity in lipid composition makes the membrane more stable, robust and retains membrane impermeability even when pH, osmolarity or local composition are changed because of physiological or pathological events [17]. There is also difference in lipid representation between prokaryotes and eukaryotes. Prokaryote membranes contain mainly only phospholipids, no cholesterol [18], however there are few studies reporting about presence of another sterols in prokaryotic organisms as well [19].

2.2 Lipid rafts in membranes

2.2.1 Fluid Mosaic Model

When Singer and Nicolson [1] proposed their famous Fluid Mosaic Model (see Fig. 3) of the membrane in 1972, it was a revolution in membrane biology. Although this model was partially overcame, in some significant aspects is still valid. First, they stated that the membrane consists of two lipid leaflets (with fatty acyl chains oriented to the center of the membrane), in which considerable amount of proteins is incorporated (transmembrane, intrinsic, intergral proteins), and with which reasonable amount of proteins interact (peripheral, extrinsic proteins). These findings make the membrane very important and also interesting cell compartment in terms of signal transduction, molecule transport etc. Second, the authors emphasized lateral mobility of the whole system (lipids and proteins). The authors referred to the membrane as fluid system where the lipids and proteins move freely. Moreover, the localization of proteins within or on the membrane surface dramatically increases catalytic efficiencies of the membrane associated processes. Singer and Nicolson also mentioned transverse mobility of lipids and the lack of it in the case of proteins. Finally, the authors also discussed the surprising variability of lipid molecules within the membrane.

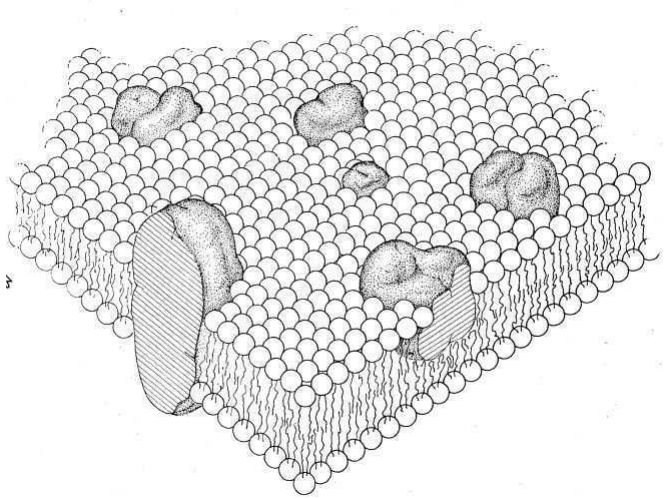

Figure 3 The Fluid Mosaic Model of the biological membrane proposed by Singer and Nicolson. According to this model the membrane is created from the lipid bilayer with hydrophobic core and hydrophilic surface and from the proteins incorporated to or in interaction with the membrane.

2.2.2 Membrane rafts

Although the Fluid Mosaic Model is accurate description of the membrane, it does not provide any information about hindered diffusion in the membrane and accumulation of some proteins and lipids in specific membrane regions. This fact has been observed and theoretically explained by the raft theory [2; 20]. The raft theory says that in a cell there are self-associating dynamic nano-scale regions with high accumulation of specific proteins and lipids [21] (Fig. 4). Dynamic raft structures have been mainly observed in the cell plasma membrane, however, there are studies reporting about the rafts presence in endosomal membrane as well [22]. It is clear that the rafts are sphingolipids (generally with saturated and longer hydrocarbon chains) and sterols dependent structures. Such lipid composition makes them more rigid in comparison to non-raft regions in the membrane [23]. Moreover, there has been found membrane asymmetry in lipid composition between the bilayer leaflets. Outer leaflet of the membrane is usually enriched in sphingolipids, whereas inner leaflet contains glycerolphospholipids with saturated acyl chains [24].

The structure and chemical characteristics of fatty-acid anchors are key factors for proteins associated with membrane rafts. For example glycosilphosphatidylinositol (GPI)-anchored proteins prefer localization in ordered domains (rafts) because of the saturation of their phosphoinositide anchors. Similarly, palmitoylated and myristoylated proteins partition to ordered domains (e.g. Src-family kinases). On the other hand, prenylated membrane anchors (Ras superfamily GTPases) partition preferentially to disordered structures (non-rafts) because their acyl chains contain unsaturated isoprenyl groups. Note that above mentioned preferences on the basis of saturation and unsaturation of the membrane anchors may be changed by the interaction with other proteins or hydrophilic headgroups. Transmembrane proteins partition to both, ordered and disordered domains. According to the literature, most of these proteins are supposed to be localized in disordered domains but there is considerable amount of transmembrane proteins associated with ordered domains, especially when these proteins are cross-linked [25]. The total number of membrane proteins associated with membrane rafts is about 35% but it should be pointed out that lipid-protein raft structure is very dynamic system where proteins are coming in and out of it.

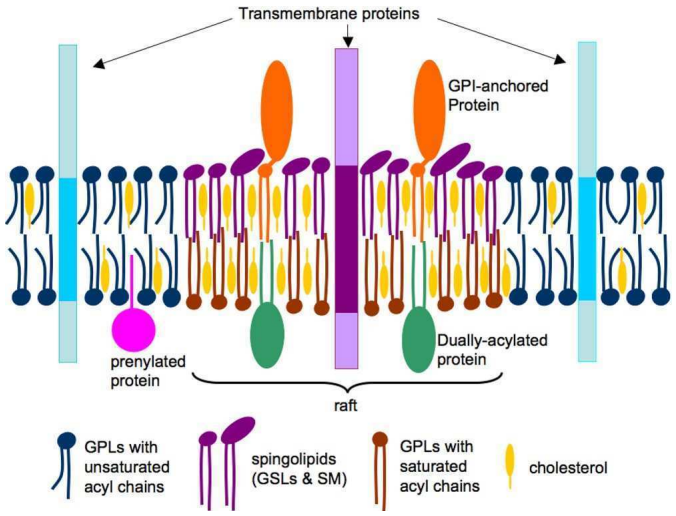

Figure 4 A simplified model of the membrane raft. The raft structures are enriched in sphingolipids, cholesterol and proteins. Adapted from [24].

2.2.3 Role of Cholesterol

One of the most interesting and controversial molecules in the nature is cholesterol (for chemical structure see Fig. 2, right). Depending on the organelle and cell type, cholesterol concentration usually varies between 20% to 50% but in ocular lens membrane can raise even up to 70%. Typical concentration in the plasma membrane is about 35%, which makes cholesterol very important molecule in membrane organization.

In living cells the cholesterol can be either biosynthesized or exported from outside of the cell. The biosynthesis of the cholesterol takes place on the interface between endoplasmic reticulum (ER) and cytoplasm and contains many steps. Transport of newly synthesized cholesterol molecules to targeted organelles is still not fully answered. It is believed that most of the cholesterol molecules are directly non-vesicularly transported to plasma membrane using cholesterol transport protein. Cholesterol molecule is hydrophobic and needs special protein carriers to be transferred, START family of transport proteins is one of known cholesterol-protein carriers [26]. The other way of cholesterol transport to the plasma membrane is from ER to Golgi and trans-Golgi and then using ATP-dependent vesicular transport directly to the plasma membrane [27]. Other major source of cholesterol is endocytic absorption of lipoproteins such as low-density lipoprotein (LDL) and hydrolysis of their cholesterol esters in late endosomes and lysosomes [28]. Final product is

a cholesterol molecule, which is transported to desired organelles using the mechanisms described above.

Due to its abundance the cholesterol fulfills many functions in living organisms. It is not only metabolic precursor to hormones and vitamins but it also provides mechanical strength to membranes and is an important agent in controlling of phase behavior of membranes. From the mechanistic side, cholesterol is responsible for increased mechanical strength, which reduces passive permeability of water as well as other small molecules and gases [29] and is capable to regulate membrane fluidity and phase behavior [30]. From the molecular point of view, cholesterol is important agent in regulation of so-called ordering and condensing effect. It has been reported that presence of cholesterol in model membranes composed of unsaturated phospholipids affects the mobility of such system; higher amount of cholesterol in the membranes decreases the membrane mobility (ordering effect). Table 1 shows our original Fluorescence Correlation Spectroscopy data (not published) for the membrane composed of POPC and various amount of cholesterol (from 0% up to 40%). One can see that 40 mol% of cholesterol slows down membrane diffusion to the half in comparison to the cholesterol-free membrane. On the other hand, when cholesterol is incorporated to the membranes which consist of saturated phospoholipids, the effect is totally opposite; higher amount of cholesterol increases fluidity of the membrane (condensing effect) [31]. As shown in Fig. 2, right, the cholesterol is composed of highly hydrophobic planar ring system, which makes the molecule rigid. Related to the localization of the cholesterol in the membrane, on one side of the ring system is hydroxyl group and on the other is hydrocarbon tail, which polarize whole molecule and give it preferential position in the membrane (with hydroxyl group oriented towards the bilayer headgroup region). Chemical characterization of interactions of the cholesterol molecule with surrounding lipids is still challenging and has been approached by molecular dynamic studies (MD studies) [32]. Rog et al. discuss in detail possible interactions of the cholesterol with saturated and unsaturated lipids but closer analysis is beyond the scope of my Thesis.

As already mentioned cholesterol is essential molecule in rafts formation. In fact, it is main molecular driving force to bring raft lipids together and stabilize them. The molecular dynamics found out that raft formation is long process from molecular point of

view with timescale longer than 200ns [33]. Very influential is the so called hydrophobic mismatch effect. The hydrophobic mismatch is the situation, where the hydrophobic profile of the proteins/rafts does not match to the hydrophobic thickness of surrounding bilayer. It is known that cholesterol modulates membrane thickness and stiffness and its effect depends on the lipid chain length and the level of unsaturation [34]. The cholesterol position in raft domains is mainly in the interface between raft/non-raft structures, which is supposed to balance hydrophobic mismatch between raft (thicker) and non-raft (thinner) structures. In other words, cholesterol compensates hydrophobic mismatch, which is very important in lipid-proteins (mostly transmembrane) coexistence. Presence of shorter transmembrane proteins in Golgi and longer transmembrane proteins in plasma membrane demonstrates effect of cholesterol on membrane thickness (cholesterol content in Golgi is just about 15-20% in comparison to 35% in plasma membrane).

Table 1 Lateral diffusion coefficients (*D*) in model membrane system (GUVs) composed of POPC and increasing amount of cholesterol (0-40mol%). The error is represented by standard deviation (*SD*), *No* stands for number of vesicles taken into consideration in statistic calculations.

	0% Chol	10% Chol	20% Chol	30% Chol	40% Chol
D [$\mu m^2 s^{-1}$]	10.79	9.81	7.29	6.27	5.18
SD [$\mu m^2 s^{-1}$]	1.12	0.68	0.74	0.21	0.33
No	7	6	10	10	10

2.3 Model membrane systems in relation to the membrane rafts

2.3.1 Model membrane characteristics

As already written, monitoring and characterization of membrane rafts (nanodomains) is very complicated. Moreover, cells and their membranes are very complex systems with thousands of "players" influencing their characteristics. Thus, quantification of membrane dynamics, lipid and protein partitioning and function in terms of biophysical and biochemical aspects is challenging. From that reason, simple model membrane systems simulating cell plasma membrane have been developed and intensively studied for last few decades.

We already mentioned high dynamic character of the membrane rafts (their formation and fading happens at one time), whereas the rafts' lifetime is still unknown. Because raft/non-raft interface is not clearly defined, membrane rafts cannot be considered as phases from thermodynamic point of view. In contrary, model membrane systems are stable and co-existence of two or more phases has been observed many times [35]. In general, we distinguish two main phases in model membranes, liquid disordered (L_d) or fluid phase and gel or solid phase, respectively. Both phases differ in membrane rigidity at certain temperature (Fig. 5) and every lipid is characterized by the temperature of the transition between liquid and gel phase (so called transition temperature). At room temperature, lipids which form fluid phase are usually unsaturated glycerophospholipids. Gel phase lipids are mainly saturated glycerophospholipids or sphingomyelins. When speaking about the gel phase, it has to be clearly stated that because of presence of cholesterol in living cells, the gel phase is irrelevant from biological point of view.

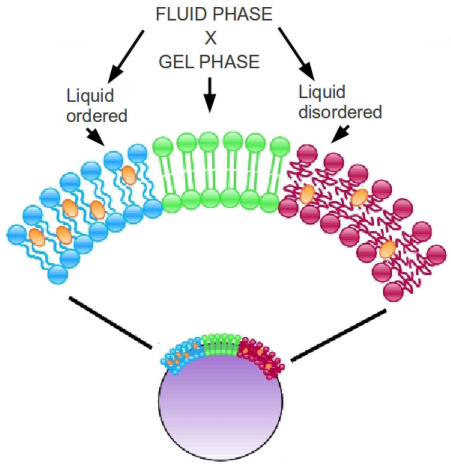

Figure 5 In model membrane system the gel phase is composed of saturated glycerophospholipids or sphingomyelins (green) and the liquid disordered phase is formed from lipids with unsaturated acyl chains (red). When adding cholesterol to gel phase, the fluidity of gel phase increases and such system is called liquid ordered phase (blue). Cholesterol is drawn as orange ovals.

The effect of cholesterol on cell membrane ordering has been in detail discussed in the cholesterol chapter (section 2.2.3). Cholesterol's biological relevance to model membranes is more than clear. When cholesterol is present in the membrane composed of "gel phase lipids", the rigidity of the membrane is dramatically decreased. Such membrane is subsequently called liquid ordered phase (L_o) and serves as model system in description of the membrane rafts as documented in the literature [36; 37]. The similarity between the liquid ordered phase and cell rafts is not only in lipid composition but also in proteins associated with both structures. Last publications revealed the similarity in size at certain lipid composition as well [38; 39].

A big advantage of model membranes is their simplicity and possibility to prepare membranes with desired lipid composition. Varying composition of three key lipids (e.g. DOPC, Cholesterol and Sphingomyelin) model membranes with L_o, L_d or with coexistence of L_o and L_d phases can be formed. Figure 6 shows phase diagram of those lipids with marked phase coexistence area. Note that the coexistence region corresponds to the phases, which are in size resolvable by conventional optical microscopes (>200 nm).

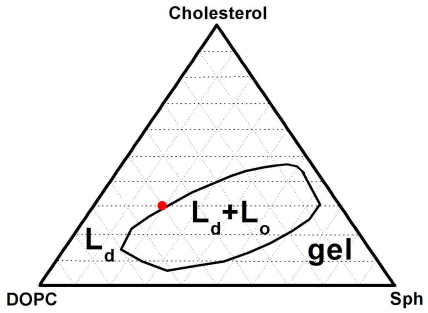

Figure 6 The phase diagram of DOPC, Sphingomyelin and Cholesterol. Marked area corresponds to the coexistence of liquid ordered and disordered phases, red dot represents lipid composition where presence of CtxB induces phase separation (see sections 2.4.2 and 4.2.2).

2.3.2 Model membrane systems

Supported Phospholipid Bilayers (SPBs) are one example of model membrane systems (Fig. 7A). These membranes are formed on solid supports, such as glass, mica, indium-tin oxide and many others. An advantage of such system is its simplicity in preparation and handling, high homogeneity of the membrane and reproducibility of results. A often discussed aspect in SPBs is the influence of the support on the membrane dynamics. First, it has been shown that support decreases membrane fluidity two times in comparison to free standing membranes, however, the difference in lateral mobility between inner and outer leaflets was refused because of strong leaflets coupling [40]. Second, the dynamics of plasma membrane in living cells are for sure affected by the cytoskeleton. Solid support in SPBs could be compared to some extend to the presence of the cytoskeleton, but to the best of our knowledge the relevance of this comparison has not been yet quantitatively discussed. Last, it has been shown that the presence of support influences formation of membrane domains, which makes SPBs a less favorable system for their study.

Nowadays, the most popular free standing model membrane system are so-called Giant Unilamelar Vesicles (GUVs). The size of such vesicles is in the range between micrometers up to tens of micrometers, thus, their size is comparable to that of cells. GUVs are an excellent system in terms of handling, stability and also preparation of the membranes with the coexistence of L_o and L_d phases (Fig. 7B). A main disadvantage is very

complicated and hardly reproducible preparation of GUVs in aqueous solutions with higher ionic strength.

As mentioned above, the membrane microscopic phase separation has never been observed in living cells. However, Baumgart et al. [41] showed that under certain non-physiological conditions microscopic phase separation can occur. The authors used formaldehyde membrane blebbing to generate Giant Plasma Membrane Vesicles (GPMVs), which separate L_o and L_d phases upon cooling as confirmed by typical L_o and L_d fluorescent markers in the membrane (Fig. 7C). This system is very similar to the GUVs, the difference is in presence of all plasma membrane components of the cell in the GPMVs.

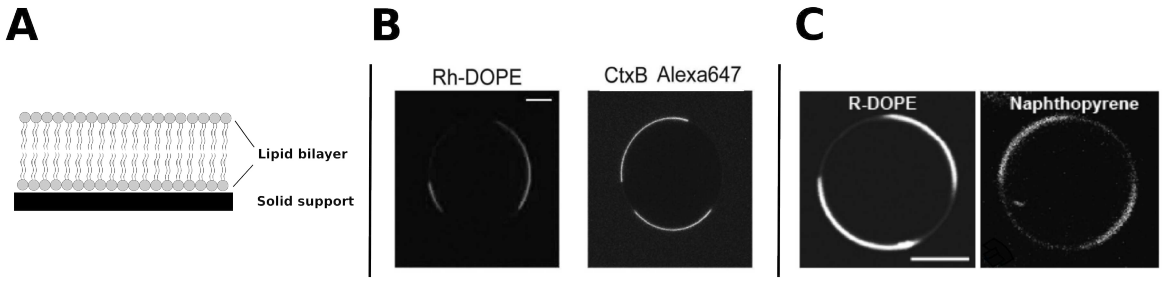

Figure 7 Supported phospholipid bilayers are non-covalently attached to the support (A) which influences lipid lateral mobility. Free standing model membranes giant unilamelar vesicles (B, from [42]) and giant plasma membrane vesicles (C, [41]) are best model systems for membrane separation studies. In this figure B and C liquid disordered phase is stained by Rh-DOPE and liquid ordered phase is labeled by CtxB-Alexa647 (B) and naphthopyrene (C), respectively. The scale bar is 10 μm.

In recent years another model systems have been developed. Briefly, very popular systems in ion channel studies are black lipid membranes (BLMs). Supported membranes on porous materials are used in phase coexistence research. The presence of pores gives rise to the support-free regions, which simulate free standing membranes.

Since there are always some disadvantages in all model membrane systems, one has to carefully consider those when using model membranes.

2.4 Visualization of lipid membranes by fluorescence – fluorescent lipid analogues

2.4.1 Fluorescent probes

Because of non-invasiveness and high sensitivity, fluorescence microscopy is a very useful group of methods in biological/biochemical/biophysical studies. On the other hand, fluorescence study of membrane rafts is still challenging due to low partitioning of fluorescence molecules into the rafts. There are many fluorescent labels applicable to membranes; membrane markers (perylene, rubicene, DiD, DiO,...) and fluorescence lipid analogues (BODIPY Ceramide, NBD-Cholesterol,…) but only a few prefers the localization inside liquid ordered phases (see Table 2, chemical structures in Fig. 8) [43]. Moreover, fluorescent analogues of raft lipids like sphingomyelin, ceramide or cholesterol surprisingly show very low partitioning to the liquid ordered phase in model membrane systems [44].

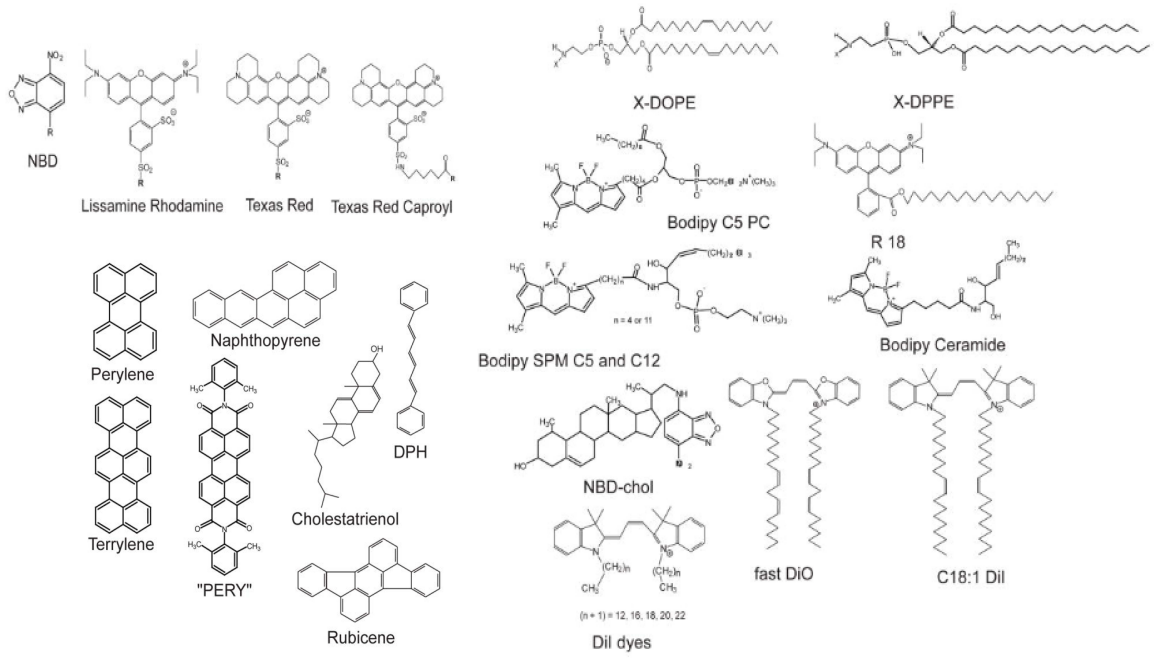

Figure 8 Chemical structures of selected fluorescence dyes usually used in model membrane visualization. Partitioning information are summarized in Table 2. Data adapted from [43].

Furthermore, increased degree of unsaturation and decreased lipid acyl chain length also favors L_d localization in comparison to L_o. Unfortunately, hydrophobic raft tracers like perylene form excited state dimers and higher polymers which are highly unsuitable for

lifetime measurements like fluorescence resonance energy transfer (FRET) or fluorescence lifetime imaging microscopy (FLIM).

Table 2 Partitioning preferences of typical membrane tracers in Sph/DOPC/cholesterol model membranes. Most of the dyes prefer liquid disordered phase but there are few localized in L_o or in both phases. X = NBD, Lissamine rhodamine. Y = Texas red, N-caproyl-Texas red. n = 5, 12. m = 12, 16, 18, 20, 22. Original data published in [43].

Fluorescent probe	Partitioning preference (= indicates no preference)
X-DOPE	L_d
DiI C18:1	L_d
Fast DiO	L_d
Bodipy PC	L_d
SPM C_n BODIPY	L_d
BODIPY Ceramide	L_d
X-DPPE	L_d
Y-DPPE	L_d
NBD-chol	L_d
Cholestatrienol	L_o
DiI C_m:0	L_d
Naphthopyrene	L_o
Perylene	=
Rubicene	=
Terrylene	L_o
DPH	=
“PERY”	L_d

2.4.2 Rafts/L_o protein fluorescent markers

Because of the low partitioning of those known fluorescence dyes to L_o phases, lipid-protein interactions have been utilized in order to visualize membrane rafts. A prominent example for that is the use of the protein cholera toxin subunit B, which unspecifically binds to ganglioside GM1 localized in the membranes. The cholera toxin (Ctx) is a 84kDa protein produced by bacteria Vibrio cholerae, which causes cholera

infection. It is composed of two subunits, a single copy of subunit A (28kDa) and five copies of subunit B (56kDa, CtxB). Only the subunit A is toxic and incorporates into the host cells. Five clones of subunit B form a pentamer and are responsible for recognition and highly specific interaction with 5 GM1 molecules in plasma membrane of host cells. The GM1-CtxB interaction is directly established between 2 GM1 saccharides (galactose and N-acetylglukosamine) and amino acid residues of cholera toxin subunit B (Trp88, Gly33 and Tyr12) [45].

Ganglioside GM1 consists of ceramide and oligosaccharide part and is believed to be localized mainly in rafts or L_o phases. When CtxB is fluorescently labeled, GM1-CtxB complex is a very useful raft marker. The preference of localization in the ordered phases is based on the stabilization of GM1 molecules by the presence of sphingomyelin and cholesterol molecules in its vicinity. As already mentioned, CtxB binds 5 GM1 molecules which forms clusters of stabilized structures consisted of GM1/Sph/Cholesterol molecules. Moreover, it has been reported in model membranes (GUVs) with certain lipid composition that CtxB binding to GM1 induces phase separation [35]. For the external triggering of a phase separation the lipid composition has to be very close to the phase boundary region as marked in Fig. 6 by a red dot. Note that according to Hammond et al. phase separation means the visual phase separation, thus, formation of phases with sizes larger than microscope optical resolution (>200nm), mainly micrometer-size phases [35]. Hammond et al. also discuss the influence of CtxB-GM1 binding on miscibility transition temperature (Tmt) of GUVs. Each lipid composition has its characteristic Tmt. Below this temperature the membrane is in phase coexistence and heating the system above Tmt makes phase coexistence disappear. They observed an ~6°C increase in Tmt temperatures when CtxB was added, which implicates that CtxB most probably does not only influence polar headgroups of lipids but partially also the hydrophobic acyl chains.

Beside of the protein-lipid interaction between CtxB and GM1, there are also other protein based markers of rafts and L_o phases. One of them is green fluorescent protein conjugated with GPI-anchored protein (GFP-GPI), which is localized in rafts [46]. Nevertheless, CtxB-GM1 remains certainly the most popular system in model membrane studies.

2.5 Membrane dynamics - lateral diffusion in membranes

According to the theory, the free Brownian lateral diffusion in a 2-dimensional system is described by the Einstein relation:

$$\langle r^2(t)\rangle = \langle (r(t) - r(0))^2 \rangle = 4\mathrm{Dt}, \quad (1)$$

where $\left\langle \boldsymbol{r}^2(t) \right\rangle$ is the mean square displacement (MSD), D is a constant called the lateral diffusion coefficient and t is the time. The process described above is driven only by thermal fluctuations around the equilibrium and so we should call it lateral self-diffusion and strictly distinguish it from lateral diffusion driven by concentration gradients [47; 48]. The phenomenological parameter D was in the focus from the beginning and several theories have been developed to relate it to the microscopic properties of diffusing molecules on and within the phospholipid bilayers. In the case of planar lipid membranes two distinct cases have been described, these cases depend on the size of the diffusing molecules in proportion to the size of the lipids (which are the basic building blocks of the membrane). The diffusion of molecules which are smaller or similar in size to the lipids is usually theoretically treated by free area theory [49; 50] based on a two-dimensional random walk. Every step of a molecule of this size is conditioned by the free area available for the molecule to move into and also by a minimal activation energy (E_a) required to perform the step. The total value of the activation energy is influenced by frictional coupling of lipids (one to each other), surrounding aqueous microenvironment and when speaking about Supported Phospholipid Bilayers (SPBs) by interaction of lipids with the solid surface (support). A theoretical model was derived which relates D to E_a, the area per lipid at a given temperature a (T) and also to the minimal cross-sectional area per lipid molecule a_0. Experimental determination of lipid areas a (T) and a_0 allows determination of E_a from temperature dependencies of D. Although the free area theory is rather simple, the good fits of experimental temperature dependencies of D with the theoretical model justify the assumptions involved in derivation of the model [49; 51]. More recent molecular dynamics simulations also proved the validity (at least qualitative) of the predictions of the free area theory [52]. An interesting prediction of the free area theory is that molecules occupying areas similar to lipids or smaller should diffuse with the same D (because a

diffusive step is completed by a lipid molecule filling the void left after the tracer molecule). This is naturally an oversimplification, since the collective fashion of membrane lipid movements allows faster filling of smaller voids, but we may at least assume that molecules similar in occupied area move all with the same *D* [50; 53].

The diffusion of molecules larger than lipids (e.g. peptides, proteins) is usually described as diffusion in viscous continuum [54; 55]. In this theory, the motion of diffusing molecules is driven by random, fluctuating forces provided by unbalanced collisions with the solvent molecules and is resisted by frictional forces inherent in viscous solvents [50]. The diffusion coefficient is defined as:

$$D = \frac{k_B T}{f}, \tag{2}$$

where k_B is the Boltzmann constant, T is the temperature and f is a frictional coefficient, which for a spherical particle of radius a in a medium of viscosity η equals to $f = 6\pi\eta a$. The resulting relation corresponds to the Stokes-Einstein equation:

$$D = \frac{k_B T}{6\pi\eta a}. \tag{3}$$

For the lateral diffusion of molecules with larger radii ($a > 10\,\text{Å}$) Eq. 3 has been extended by Saffman and Delbrück, where the thickness of the membrane is taken into account [56; 57].

It has been found by several studies that the description of diffusion in cellular membranes does not fully conform to the Eq. 1, but to its modification:

$$\langle r^2(t)\rangle = 4\mathrm{Dt}^{\alpha}, \tag{4}$$

where α is called the anomalous exponent and is limited by the interval [0;1]. The diffusion is referred to as anomalous (or sometimes anomalous subdiffusion) to indicate that smaller values of α correspond to slower diffusion. Theoretical studies have shown that the anomalous diffusion can be a result of a broad distribution of jump times, correlations between diffusing particles or multiple diffusion rates. Moreover, anomalous diffusion in cellular membranes has been explained by lipid-protein binding interactions and by hindrance of diffusion by impermeable obstacles (i.e. immobile proteins, lipid microdomains and the cytoskeleton) [47; 58-61]. Theoretical and experimental analysis of

diffusion in heterogeneous systems has revealed how the characteristic length-scale of the measurements ω and its relation to the characteristic size of the obstacles influence values obtained for diffusion coefficients [62-64]. Locally the tracer molecule may be able to diffuse freely. However, its diffusion is anomalous when probing a larger area ω. For yet larger values of ω, the diffusion satisfies again the Eq. 1, but with a lower value of D than in the absence of hindrance. With an increasing fraction of the area occupied by the obstacles, ω at which the transition to normal diffusion occurs is shifted to larger values [61; 62]. When the effects of mobile and immobile obstacles are compared, the influence of mobile obstacles is less pronounced [47; 65].

2.6 Fluorescent techniques used in membrane characterization

2.6.1 Fluorescence

Fluorescence [66] is one of luminiscence phenomena. When the molecule is excited, the electron from ground state comes to the first or second excited state levels. Excitation can be followed by internal conversion (conversion between vibration levels of first and second electron levels), spin-forbidden intersystem crossing (from singlet to triplet state, or spin-allowed deexcitation in radiative (fluorescence) or non-radiative way.

It was shown that fluorescence excitation and emission spectra are symmetrical. Schematic representation of mirror-imaged absorption and emission spectra (so called mirror-image rule) is shown in Figure 9. This characteristic has been explained by Franck-Condon principle. The theory assumes that during the excitation and emission process, the positions of atomic nuclei do not change. Thus, according to this principle, there is a preference for electron to transit from the ground state to certain vibration levels of the excitation state, which results in fine structuring of excitation spectra. Similarly, the relaxation from vibration levels to the ground state exhibits certain preference and fine structure in emission spectra is also observable. Because the probability of the excitation to vibration level (0 → 2 in Fig. 9A excitation) is equal to the probability of relaxation from particular vibration level to the ground state (0 → 2 in Fig. 9A emission), then absorption and emission spectra are symmetrical.

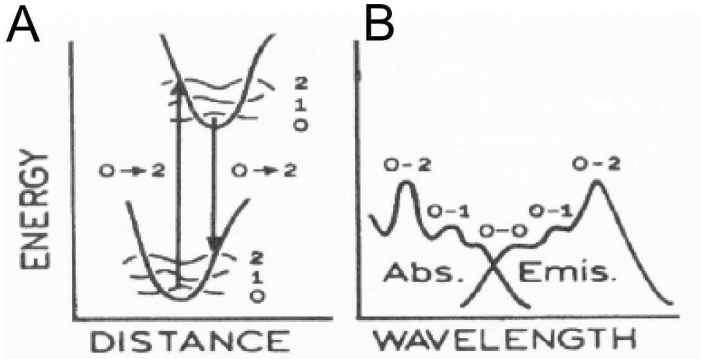

Figure 9 (A) Schematic illustration of the Franck-Condon principle. The probability of the excitation from 0 vibration level of ground state to 2 vibration level of excited state is equal to the relaxation from 0 vibration level of excited state to 2 vibration level of ground state. (B) Impact of the Franck-Condon principle on absorption and emission spectra. Both spectra are mirror images because of the same transition probability between particular levels. Graphics adapted from [67].

There are many characteristics of fluorescence; fluorescence intensity, polarization, lifetime, excitation spectra, emission spectra or quantum yield, which is defined as

$$Q = \frac{k_r}{k_r + k_{nr}}, \tag{5}$$

where k_r is the rate constant of radiative processes and k_{nr} is the rate constant of non-radiative processes (internal conversion, intersystem crossing, vibration of the molecule, *etc*.). The photon emission is single-molecular process, which is described by the first order kinetics

$$I(t) = I(0)e^{-kt}, \tag{6}$$

where *I(t)* corresponds to the fluorescence intensity in the time *t*, *I(0)* is the fluorescence intensity in the time = 0, *k* is the rate constant.

In the case that

$$\tau = \frac{1}{k}, \tag{7}$$

where τ is the fluorescence lifetime, Eq. 6 can be formulated as

$$I(t) = I(0)e^{-\frac{t}{\tau}}. \tag{8}$$

Using these equations the quantum yield can be defined as

$$Q = \frac{T_{r+nr}}{\tau_r}, \tag{9}$$

T_{r+nr} is the sum of radiative and non-radiative fluorescence lifetimes and τ_r is the fluorescence lifetime of the radiative processes. Note that according to the Eq. 8 fluorescence intensity decays exponentially. In description of multiexponentially decaying fluorophores, linear combination of monoexponentials is used.

The equations mentioned above show direct relations between rate constants, fluorescence lifetimes and quantum yields. These characteristics are often used in the most of fluorescence techniques.

2.6.2 Fluorescence lifetime imaging microscopy (FLIM)

As briefly stated above, the fluorescence lifetime is one of the most important fluorescence characteristics because of its sensitivity to the changes in fluorophore environment. Fluorophore lifetime can sense polarity, viscosity, presence of aromatic

molecules, pH and temperature. The changes in lifetime are highly used in biochemical/biological studies, e.g. monitoring of conformational changes of proteins, anisotropic data provide information about ligand-protein binding or monitor e.g. membrane viscosity.

It is important to mention that there are two main experimental techniques for lifetime determination, time-resolved and phase-modulation, respectively. In this and next chapter, only time-resolved technique will be discussed, however, in the papers attached to this Thesis phase-modulation technique is also elucidated.

FLIM is microscopic technique based on pixel by pixel scanning of the sample and the fluorescence intensity and lifetime information in each pixel is obtained. Analysis of such data is not complicated and can be done using two main approaches, decay fitting and phasor plots [68; 69] (Fig. 10), respectively. In the fluorescence decay fitting, every fluorescence decay in each pixel is analyzed separately using mathematical model for exponential fitting (see Eq. 8 for instance). Finally, maps of fluorescence lifetimes corresponding to every pixel are achieved. The phasor plot method is based on completely different idea. In this approach, *G* and *S* functions are calculated directly from the raw fluorescence data according to the following expressions

$$g_i(\omega)=\frac{\int_0^\infty I(t)\cos(\omega t)\,dt}{\int_0^\infty I(t)\,dt} \tag{10}$$

$$s_1(\omega)=\frac{\int_0^\infty I(t)\sin(\omega t)\,dt}{\int_0^\infty I(t)\,dt}, \tag{11}$$

$\omega = 2\pi F$, F is a frequency (can be repetition frequency of the laser or any other value), and plotted into the so called phasor plots. Relative position of each individual pixel in phasor plot provides the information about fluorescence lifetime distribution in the sample. Single-exponential fluorescence dyes are localized on the so called universal semicircle with the center [0.5, 0]. Multi-exponential dyes or mixtures of single-exponentials fall inside the universal semicircle. Note that the position in phasor plot is highly dependent on the frequency, which is used in the analysis. In other words, two sets of data can be compared only for equal frequencies.

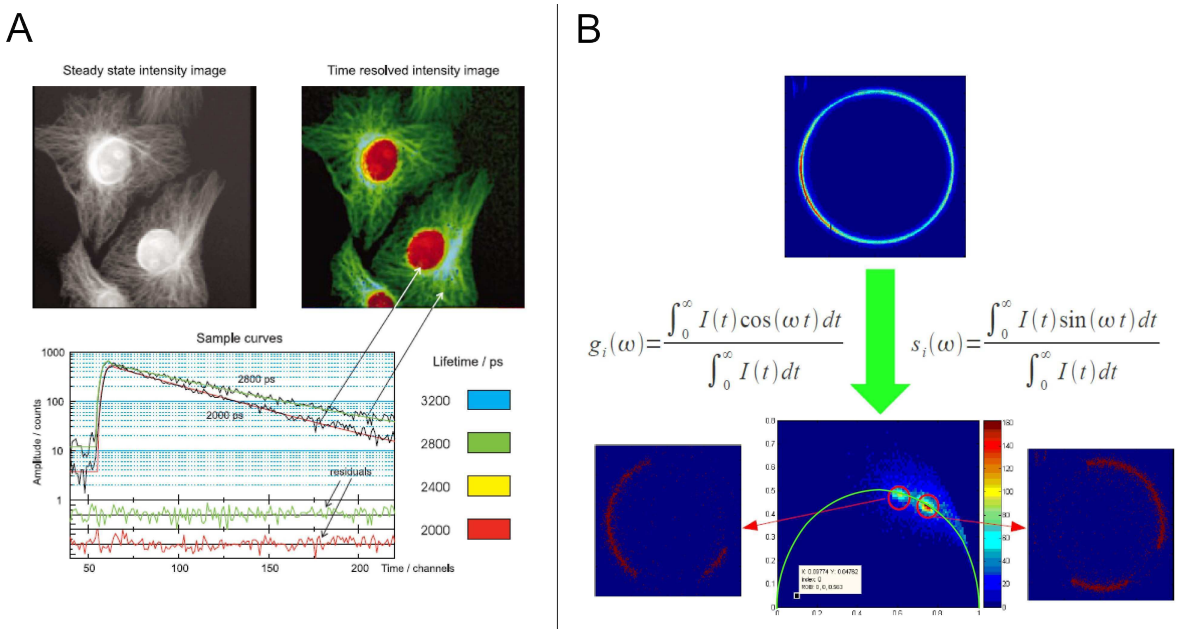

Figure 10 Schematic illustration of two concepts in analysis of FLIM data. Classic approach is based on fitting of each individual decay in all pixels which produces lifetime map of the sample (A). Phasor approach plots the positions of individual pixels into the phasor plot and provides information about lifetime distribution in the sample (B, picture in the center of lower part). Green semicircle in phasor plot corresponds to the position of single-exponential dyes (universal semicircle).

2.6.3 Fluorescence Resonance Energy Transfer (FRET) [70]

When two fluorophores are in a distance of 1 to 10 nm and the emission spectrum of one fluorophore (donor) overlaps with the absorption spectrum of the second fluorophore (acceptor), energy transfer can occur. During the energy transfer, part of the emission energy of the donor is used for the excitation of the acceptor. The energy transfer is accompanied by the decrease in fluorescence intensity and lifetime of the donor and increase of the fluorescence of the acceptor. As already mentioned the donor and the acceptor have to be very close to each other, in other words the distance at which energy transfer is 50 % efficient is called Főrster distance/radius and is typically ~ 50 Å. For quantification of energy transfer, the transfer rate is usually used, and decreases with the sixth root of the donor-acceptor distance.

In biological studies the molecular interactions very often happen on the scale of few nanometers which makes FRET powerful tool in their examination. However,

observation of the decrease (donor) or increase (acceptor) of fluorescence intensity is problematic because of the effects connected with the local changes in dye concentration and with the photoselection (only the molecules with dipole moment parallel to the polarity of the excitation beam can be fully excited). This reason makes fluorescence intensity unsatisfactory in quantification of energy transfer, and thus, fluorescence lifetime is used because of its non-sensitivity to the dye concentration, beam polarization and fluorophore orientation.

2.6.4 Fluorescence Correlation Spectroscopy (FCS)

FCS as one of the fluorescence fluctuation methods was introduced in early 1970s by Magde, Elson and Webb [71; 72] and is based on a statistical analysis of the time-scale of fluctuations of the fluorescence intensity $I(t)$. Such dependence is described by normalized autocorrelation function $G(\tau)$:

$$G(\tau)=\frac{\langle I(t)I(t+\tau)\rangle}{\langle I(t)\rangle^2}, \tag{12}$$

where the angle brackets represent an average over all values of the time t. The shape of the autocorrelation function bears information on the timescale of fluorescence intensity fluctuations, which originate from a small volume element of the sample and are recorded with a high temporal resolution. The intensity fluctuations mainly result from translational diffusion of molecules in and out of the detection volume and photochemical processes like banned intersystem crossing to a triplet state. The detection volume (often called confocal volume) is defined by the optics of the experimental setup and is usually on the order of femtoliters [73]. In the case of a two dimensional sample like a planar lipid bilayer, the confocal volume is actually defined by the intersection of the microscope focus and the plane of the bilayer. In that case it can be described by diffraction limited two-dimensional Gaussian profile [74; 75]. Fluctuations corresponding to the lateral diffusion occur on a submilisecond to a second timescale, while fluctuations due to photochemical processes are much faster. This enables one to separate each of their contributions to the recorded time traces [76; 77].

2.6.5 Determination of lateral diffusion by conventional FCS

The determination of lateral diffusion coefficients from recorded autocorrelation functions requires fitting of those by a theoretical model function. The parameters of interest are the diffusion time of fluorescent molecule τ_D (gives information about the time the fluorophore stays in the detection volume) and average number of fluorescent molecules in the confocal volume N (particle number). In the case of two-dimensional Brownian diffusion, the theoretical shape of $G(\tau)$ is given by [71; 75]:

$$G(\tau)=1+\frac{1}{N}\frac{1}{1+\left(\frac{\tau}{\tau_D}\right)}. \tag{13}$$

When fluorescence fluctuations, which are caused by intersystem crossing to a non-fluorescent triplet state are taken into account, an average fraction of fluorophores in triplet state T and intersystem crossing relaxation time τ_T need to be incorporated into Eq. 13 [6; 78], and thus, the autocorrelation curve is fitted by the following expression:

$$G(\tau)=1+\left[1-T+Texp\left(\frac{-\tau}{\tau_T}\right)\right]\frac{1}{N(1-T)}\frac{1}{1+\left(\frac{\tau}{\tau_D}\right)}. \tag{14}$$

In the case that more than one fluorophore with different diffusion times contribute to the recorded fluctuations, it has to be considered in Eq. 14, but I do not want to go to such details in this Thesis.

The signal-to-noise ratio in FCS is the highest when there is about one fluorescent molecule in the detection volume on average [79]. This means that for very low concentrations (in range of tens of nM), when one fluorescent molecule diffuses in the confocal volume, the FCS provides the most relevant information, and thus, fluorescence correlation spectroscopy is sometimes referred to as a single-molecule technique. However, it should be noted that the autocorrelation curve is always calculated from fluctuations caused by a large number of molecules.

The physically most relevant parameter describing lateral diffusion is the lateral diffusion coefficient D, which can be extracted directly from τ_D using the following relation:

$$D = \frac{\omega^2}{4\tau_D}, \tag{15}$$

where ω is the radius of the detection volume in the plane of diffusion and is defined as the radial distance from the optical axis, at which the intensity drops by e^{-2} [75; 79]. The surface concentration of fluorescent molecules c_S can be calculated in a similar manner from number of particles in the detection volume N. For a precise determination of diffusion coefficient D, the knowledge of confocal volume radius ω is critical. To obtain this information a reference FCS measurement of a fluorophore with well defined diffusion coefficient is applied. Although the radius of the beam-waist is calibrated, the real shape of the detection volume may differ from the assumed one (because of beam astigmatism, refractive index mismatch and other artefacts) and furthermore the radius of the beam-waist in the reference solution may vary from that in the sample of interest (because of differences in refractive indices).

2.6.6 Z scan FCS and diffusion law

In the previous section we mentioned difficulties of the FCS calibration. Z-scan FCS approach was developed to avoid such problems. The principle of this approach is based on acquiring of individual point measurements in dependence on positions along the optical axis (z-axis) of the microscope. All points are individually correlated according to the Eq. 12 and resulted autocorrelation functions are subsequently fitted with suitable model (e.g. Eq. 14). When the parameters of interest (τ_D, N) are plotted in dependence on relative position in the detection volume (Δz), planar system can be characterized by these equations:

$$\tau_D(\Delta z) = \frac{\omega_0^2}{4D}\left(1 + \frac{\lambda^2 \Delta z^2}{n^2 \pi^2 \omega_0^4}\right), \tag{16}$$

$$N(\Delta z) = N_0\left(1 + \frac{\lambda^2 \Delta z^2}{n^2 \pi^2 \omega_0^4}\right), \tag{17}$$

where $N_0 = \pi c_s \omega^2$, λ is the excitation wavelength, n is the refractive index. The parameters of interest D, c_s and ω are directly derived from the fit.

An analytical model suggested by Wawrezinieck et al. [80] and called apparent

diffusion law enables to some extend characterize membrane structures which are unresolvable by optical microscopes (smaller than optical microscope resolution). This model is based on the step by step change of the size of the detection area and observation of the dependence of the time the molecule stays in this detection area (ω). The dependence is linear for ω high enough in comparison to structures of interest (ω^2>10 for isolated domains and ω^2>2 for meshwork) and is described by

$$\tau_D^{app} = t_0 + \frac{\omega^2}{4D_{eff}}. \quad (18)$$

τ_D^{app} is the the apparent time the molecule takes to diffuse through the detection area, D_{eff} is the effective diffusion coefficient which bears the information about the macroscopic diffusion coefficient, probability of crossing the barriers and the density of the membrane structures (in the case of isolated domains). The intercept t_0 is equal to zero for membranes free of any structures, negative in the case of meshwork and positive in the presence of isolated domains in the membrane.

An application of the FCS diffusion law in z-scan FCS was introduced by Humpolickova et al. [81], where Eq. 18 was extended to

$$\tau_D^{app} = t_0 + \frac{\omega_0^2}{4D_{eff}} \frac{N}{N_0}, \quad (19)$$

where linear dependence is achieved by plotting of $\tau_D^{app}(\Delta z)$ for various ratios of $N(\Delta z)/N_0$.

2.6.7 Other fluorescence techniques for membrane dynamics studies

It is worth to mention that there are other fluorescence techniques useful in membrane dynamics unless they were not used in this work. Very helpful is Single Particle Tracking (SPT) method where every single fluorescence molecule is tracked along the sample. The SPT provides the information about lateral diffusion [82]. The laboratory of Enrico Gratton introduced Raster Image Correlation Spectroscopy (RICS) as a method for lateral diffusion determination applicable to living cells [83]. RICS is based on fast 3 dimensional scanning throughout the sample and the diffusion of fluorescent molecule is correlated with the speed of scanner in all three axes (diffusion in adjacent pixels in line ~

μs, pixels in successive lines ~ ms and pixels in different frames ~ s). The line-scan FCS approach has been introduced by Petra Schwille's group [84]. The principle is in scanning the line accompanied by simultaneous acquisition of FCS data in every pixel. Analysis of such data also provides insight into lateral diffusion of the sample.

2.7 General conclusions from the introduction

The cell membrane is not only physical barrier between outer and inner space of the cell, but also support for proteins involved in membrane signalling, signal transduction, endocytosis, exocytosis, vesicular transport and many others. In the past, there was general assumption that only proteins are responsible for all the processes mentioned above and lipids serve only as a support for them. But this is changed nowadays. It has been proven that lipid-protein interactions are very important to many membrane processes, that even some of such processes are regulated by individual lipid species and their concentration. Because of this, knowledge of biophysical characteristics of individual species and their behaviour and interactions between each others is very important in understanding of their impact on the membrane. Cell membranes are very complex systems with high amount of variables. Simplification (reducing the number of key parameters) is necessary for the characterization of influence of individual lipids. Model membranes such as GUVs and SPBs seem to be reasonable compromise in membrane studies.

Fluorescence techniques are excellent tool in visualization and dynamic characterization of model membranes as well as living cells. Fluorescence imaging displays cell membranes and localizes fluorescently labelled proteins, FLIM provides the information about microenvironment (polarity, viscosity, hydrophobicity) in the vicinity of the fluorophore, FRET measures relative distance between two fluorophores and FCS, SPT or RICS inform us about local mobility inside the membranes.

3 Aims of the study

The aim of this work was to contribute to a better understanding of the role of lipids in membrane organization and membrane-protein interactions by means of fluorescence techniques (mainly fluorescence microscopy techniques). More specifically, this work was focused on development of the fluorescence methods applicable to model membranes and mainly on using such methods to characterize membrane dynamics, the impact of individual lipids on membrane organization and the study of protein-lipid interactions and interplay. For simplicity, this work is structured into three main parts according to the questions I wanted to answer:

1) Is phasor plot analysis of lifetime data applicable to model membrane organization and protein conformation studies? Does phasor plot analysis bring new insights into biochemistry of proteins and lipid membranes?

2) Can we monitor and characterize membrane nanodomains in GUVs? If so, can we say anything about the formation of such domains and make any general conclusion?

3) Related to the protein-lipid interactions, is FCS good tool in description of dynamics of weakly bound peripheral proteins?

4 Results and Discussion

4.1 Question No 1:

Is phasor plot analysis of lifetime data applicable to model membrane organization and protein conformation studies? Does phasor plot analysis bring new insights into biochemistry of proteins and lipid membranes?

4.1.1 Characterization of the excited state processes using phasor plot approach (paper I)

The purpose of this paper was to develop a method that could be used to study mixtures of fluorophores for analytical purposes, that is, to be able to facilely compare different mixtures in such a way that differences in the fluorophore composition would be readily apparent. As already mentioned in section 2.6.2, a mixture of two monoexponential fluorophores with different fluorescence lifetimes, or a fluorophore characterized by a multiexponential decay, will produce a phasor point within the universal circle, indicating lifetime heterogeneity. The theoretical basis of the phasor plot analysis indicates that this measured phasor point will be located on a line between the points of the individual fluorophores or single-exponential components. Therefore, when three dyes are combined in solution, the resulting phasor point should be found constrained within a triangle that has vertices defined by the location of the phasor of the individual dyes (Fig. 11). Binary and tertiary fluorophore mixtures were studied using fluorophores in ethanol with widely separated lifetimes, namely DENS (fluorescence lifetime τ = 29.9 ns), IAEDANS (τ = 5.3 ns), and Rhodamine B (τ = 1.7 ns). Fig.11 shows the phasor data of each individual fluorophore (black dots), solutions containing a mixture of two dyes (DENS/IAEDANS, DENS/Rhodamine B, and IAEDANS/Rhodamine B), and a mixture of all three dyes. As expected, the individual fluorophore's phasor points are located along the universal circle, whereas the phasor points corresponding to mixtures of any two dyes fall on a line between the points on the universal circle corresponding to the individual dyes. For the mixture of the three dyes, the phasor point is located within the triangle defined by the three dual fluorophore mixture lines.

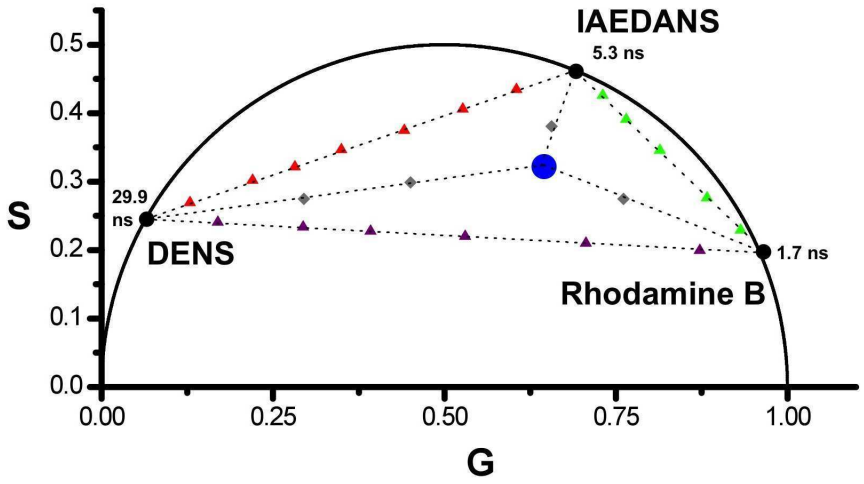

Figure 11 Phasor data corresponding to ethanol solutions of three fluorophores each of which is characterized by a single-exponential decay. Black circles correspond to the individual fluorophores. Colored triangles show the mixture of two particular fluorophores (red corresponds to the mixture of DENS and IAEDANS, green to the mixture of IAEDANS and Rhodamine B, and purple to the mixture of DENS and Rhodamine B, respectively). The blue circle corresponds to a mixture of all three fluorophores. Increasing the fluorescence contribution of one of the components moves the points closer to the specific corner of the triangle (gray diamonds).

We have also employed phasor plot analysis in the excited state processes like Förster resonance energy transfer and dipolar solvent relaxation, respectively. In the case of dipolar solvent relaxation the excitation changes the dipole moment of the fluorophore resulting in the reorganization of solvent molecules in the vicinity of the dye. The reorganization rate (between so called non-relaxed to relaxed state) depends on the rigidity of environment and non-covalent interactions and is valuable quantity in membrane or protein characterization. Because the phase delay of the emission of relaxed state (in solvent relaxation) or acceptor's lifetime after energy transfer (in FRET) is increased in comparison to non-relaxed or non-transferred state, those processes can fall in phasor plot outside the universal circle.

Fig. 12, left is an example of energy transfer and shows the phasor points associated with the visible emission (>525 nm) from EGFP, excited with both visible (471 nm) and ultraviolet (UV, 280 nm) excitation, as a function of modulation frequency (16–300 MHz). As is evident for the phasor plot, 471 nm excitation results in phasor points corresponding to single-exponential decays; that is, the points are all on the universal circle. On the other

hand, 280 nm excitation, which will directly excite the single tryptophan residue (as well as the tyrosine residues) in addition to some direct excitation of the EGFP chromophore, results in phasor points that are all outside of the universal circle. Hence, although some of the visible chromophores may be directly excited at 280 nm, there is enough tryptophan-to-chromophore energy transfer to move the phasor point outside of the universal circle.

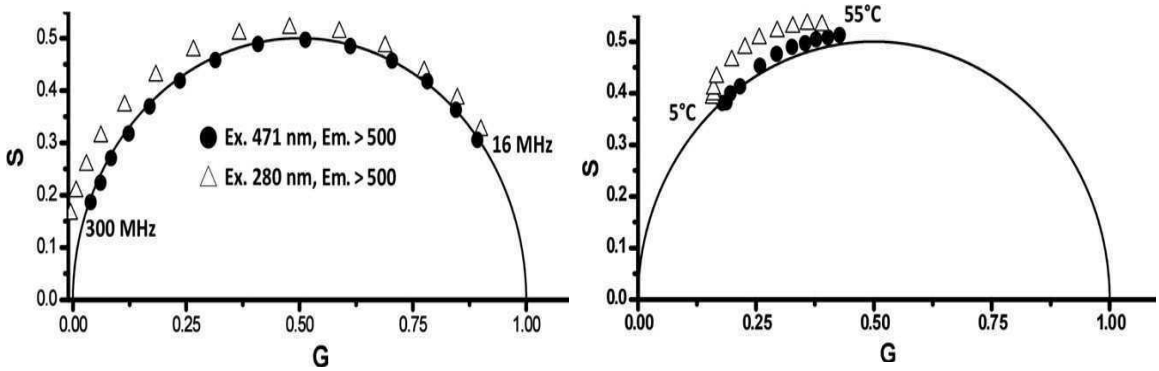

Figure 12 Left: Decay data of EGFP excited at 471nm and 280nm, emission was recorded at 500nm and higher. All of the data recorded with 280nm excitation fall outside the universal circle, an indication of an excited state process. Right: LAURDAN in DMPC vesicles. Circles and triangles represent data collected for temperatures between 5°C and 55°C with 5°C interval. Excited at 375nm; emission was viewed through 420-nm (circles) and 470-nm (triangles) longpass filters.

Similarly, inspection of the temperature dependence (from 5°C to 55°C) of the LAURDAN/DMPC vesicles' phasor plot shows that the phasor points corresponding to data collected using the 470-nm filter are completely outside of the universal circle, indicative of a dipolar solvent relaxation mechanism (Fig. 12, right). When the entire LAURDAN emission is collected using the 420-nm longpass filter, the phasor points lay along or very close to the universal circle, indicating that the non-relaxed emission dominates the observed decay. Using the 470-nm longpass filter, the collected emission is weighted primarily from the molecules that undergo dipolar relaxation and the location of the phasor points outside of the universal circle is more pronounced. However, the points above 25°C show a clear trend above the universal circle, indicating the presence of an excited state event.

In conclusion, we have demonstrated that the extension of the phasor method from FLIM to cuvette measurements provides a method that complements other approaches and that, in some cases, provides insights that would otherwise be difficult to obtain. In particular, the method allows facile analysis of sample heterogeneity and ready

identification of excited state processes such as dipolar relaxation and FRET.

New findings:

- Extension of phasor plot analysis to cuvette measurements
- Experimental confirmation of phasor theory
- Demonstration of the phasor analysis in excited state processes such as dipolar solvent relaxation and FRET

4.1.2 Phasor plot monitors proteins conformation, protein-ligand binding and protein kinetics (paper II)

In this paper we have used mainly intrinsic fluorescence of tryphtophane to characterize proteins such as lysozyme, dynamin 2, human serum albumin and human serum transferrin. We explored the changes in protein conformations by quenching and temperature studies and analyzed using the phasor plot. Briefly, the fluorescence quencher acrylamide rapidly decreases fluorescence lifetime of the protein lysozyme in dependence on the quencher concentration suggesting changes in the protein folding. The temperature experiments revealed two steps in lysozyme denaturation. At 40°C, the decreasing trend of lifetime heterogeneity is stopped which, according to the literature, corresponds to the reversible unfolding of the protein. At 70°C, the lifetime heterogeneity starts to increase indicating crossing of barrier where protein unfolding starts to be irreversible.

Figure 13 shows a set of data (acquired with 280 nm excitation) for thrombin, antithrombin, lysozyme, and mixtures therein. Antithrombin and lysozyme are not predicted to interact, therefore a solution containing the two proteins should produce a phasor point that falls directly on a line between their individual points (see sections 2.6.2 and 4.1.1, and Fig. 11). This outcome is clearly observed (Fig. 13) for the phasor plot of a 1:1 mixture of the two proteins. On the other hand, thrombin/antithrombin is known to form a tight complex and may be expected to produce a distinct phasor point away from the linear combination. The phasor point of the thrombin/antithrombin (1:1) indeed shifts inward away from the line connecting the points corresponding to the two pure proteins, indicating a change in intrinsic fluorescence on protein interaction. This demonstration shows how

phasor plots can provide a facile indication of protein interaction.

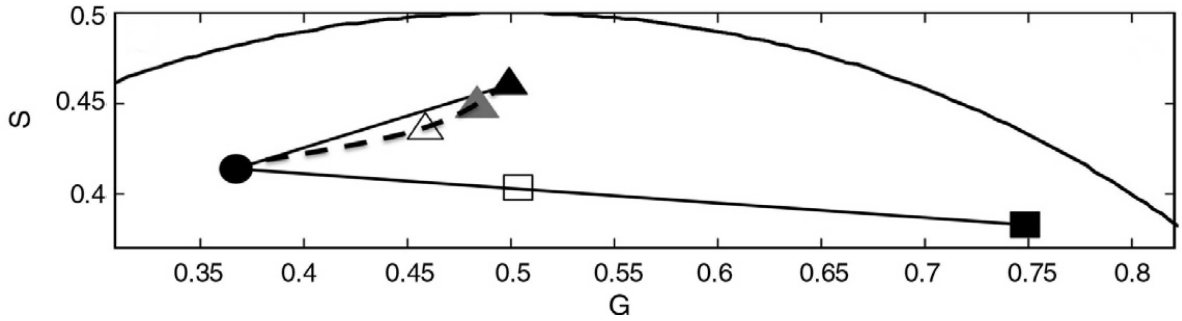

Figure 13 Protein-ligand interactions analyzed by phasor plot. Three different proteins (antithrombin-triangle, thrombin-circle, lysozyme-square) are shown by black closed symbols. The mixtures are in opened symbols. Mixture of antithrombin and lysozyme lies on the connecting line indicating no interaction between these two proteins. In contrary, mixture of antithrombin and thrombin is not located on the connecting line which stands for interaction of these proteins.

Protein denaturation mechanisms are a hot topic in protein science, however their studies are very complicated. Typical protein denaturants such as the urea or the guanidin hydrochloride (GdHCl) are often used in the protein unfolding studies. We have monitored intrinsic fluorescence of the lysozyme when urea and GdHCl were stepwise added to the solution (Fig. 14). The sequence of denaturants' concentrations was like follows; 0 M (closed circle), 1 M (opened circle), 2 M (opened triangle) and 6/8 M (closed triangle) GdHCl and urea are highlighted. Initial additions of denaturants cause similar changes, however higher concentration of urea or GdHCl follows totally different directions. The final points in phasor plot are dramatically different indicating unique unfolded forms of lysozyme.

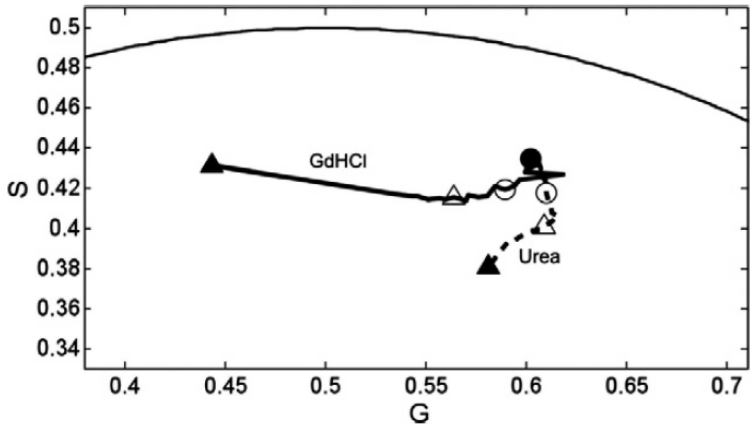

Figure 14 Denaturation studies of lysozyme were analyzed by phasor plot. Concentrations of denaturants were 0 M (closed circles), 1 M (opened circles), 2 M (opened triangles) and 6/8 M (closed triangles).

In this article, we have described the application of the phasor method to time-resolved studies on intrinsic protein fluorescence. Using this approach, the complex decay of protein fluorescence, due to either multiple emitting tryptophan residues or excited state reactions such as tyrosine-to-tryptophan energy transfer, can be reduced to a single point on a phasor plot. Activities such as ligand or protein binding and protein denaturation, which result in changes in the microenvironment of the tryptophan residue(s), lead to movements of the phasor point. The trajectory of the phasor point in response to a physical or chemical perturbation can be followed to provide insights into the processes under investigation.

New findings:

- The phasor plot is simple approach in the analysis of intrinsic protein fluorescence
- The phasor plot analysis clearly monitors the protein-ligand or protein-protein interactions
- Description of unique denaturation pathways of protein lysozyme

4.2 Question No 2:

Can we monitor and characterize membrane nanodomains in GUVs? If so, can we say anything about the formation of such domains and make any general conclusions?

4.2.1 Conceptual limitations in energy transfer for membrane nanodomain size and surface area determination revealed by molecular dynamics (paper III)

Förster resonance energy transfer is often employed in characterization of membrane nanodomains, also due to the fact that FRET can report on nanodomains even if they are formed transiently. The size determination of these nanodomains by FRET requires knowledge about partitioning of donors (D) and acceptors (A) between nanodomains and the remaining liquid-disordered (L_d) bilayer. In this work we mainly discuss the partition coefficients of individual fluorophores between liquid ordered and disordered phases in model membranes and their relation to the domain size determination by FRET. There are three possible cases; I) both dyes are located in L_o nanodomains, II) D/A pairs are excluded from nanodomains and III) donor and acceptor have increased affinity to different phases (Fig. 15). By means of molecular dynamics we have calculated the probabilities of the ability to detect membrane domains and related them to the domains' sizes and domains' surface area (Fig. 15). The probability is expressed by the ratio of steady-state intensity obtained from donors (F_d) to the intensity of donors when D/A pairs are distributed uniformly in the bilayer (F_d(uni)). Note that ratio higher than 1.2 is suitable for membrane size and area determination. Although first two cases seem to be most useful in the energy transfer studies, we have revealed that relevant results can be obtained only when distribution constants K_d and K_a (defined as $K_i=[i]_{Lo}/[i]_{Ld}$, i=D or A) are both higher than 5 (case I) or lower than 0.01 (case II), respectively. However, we found out that the case III is ideal in membrane characteristic studies, especially when $K_d > 3$ and $K_a < 0.01$.

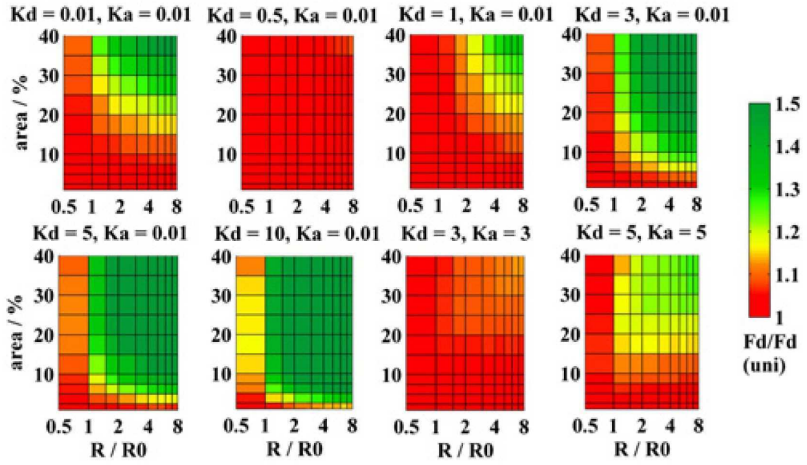

Figure 15 Map of FRET resolutions represented by the ratio $F_d/F_d(uni)$ as a function of domain radius and domain surface area simulated for various values of K_d and K_a. Note that domain sizes are expressed relatively to the Förster radius R_0.

We also discuss four FRET pairs (which we found in the literature) and their real use in nanodomain characterization. The FRET pairs were;

I) NBD-PE/Rhodamine-PE with $K_d = 4.3$, $K_a = 0.37$ and $R_0 \sim 5$ nm [85],

II) BODIPY-PC/fast-DiI with $K_d = 0.1$, $K_a = 0.1$ and $R_0 \sim 6.5$ nm [86],

III) Alexa Fluor 647 cholera toxin subunit B/DiD with $K_d = 11$ (6), $K_a = 0.004$ and $R_0 \sim 5.4$ nm, and,

IV) Perylene/fast-DiI with $K_d = 0.8$ (3), $K_a = 0.01$ and $R_0 \sim 5$ nm [35].

All the FRET pairs were examined in systems with different lipid compositions which explains small discrepancies in distribution coefficients. According to our simulations, best FRET pair was Alexa Fluor 647 cholera toxin subunit B/DiD followed by Perylene/fast-DiI, especially when $K_d = 3$ was used in calculations. Unfortunately obvious disadvantage of the cholera toxin is its cross-linking ability, which changes the local lipid composition in the membrane as reported by Hammond et al. [35].

New findings:

- Description of theoretical limits of FRET for nanodomain detection
- The simulation of the effectiveness of FRET in nanodomain size determination for FRET pairs with various partition coefficients

- Discussion of realistic FRET pairs found in the literature, which were intensively used in nanodomains' characterization

4.2.2 Characterization of nanodomain structures in terms of mechanism of formation and sizes in GUVs (paper IV)

Changes of membrane organization upon cross-linking of its components trigger cell signaling response to various exogenous factors. Cross-linking of raft gangliosides GM1 with cholera toxin (CtxB) was demonstrated to cause microscopic phase separation in model membranes and the CtxB-GM1 complexes forming a minimal lipid raft unit are subject of ongoing cell membrane research. Direct observation of such nano-scaled heterogeneities in plasma membrane by means of optical microscopy fails either due to its poor resolution, or anticipated transient character of rafts. From these reasons, those subdiffraction sized rafts have never been described in terms of size and dynamics. In this work, we aimed to investigate early stages of the CtxB induced phase separation in model membranes (GUVs) composed of Sph/DOPC/Chol, e.g. formation, size and dynamic properties of nanodomains by means of z-scan FCS and FLIM-FRET.

The lipid compositions mostly investigated in this research are very close to the microscopic phase coexistence boundary (Fig. 6) and are summarized in Table 3. The cross-linker CtxB was added in two steps, here presented as the low loading and the high loading (marked with apostrophe, e.g. **B** and **B'**). We should stress out that under our conditions the micrometer sized domains (optically resolvable) were not observed in both, composition **B** and **C**. These microdomains were not seen even at high CtxB loading too. Fig. 16 shows results from CtxB-Alexa647 measured by z-scan FCS and analyzed by the Wawrezinieck's apparent diffusion law [80]. We also performed FLIM-FRET measurements of energy transfer from CtxB-Alexa488 (donor) to DiD (acceptor), a lipid tracer preferentially residing in L_d phase, and monitored by phasor plot approach the changes in a fluorescence decay histogram of the donor (Fig. 17).

Table 3 Molar fractions of lipids in GUV lipid composition discussed in this work

	DOPC	Sph	Chol	DOPG	GM1
A	0.68	0	0.25	0.05	0.02
B	0.49	0.19	0.25	0.05	0.02
C	0.44	0.24	0.25	0.05	0.02

Composition A is a Sph free lipid mixture which serves as a blank experiment (no lipid segregation occurs). Diffusion behavior of the CtxB is independent on its load and the apparent diffusion law suggests free diffusion (no intercept) for the cross-linker molecules (Fig. 16). FLIM-FRET results show the maximal energy transfer suggesting homogeneous distribution of the donors and the acceptors molecules in the membrane (Fig. 17).

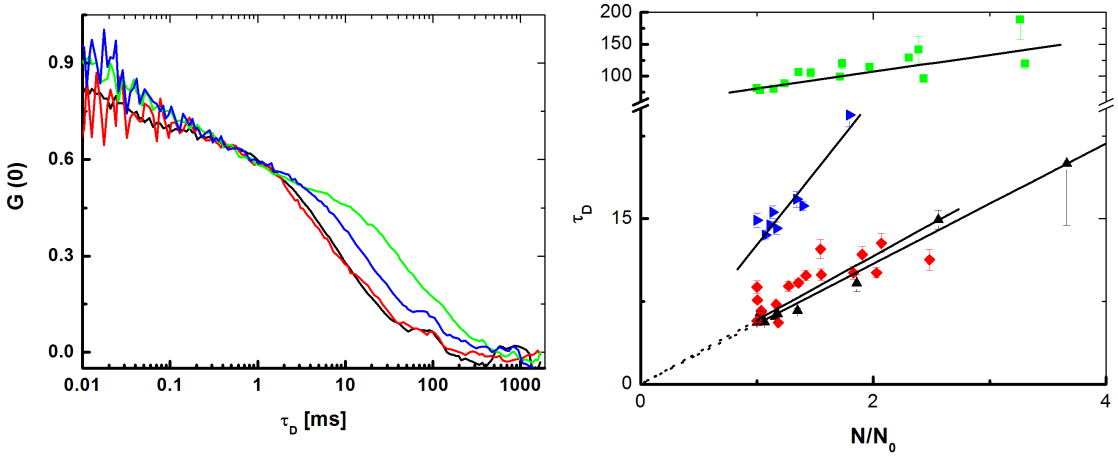

Figure 16 Left: Autocorrelation curves of labeled CtxB-Alexa647 for compositions **A** (black), **B** (red), **B'** (green) and **C** (blue). Right: Corresponding apparent diffusion laws (colors as in the left part). Black lines are linear fits of the data.

Compositions' B and B' diffusion behavior significantly differs from Sph free system. First, this composition is dependent on the cross-linker load and, second, the apparent diffusion law for high loads shows a significant positive temporal offset suggesting the presence of a nanometer sized domains in which the diffusion is considerably slowed down (Fig. 16). Moreover, decreased efficiency of the energy transfer in composition **B** in comparison to composition **A** indicates the separation of the donor and the acceptor molecules and, thus, the presence of the domains. This effect was even more pronounced when high load of CtxB was added (Fig. 17) implying the enlargement of the domains. The analytical Baumann and Fayer model [87] was applied on fluorescent lifetime

decays of the donor providing a mean domain radius. We have determined that the average domain radius in the compositions **B** and **B'** is 5 nm and 8 nm, respectively.

Composition C dramatically differs from composition **B** in three aspects (Fig. 16); 1) no concentration dependence of the cross-linker loading was observed, 2) although it contains higher amount of Sph compared to composition **B**, the CtxB-Alexa647 transition time was slower than in **B'** but longer in comparison to **B** and 3) the temporal offset in the apparent diffusion law is significantly lower (or even equal to 0) when compared to **B'**. The high decrease of the efficiency of the energy transfer suggests large domains and Baumann and Fayer model confirms those hypotheses when determining the radius of the domains (R=24 nm).

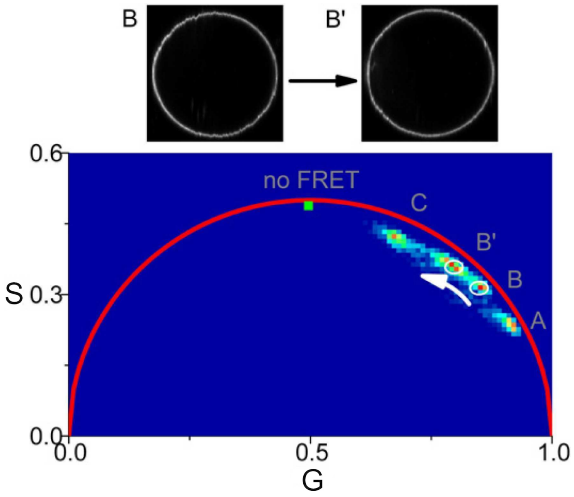

Figure 17 Lower part: Phasor plot analysis of fluorescence donor's lifetime (CtxB-488) influenced by energy transfer. Upper part: Intensity images of GUVs measured at lower and higher CtxB-488 loading. Note that even at higher loading no visual phase separation is observable.

In conclusion we have found two different types of subwavelength domains. Since in **B**, the diffusion character changes at increased cross-linker load, we propose that these nanodomains are transiently constituted upon collision of CTxB-GM1 complexes. In **B** the domain formation is therefore initiated exclusively by the cross-linker and consequently stabilized by Sph. In contrast, our data indicate that small lipid domains are formed in the composition **C** already before the cross-linker is added and their existence is attributed mainly to lipid-lipid interactions. We hypothesize that the addition of the cross-linker

induces further coalescence into larger membrane assemblies that eventually leads to microscopic phase separation.

New findings:

- We observed 2 types of nanodomains depending on Sph concentration
- We postulated the mechanism of nanodomain formation
- For the first time we determined the size of nanodomains in GUVs

4.3 Question No. 3

Related to the protein-lipid interactions, is FCS a good tool in description of dynamics of weakly bound peripheral proteins?

4.3.1 Characterization of prothrombin interaction with negatively charged model membranes (paper V)

Several enzymatic processes involving proteins containing γ-carboxyglutamic acid residues require the association of those proteins with negatively charged membrane surfaces. As a paradigm for such processes serves the membrane binding of the blood coagulation protein prothrombin followed by lateral diffusion to the prothrombinase enzyme complex. Since those proteins are only weakly binding to relevant membrane surfaces (apparent equilibrium dissociation constants K_d are in the μM range), at physiological protein concentrations there is a considerable amount of unbound protein and, thus, the lateral protein diffusion coefficients are difficult to access. We show that z-scan FCS is a simple method for the determination of 2D diffusion coefficients of those weakly bound proteins. Moreover, together with pulsed interleaved excitation (PIE) we are able to simultaneously monitor lipid and protein diffusion and thus obtain direct information on possible coupling of both diffusion processes. Specifically, we investigated the calcium-dependent binding of Alexa633 labeled bovine prothrombin (BP) to SPBs composed of DOPC and DOPS. The SPBs of different lipid composition were labeled by DOPE-Atto488.

In order to extract the information about BP only bound to the membrane, mathematical model combining 2D and 3D diffusion has been employed when fitting autocorrelation functions:

$$G(\tau)=1+\frac{1}{N(1-T)}\left(1-T\left(1-e^{\frac{-\tau}{\tau_T}}\right)\right)\left(\frac{FRa}{1+\frac{\tau}{\tau_{Da}}}\frac{1}{\left(1+\frac{\tau}{\tau_{Da}}\left(\frac{\omega_0}{\omega_z}\right)^2\right)^{\frac{1}{2}}}+\frac{1-FRa}{1+\frac{\tau}{\tau_{Db}}}\right) \qquad (20)$$

where *Fra* is the percentage of unbound BP molecules, ω_0 and ω_z are spatial parameters of the confocal volume, τ_{Da} and τ_{Db} are diffusion times of unbound (D_3) and bound (D_2) BP. The parameter τ_{Db} has been used in further analysis according to the Eq. 16 and diffusion

coefficient D_2 has been determined. Comparison of D_2 values for BP and lipids (Fig. 18, left) shows that BP diffuses significantly slower. However, BP and lipid diffusion display qualitatively the same trends suggesting that both lateral diffusion processes are strongly related with each other. At low (10 %) DOPS content and low BP concentration the difference between protein and lipid diffusion is considerably smaller than at higher DOPS contents.

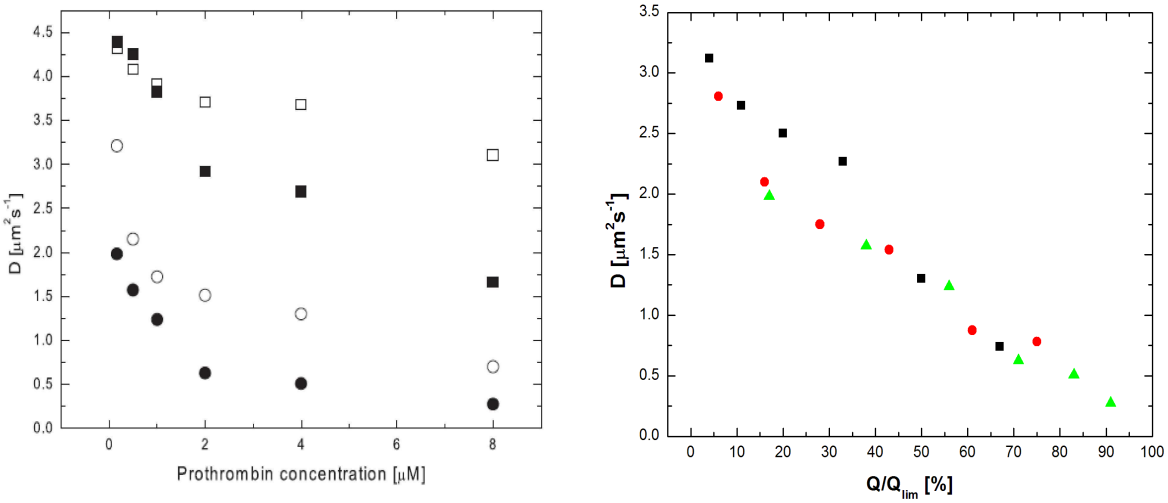

Figure 18 Left: Comparison of lateral diffusion coefficients of prothrombin (circles) and membrane (squares) in dependence on prothrombin loading. Opened symbols correspond to the membrane with 10% of negatively charged phosphatidylserine (PS), closed symbols to the membrane with 30% of PS. Right: Dependence of BP lateral diffusion coefficients on the relative amount of bound BP Q/Q_{lim}. Data were determined for 10 mol % of DOPS (black), 20 mol % of DOPS (red) and 30 mol % of DOPS (green) containing DOPC SPBs.

From the dependencies of the particle numbers on the axial sample positions at different protein concentrations phosphatidylserine-dependent equilibrium dissociation constants are derived confirming literature values. Moreover, number of bound BP molecules Q and limiting value of bound BP proteins Q_{lim} are also parameters of interest. Our data show that with increasing Q (e.g. with increasing amount of DOPS or BP used) protein D_2 values decrease. Above 30 % Q/Q_{lim} the D_2 values obtained for three different DOPS contents overlap perfectly. In this range the observed dependency might be explained by a model based on bound BP molecules acting as impermeable diffusion obstacles. Interestingly, in the physiological relevant range (Q/Q_{lim} < 30 %) the BP diffusion weakly bound to 10 % DOPS SPBs appears to be faster than on SPBs with higher DOPS content, indicating that at the same surface coverage the increasing amount of available DOPS

headgroups is slowing down BP lateral diffusion (Fig. 18, right).

In summary, we found that the lateral diffusion of BP is coupled with the diffusion of DOPE-Atto488. However, BP is diffusing considerably slower than the lipids. No differences in the lateral diffusion within both layers of the used SPBs were observed. Thus, there is no evidence for significantly faster diffusion within the layer facing the support compared to diffusion within the lipid layer binding BP, suggesting that the reason for the difference in D_2 values between BP and lipids might be connected with the mechanism of BP diffusion. However, explanations based on hydrophobic interactions between the non-fragment part of BP and the SPBs or a possible exchange of DOPS molecules bound to BP with unbound ones appear at that point as too speculative.

New findings:

- For the first time, 2 color FCS in PIE mode has been used in lipid-protein studies
- Z-scan FCS is a robust approach for the determination of lateral diffusion coefficients of weakly bound proteins
- We have revealed coupling of BP and labeled lipid, however, the lateral diffusion of BP was 2-times slower in comparison to the membrane diffusion

5 Conclusion

In this Thesis it has been shown that the fluorescence phenomenon is a versatile tool in membrane and protein studies.

More specifically, we have brought a new concept to the analysis of fluorescence lifetime data (phasor plot) and its utilization in biological, biochemical and biophysical research. The phasor plot was introduced as a powerful tool in monitoring of; 1) excited state processes like energy transfer and solvent relaxation, 2) protein folding and denaturation, 3) protein-protein interaction and 4) protein kinetics.

We have also stated the limitations of the energy transfer in the membrane nanodomain studies. With this knowledge, the membrane nanodomains were characterized in terms of the mechanism of formation, size and stability. Additionally, the relation between the nanodomain formation and rigidity and the external cross-linker Cholera toxin subunit B was described.

Last but not least, we have introduced the method in combination with the analytical model which enables the characterization of the dynamics of the proteins which are weakly bound to the membrane. Using this approach it has been confirmed the coupling in diffusion of the blood coagulation cascade protein prothrombin with membrane lipids, however the protein diffusion was found surprisingly two times slower.

6 References

[1] Singer, S.J. & Nicolson, G.L. (1972). *Science (80-)* **175**, 720-731.
[2] Simons, K. & Ikonen, E. (1997). *Nature* **387**, 569-572.
[3] Kusumi, A., Koyama-Honda, I. & Suzuki, K. (2004). *Traffic* **5**, 213-230.
[4] Lindner, R. & Naim, H.Y. (2009). *Exp Cell Res* **315**, 2871-2878.
[5] Brian, A.A. & McConnell, H.M. (1984). *Proceedings of the National Academy of Sciences of the United States of America-Biological Sciences* **81**, 6159-6163.
[6] Benes, M., Billy, D., Benda, A., Speijer, H., Hof, M. & Hermens, W.T. (2004). *Langmuir* **20**, 10129-10137.
[7] Angelova, M.I. & Dimitrov, D.S. (1986). *Faraday Discuss* **81**, 303-+.
[8] Bagatolli, L.A., Parasassi, T. & Gratton, E. (2000). *Chem Phys Lipids* **105**, 135-147.
[9] Montes, L.R., Alonso, A., Goni, F.M. & Bagatolli, L.A. (2007). *Biophys J* **93**, 3548-3554.
[10] Pott, T., Bouvrais, H. & Meleard, P. (2008). *Chem Phys Lipids* **154**, 115-119.
[11] Tanford, C. (1973). *Neurosci Res Program Bull* **11**, 193-195.
[12] Luckey, M. (2008). *Membrane Structural Biology* , Cambridge University Press.
[13] Epand, R.M. (1998). *Biochim Biophys Acta* **1376**, 353-368.
[14] Quehenberger, O. & Dennis, E.A. (2011). *N Engl J Med* **365**, 1812-1823.
[15] Hannich, J.T., Umebayashi, K. & Riezman, H. (2011). *Cold Spring Harb Perspect Biol* **3**, .
[16] Lingwood, D. & Simons, K. (2010). *Science (80-)* **327**, 46-50.
[17] Simons, K. & Sampaio, J.L. (2011). *Cold Spring Harb Perspect Biol* **3**, a004697.
[18] Tannert, A., Pohl, A., Pomorski, T. & Herrmann, A. (2003). *Int J Antimicrob Agents* **22**, 177-187.
[19] Lamb, D.C., Jackson, C.J., Warrilow, A.G.S., Manning, N.J., Kelly, D.E. & Kelly, S.L. (2007). *Mol Biol Evol* **24**, 1714-1721.
[20] Simons, K. & van Meer, G. (1988). *Biochemistry* **27**, 6197-6202.
[21] Hancock, J.F. (2006). *Nat Rev Mol Cell Biol* **7**, 456-462.
[22] Ikonen, E. (2001). *Curr Opin Cell Biol* **13**, 470-477.
[23] Niemelä, P.S., Ollila, S., Hyvönen, M.T., Karttunen, M. & Vattulainen, I. (2007). *PLoS Comput Biol* **3**, e34.
[24] Waheed, A.A. & Freed, E.O. (2010). *Viruses* **2**, 1146-1180.
[25] Holowka, D., Gosse, J.A., Hammond, A.T., Han, X., Sengupta, P., Smith, N.L., Wagenknecht-Wiesner, A., Wu, M., Young, R.M. & Baird, B. (2005). *Biochim Biophys Acta* **1746**, 252-259.
[26] Soccio, R.E. & Breslow, J.L. (2004). *Arterioscler Thromb Vasc Biol* **24**, 1150-1160.
[27] Maxfield, F.R. & Tabas, I. (2005). *Nature* **438**, 612-621.
[28] Goldstein, J.L. & Brown, M.S. (2001). *Science (80-)* **292**, 1310-1312.
[29] Finkelstein, A. & Cass, A. (1967). *Nature* **216**, 717-718.
[30] Thewalt, J.L. & Bloom, M. (1992). *Biophys J* **63**, 1176-1181.
[31] Marsh, D. & Smith, I.C. (1973). *Biochim Biophys Acta* **298**, 133-144.
[32] Róg, T., Pasenkiewicz-Gierula, M., Vattulainen, I. & Karttunen, M. (2009). *Biochim Biophys Acta* **1788**, 97-121.
[33] Pandit, S.A., Jakobsson, E. & Scott, H.L. (2004). *Biophys J* **87**, 3312-3322.

[34] Gallová, J., Uhríková, D., Islamov, A., Kuklin, A. & Balgavý, P. (2004). *Gen Physiol Biophys* **23**, 113-128.
[35] Hammond, A.T., Heberle, F.A., Baumgart, T., Holowka, D., Baird, B. & Feigenson, G.W. (2005). *Proc Natl Acad Sci U S A* **102**, 6320-6325.
[36] de Almeida, R.F.M., Fedorov, A. & Prieto, M. (2003). *Biophys J* **85**, 2406-2416.
[37] Simons, K. & Vaz, W.L.C. (2004). *Annu Rev Biophys Biomol Struct* **33**, 269-295.
[38] Eggeling, C., Ringemann, C., Medda, R., Schwarzmann, G., Sandhoff, K., Polyakova, S., Belov, V.N., Hein, B., von Middendorff, C., Schönle, A. et al. (2009). *Nature* **457**, 1159-1162.
[39] Stefl, M., Sachl, R., Humpolíčková, J., Cebecauer, M., Macháň, R., Kolářová, M., Johansson, L.B. & Hof, M. (2012). *Biophys J* **102**, 2104-2113.
[40] Przybylo, M., Sykora, J., Humpolickova, J., Benda, A., Zan, A. & Hof, M. (2006). *Langmuir* **22**, 9096-9099.
[41] Baumgart, T., Hammond, A.T., Sengupta, P., Hess, S.T., Holowka, D.A., Baird, B.A. & Webb, W.W. (2007). *Proc Natl Acad Sci U S A* **104**, 3165-3170.
[42] Kaiser, H., Lingwood, D., Levental, I., Sampaio, J.L., Kalvodova, L., Rajendran, L. & Simons, K. (2009). *Proc Natl Acad Sci U S A* **106**, 16645-16650.
[43] Baumgart, T., Hunt, G., Farkas, E.R., Webb, W.W. & Feigenson, G.W. (2007). *Biochim Biophys Acta* **1768**, 2182-2194.
[44] Wang, T.Y. & Silvius, J.R. (2000). *Biophys J* **79**, 1478-1489.
[45] Sanchez, J. & Holmgren, J. (2011). *Indian J Med Res* **133**, 153-163.
[46] Legler, D.F., Doucey, M., Schneider, P., Chapatte, L., Bender, F.C. & Bron, C. (2005). *FASEB J* **19**, 73-75.
[47] Ratto, T.V. & Longo, M.L. (2003). *Langmuir* **19**, 1788-1793.
[48] Saxton, M.J. (1989). *Biophys J* **56**, 615-622.
[49] Vaz, W.L., Clegg, R.M. & Hallmann, D. (1985). *Biochemistry* **24**, 781-786.
[50] Vaz, W.L.C., Goodsaid-Zalduondo, F. & Jacobson, K. (1984). *FEBS Lett* **174**, 199-207.
[51] Almeida, P.F., Vaz, W.L. & Thompson, T.E. (1992). *Biochemistry* **31**, 7198-7210.
[52] Falck, E., Patra, M., Karttunen, M., Hyvönen, M.T. & Vattulainen, I. (2004). *Biophys J* **87**, 1076-1091.
[53] Liu, C., Paprica, A. & Petersen, N.O. (1997). *Biophys J* **73**, 2580-2587.
[54] Petrov, E.P. & Schwille, P. (2008). *Biophys J* **94**, L41-3.
[55] Hughes, B.D., Pailthorpe, B.A., White, L.R. & Sawyer, W.H. (1982). *Biophys J* **37**, 673-676.
[56] Saffman, P.G. & Delbruck, M. (1975). *Proc Natl Acad Sci U S A* **72**, 3111-3113.
[57] Saffman, P.G. (1976). *J Fluid Mech* **73**, 593-602.
[58] Saxton, M.J. (1996). *Biophys J* **70**, 1250-1262.
[59] Saxton, M.J. (2007). *Biophys J* **92**, 1178-1191.
[60] Saxton, M.J. (2001). *Biophys J* **81**, 2226-2240.
[61] Saxton, M.J. (1994). *Biophys J* **67**, 2110-2119.
[62] Deverall, M.A., Gindl, E., Sinner, E., Besir, H., Ruehe, J., Saxton, M.J. & Naumann, C.A. (2005). *Biophys J* **88**, 1875-1886.
[63] Saxton, M.J. (1995). *Biophys J* **69**, 389-398.
[64] Wenger, J., Conchonaud, F., Dintinger, J., Wawrezinieck, L., Ebbesen, T.W.,

Rigneault, H., Marguet, D. & Lenne, P. (2007). *Biophys J* **92**, 913-919.
[65] Saxton, M.J. (1990). *Biophys J* **58**, 1303-1306.
[66] Stokes, G.G. (1852). *Philosophical Transactions of the Royal Society of London* **142**, 463-562.
[67] Lakowicz, J. (1999). *Principles of Fluorescence Spectroscopy* , Kluwer Academic/Plenum Publishers, New York.
[68] Jameson, D.M., Gratton, E. & Hall, R.D. (1984). *Applied Spectroscopy Reviews* **20**, 55-106.
[69] Digman, M.A., Caiolfa, V.R., Zamai, M. & Gratton, E. (2008). *Biophys J* **94**, L14-6.
[70] Förster, T. (1948). *Annalen der Physik* **437**, 55-75.
[71] Elson, E. & Magde, D. (1974). *Biopolymers* **13**, 1-27.
[72] Magde, D., Elson, E.L. & Webb, W.W. (1974). *Biopolymers* **13**, 29-61.
[73] Enderlein, J., Gregor, I., Patra, D., Dertinger, T. & Kaupp, U.B. (2005). *Chemphyschem* **6**, 2324-2336.
[74] Dertinger, T., Pacheco, V., von der Hocht, I., Hartmann, R., Gregor, I. & Enderlein, J. (2007). *Chemphyschem* **8**, 433-443.
[75] Thompson, N.L. (1991). In *Topics in Fluorescence Spectroscopy*, ed. Lakowicz, J.R. (Plenum Press, New York), pp. 337-378.
[76] Ries, J. & Schwille, P. (2008). *Physical Chemistry Chemical Physics* **10**, 3487-3497.
[77] Hess, S.T., Huang, S., Heikal, A.A. & Webb, W.W. (2002). *Biochemistry* **41**, 697-705.
[78] Schwille, P., Oehlenschläger, F. & Walter, N.G. (1996). *Biochemistry* **35**, 10182-10193.
[79] Benda, A., Benes, M., Marecek, V., Lhotsky, A., Hermens, W.T. & Hof, M. (2003). *Langmuir* **19**, 4120-4126.
[80] Wawrezinieck, L., Rigneault, H., Marguet, D. & Lenne, P.F. (2005). *Biophys J* **89**, 4029-4042.
[81] Humpolickova, J., Gielen, E., Benda, A., Fagulova, V., Vercammen, J., Vandeven, M., Hof, M., Ameloot, M. & Engelborghs, Y. (2006). *Biophys J* **91**, L23-L25.
[82] Saxton, M.J. (1997). *Biophys J* **72**, 1744-1753.
[83] Rossow, M.J., Sasaki, J.M., Digman, M.A. & Gratton, E. (2010). *Nat Protoc* **5**, 1761-1774.
[84] Ries, J., Chiantia, S. & Schwille, P. (2009). *Biophys J* **96**, 1999-2008.
[85] de Almeida, R.F.M., Loura, L.M.S., Fedorov, A. & Prieto, M. (2005). *J Mol Biol* **346**, 1109-1120.
[86] Heberle, F.A., Wu, J., Goh, S.L., Petruzielo, R.S. & Feigenson, G.W. (2010). *Biophys J* **99**, 3309-3318.
[87] Baumann, J. & Fayer, M.D. (1986). *J Chem Phys* **85**, 4087-4107.

7 Appendices

7.1 List of Publications

Paper I - Applications of Phasors to In Vitro Time-Resolved Fluorescence Measurements: Štefl, M., James, N.G., Ross, J.A., Jameson, D.M., Analytical Biochemistry, 410(1), 62-69, 2011

Paper II - Applications of Phasor Plots to in Vitro Protein Studies: James, N.G., Ross, J.A., Štefl, M., Jameson, D.M., Analytical Biochemistry, 410(1), 70-76, 2011

Paper III - Limitations of Electronic Energy Transfer in the Determination of Lipid Nanodomain Sizes: Šachl, R., Humpolíčková, J., Štefl, M., Johansson, L.B. -A., Hof, M., Biophysical Journal, 101(11), L60-L62, 2011

Paper IV - Dynamics and Size of Crosslinking-Induced Lipid Nanodomains in Model Membranes: Štefl, M., Šachl, R., Humpolíčková, J., Cebecauer, M., Macháň, R., Kolářová, M., Johansson, L.B.-A., Hof, M., Biophysical Journal, 102(9), 2104-2113, 2012

Paper V - Simultaneous Characterization of Lateral Lipid and Prothrombin Diffusion Coefficients by z-scan Fluorescence Correlation Spectroscopy: Štefl, M., Kulakowska, A., Hof, M., Biophysical Journal, 97(3), L1-L3, 2009

I

Applications of Phasors to In Vitro Time-Resolved Fluorescence Measurements

Štefl, M., James, N.G., Ross, J.A., Jameson, D.M.
Analytical Biochemistry, 410(1), 62-69, 2011

Analytical Biochemistry 410 (2011) 62–69

Contents lists available at ScienceDirect

Analytical Biochemistry

journal homepage: www.elsevier.com/locate/yabio

Applications of phasors to in vitro time-resolved fluorescence measurements

Martin Štefl [a], Nicholas G. James [b], Justin A. Ross [b], David M. Jameson [b,*]

[a] J. Heyrovský Institute of Physical Chemistry, v.v.i., Academy of Sciences of the Czech Republic, Dolejškova 3, Prague 18223, Czech Republic
[b] Department of Cell and Molecular Biology, John A. Burns School of Medicine, University of Hawaii, Honolulu, HI 96813, USA

ARTICLE INFO

Article history:
Received 27 July 2010
Received in revised form 5 November 2010
Accepted 7 November 2010
Available online 13 November 2010

Keywords:
Phasor
Frequency domain
Fluorescence lifetimes
Solvent relaxation
FRET

ABSTRACT

The phasor method of treating fluorescence lifetime data provides a facile and convenient approach to characterize lifetime heterogeneity and to detect the presence of excited state reactions such as solvent relaxation and Förster resonance energy transfer. The method uses a plot of $M \sin(\Phi)$ versus $M \cos(\Phi)$, where M is the modulation ratio and Φ is the phase angle taken from frequency domain fluorometry. A principal advantage of the phasor method is that it provides a model-less approach to time-resolved data amenable to visual inspection. Although the phasor approach has been recently applied to fluorescence lifetime imaging microscopy, it has not been used extensively for cuvette studies. In the current study, we explore the applications of the method to in vitro samples. The phasors of binary and ternary mixtures of fluorescent dyes demonstrate the utility of the method for investigating complex mixtures. Data from excited state reactions, such as dipolar relaxation in membrane and protein systems and also energy transfer from the tryptophan residue to the chromophore in enhanced green fluorescent protein, are also presented.

Fluorescence methodologies are increasingly used in the chemical, physical, and biological sciences. This increase in popularity is due to improved instrumentation as well as novel probe chemistries and, in biological applications, to the introduction of molecular biological methodologies, including recombinant fluorescent proteins. During recent years, the use of fluorescence in analytical applications has grown in importance and is commonly used to detect and characterize sample heterogeneity in many chemical, physical, and biological systems. Examples of such applications in chemistry include analysis of dissolved organic matter (e.g., polycyclic aromatic hydrocarbons) in air particulates [1,2], in human hair [3], in oil and water samples [4], in foods [5], and in coal-derived extracts [6]. Fluorescence heterogeneity analysis has also been applied in studies of nanotechnology [7], surface chemistry [8], and bacteria identification [9], whereas in biological fields fluorescence heterogeneity analysis is important in many areas such as studies of intrinsic protein fluorescence [10,11], biological membranes [12,13], nucleic acids [14], and calcium gradients [15]. Traditional approaches to detecting and evaluating heterogeneous emitting samples include the use of excitation and emission spectra, such as excitation–emission matrices (EEMs)[1] [16,17], and synchronous scanning methods [18]. In addition to steady state fluorescence parameters, excited state lifetimes are also important in quantification of the nature and extent of sample heterogeneity [19,20]. An interesting recent example of the use of steady state and time-resolved fluorescence to characterize the heterogeneity in a mixture of fluorophores was presented by Smyk et al. [21], who studied the fluorescence from borage oils that contain polyunsaturated fatty acids. The purpose of their study was to establish, using spectroscopic methods as opposed to chromatographic ones, the presence of polyunsaturated fatty acids of varying extents of conjugation.

Excited state lifetimes have traditionally been measured using either the *impulse* or *harmonic* response method, also known as the "time domain" or "frequency domain", respectively [19,20,22]. In principle, both methods have the same information content because they can be interconverted using Fourier transforms [23]. In the impulse method, the sample is illuminated with a short pulse of light and the intensity of the emission versus time is recorded.

* Corresponding author. Address: Department of Cell and Molecular Biology, John A. Burns School of Medicine, University of Hawaii, 651 Ilalo Street, Biosciences 222, Honolulu, HI 96813, USA. Fax: +1 808 692 1968.
E-mail address: djameson@hawaii.edu (D.M. Jameson).

[1] *Abbreviations used:* EEM, excitation–emission matrix; LED, light-emitting diode; FRET, Förster resonance energy transfer; FLIM, fluorescence lifetime imaging microscopy; EDTA, ethylenediaminetetraacetic acid; DENS, 2-diethylamino-5-naphthalenesulfonic acid; LAURDAN, 6-dodecanoyl-2-(*N*,*N*-dimethylamino)naphthalene; IAEDANS, 5-[(2-iodoacetyl)-amino]naphthalene-1-sulfonic acid, sodium salt; DMPC, 1,2-dimyristoyl-*sn*-glycero-3-phosphocholine; EGFP, enhanced green fluorescent protein; SUV, small unilamellar vesicle; FWHM, full-width half-maximum; TNS, 2-*p*-toluidinyl-6-napthoyl-4′-cyclohexane carboxylic acid; DANCA, 2-dimethylamino-6-naphthoyl-4′ cyclohexane carboxylic acid; ANS, 1-anilinonaphthalene-8-*sulfonate*; UV, ultraviolet.

0003-2697/$ - see front matter © 2010 Elsevier Inc. All rights reserved.
doi:10.1016/j.ab.2010.11.010

Modern laser sources can now routinely generate pulses with widths on the order of picoseconds or shorter. In the harmonic method (also known as the phase and modulation approach), a continuous light source is typically used, such as a CW laser or xenon arc, and the intensity of this light source is modulated sinusoidally at high frequency. Often an electro-optic device, such as a Pockels cell, is used to modulate the light source. Alternatively, light-emitting diodes (LEDs) or laser diodes can be directly modulated [24]. Frequency domain methods have also been realized using the harmonic content of pulsed sources [25,26].

Both the time domain and frequency domain methods provide information on the excited state decay of a fluorophore. Data analysis of a fluorophore with a single lifetime component is straightforward. More sophisticated data analysis, such as fitting to a specific decay model or using the model-independent maximum entropy method [27], is required when the emission is heterogeneous. Emission heterogeneity could be due to the presence of multiple fluorophores (each giving rise to different exponential decays), excited state processes (e.g., solvent relaxation or Förster resonance energy transfer [FRET]), or nonexponential decays due to processes such as transient quenching. Models used to fit multiexponential decays are usually based on discrete exponential components or continuous distribution functions [10,19,20]. An alternative model-less approach to fluorescence lifetime determinations, called the phasor plot method, was introduced in 1984 by Jameson et al. [28]. A few years later, the phasor approach was used to correct phase and modulation lifetime measurements for background fluorescence [29]. The phasor approach to fluorescence lifetime analysis was largely dormant until recently, when several laboratories resurrected this approach and applied it to microscopy, for example, for studies on live cells using fluorescence lifetime imaging microscopy (FLIM) [30–36]. These FLIM/phasor studies (also termed AB or polar plots) have largely been focused on FRET systems, although recently they have been applied to study and characterize cell autofluorescence [37]. The phasor approach has not, however, been used extensively for cuvette studies, although some quenching studies in cuvettes have appeared [38]. In the current study, and in an accompanying article, we explore the application of the phasor method to cuvette studies and demonstrate its ability to evaluate and characterize fluorescence heterogeneity with in vitro samples to distinguish excited state reactions and to monitor photophysical processes.

Experimental

Brief theory of frequency domain fluorometry

In frequency domain fluorometry, a continuous wave light source, such as a laser or xenon arc lamp with a Pockels cell or directly modulating LED or laser diodes, is typically used to excite the sample; this light source is sinusoidally modulated at high frequencies (typically from hundreds of kHz to hundreds of MHz) such that the excitation intensity is described by

$$E(t) = E(0)[1 + M_E \sin(\omega t)], \quad (1)$$

where $E(t)$ and $E(0)$ are the excitation intensities at times t and 0, respectively, M_E is the modulation of the excitation ($M_E = AC_E/DC_E$), and ω is the angular modulation frequency (equal to $2\pi f$, where f is the modulation frequency). The fluorescence emission will then consist of an intensity that is also sinusoidally modulated having the same frequency as the excitation light but shifted in phase and demodulated. If the fluorescence decay is a single exponential, $e^{-t/\tau}$, where τ is the fluorescence lifetime, the sinusoidal fluorescence emission is described by

$$F(t) = F(0)[1 + M_F \sin(\omega t + \phi)], \quad (2)$$

where $F(t)$ and $F(0)$ are the fluorescence intensity at times t and 0, respectively, M_F is the modulation of the fluorescence ($M_F = AC_F/DC_F$), and ϕ is the phase delay of the fluorescence emission. The measured components in the frequency domain are the phase delay between excitation and emission (ϕ) and the demodulation, which can be related to the lifetime using the following equations:

$$\tan\phi = \omega\tau_p \quad (3)$$

$$M = M_F/M_E = (1 + \omega^2\tau_m^2)^{-1/2}, \quad (4)$$

where τ_p and τ_m are the phase and modulation lifetimes, respectively. For a fluorescent system that has only a single lifetime, these values will be identical. In the case of a system with multiple lifetimes, the measured τ_p will be less than the measured τ_m. The relationship between ϕ and squared amplitude (M^2) for a mixture of sinusoidal components is described below (the derivations can be found in Refs. [23,39]):

$$\tan\phi = \sum f_i M_i \sin\phi_i \Big/ \sum f_i M_i \cos\phi_i \quad (5)$$

$$M^2 = \left(\sum f_i M_i \sin\phi_i\right)^2 + \left(\sum f_i M_i \cos\phi_i\right)^2, \quad (6)$$

where f_i is the fractional photocurrent of the ith component with modulation M_i and phase ϕ_i. (Note that in the case of frequency domain measurements, the intensity fraction corresponds to the fraction of the photocurrent at the particular modulation frequency used and should not be confused with the preexponential function typically used in time domain fluorometry.)

Phasor plots

Jameson et al. [28] described a method of graphically representing phase and modulation data that we have redrawn in Fig. 1A. In

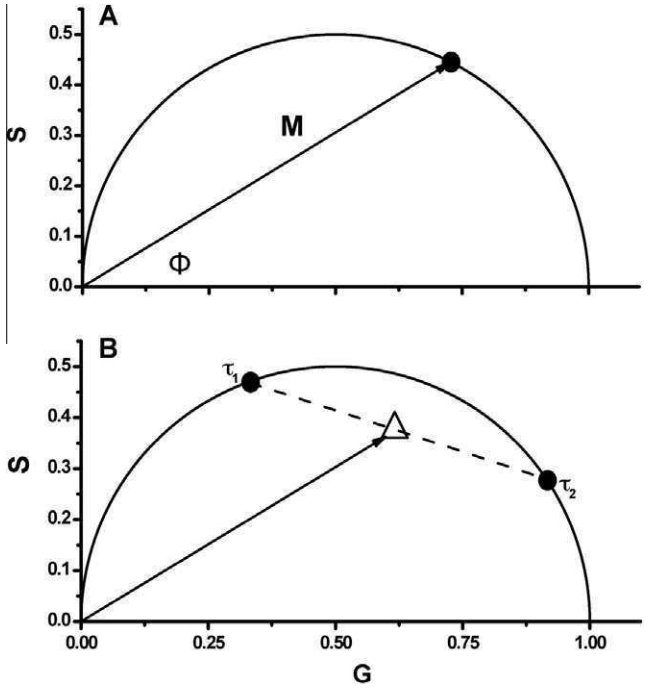

Fig.1. (A) Schematic illustration of the basic concepts of phasor plots. (B) Two different fluorophores with lifetimes of τ_1 and τ_2, where $\tau_1 > \tau_2$, and their hypothetical mixtures. The dashed line represents the set of mixtures. The solid line illustrates vector M with phase shift Φ, which corresponds to the mixture, where the ratio of the fluorescence contributions between both fluorophores is 1:1. Note that increased fluorescence contribution from the fluorophore with fluorescence lifetime τ_1 results in an increased angle Φ and decreased modulation M and also moves the phasor point closer to that of τ_1.

this figure, the vector has a length equal to the modulation (M) and makes an angle with the x axis equal to the phase delay (ϕ). The x and y coordinates of this vector are derived from Eqs. (5) and (6), and using Weber's notation [23],

$$x = G = M\cos\phi \tag{7}$$

$$y = S = M\sin\phi. \tag{8}$$

For a single-exponential decay, this vector describes a semicircle of radius ½ with a center at (1/2, 0) due to the relationship

$$M = \cos\phi. \tag{9}$$

Therefore, a fluorophore characterized by a single lifetime will always give rise to a phasor point that falls on this semicircle, typically referred to as the universal circle (Fig. 1A). The phasor points for fluorophores that decay with multiple or nonexponential lifetimes are constrained within the universal circle, as described by Eqs. (7) and (8). The location of the phasor point for heterogeneous emitting systems, or multiple single lifetime fluorophores, is the intensity-weighted average of the separate lifetime decay components as described below (Fig. 1B):

$$G_{\text{tot}} = \sum f_i M_i \cos\phi_i \tag{10}$$

$$S_{\text{tot}} = \sum f_i M_i \sin\phi_i. \tag{11}$$

The derivations of the equations and graphical representation have been described previously [28,29,32,36]. In a system containing two decay components, the phasor point will be located on the line between the individual decay vectors weighted by the intensity of each component. Therefore, lifetime heterogeneity within a system will place the phasor point within the universal circle, as illustrated in Fig. 1B.

Although up to this point the mathematical treatment for converting data to a phasor plot has been given using the frequency domain method (which is the method used in this study), raw data from the time domain method can also be analyzed via phasor plots [35]. The equations used to transform the data to the phasor plot from the raw time domain data, originally presented by Weber [23], are

$$\begin{aligned} G(\omega) &= \int_0^\infty I(t)\cos(\omega t)dt \Big/ \int_0^\infty I(t)dt \\ S(\omega) &= \int_0^\infty I(t)\sin(\omega t)dt \Big/ \int_0^\infty I(t)dt, \end{aligned} \tag{12}$$

where ω can be chosen as the repetition frequency of the pulsed excitation source or another value that depends on the kinetics of the excited state process under investigation. We have outlined a script in MATLAB that can be used to convert/visualize time domain data as a phasor plot in Appendix A. We note that calculations of phasors from frequency or time domain data are carried out by the Globals for Images (aka Sim FCS) software package from the Laboratory for Fluorescence Dynamics (http://www.lfd.uci.edu).

Materials and methods

Materials

Rhodamine B, dimethyl POPOP, Hepes, NaCl, ethylenediaminetetraacetic acid (EDTA), *p*-terphenyl, fluorescein, spectrophotometric-grade ethanol, and glycerol were purchased from Sigma–Aldrich (St. Louis, MO, USA). 2-Diethylamino-5-naphthalenesulfonic acid (DENS) was synthesized by the method of Weber [40]. 6-Dodecanoyl-2-(*N*,*N*-dimethylamino)naphthalene (LAURDAN) and 5-[(2-iodoacetyl)-amino]naphthalene-1-sulfonic acid, sodium salt (IAEDANS) were obtained from Invitrogen (Carlsbad, CA, USA). 1,2-Dimyristoyl-*sn*-glycero-3-phosphocholine (DMPC) was obtained from Avanti Polar Lipids (Alabaster, AL, USA). Enhanced green fluorescent protein (EGFP) was a generous gift from Joseph Albanesi.

Vesicle formation

Small unilamellar vesicles (SUVs) were prepared by mixing DMPC (in chloroform/methanol) with the fluorescent dye LAURDAN dissolved in methanol such that the final concentration of lipids was 1 mM and the dye-to-lipid ratio was approximately 1:200. (The concentration of LAURDAN was determined using a molar extinction coefficient of 20,000 M^{-1} cm^{-1} (362 nm) [41].) The mixture was dried for 10 min under nitrogen and then kept under vacuum for approximately 2 h. The dried lipid film was dissolved in 10 mM Hepes (pH 7.4) with 150 mM sodium chloride and 2 mM EDTA, heated to 30–35 °C, and vortexed for 2 min. The cloudy solution was sonicated for 15 min in a G112 SPIT sonicator bath (Laboratory Supplies, Hicksville, NY, USA), resulting in an optically clear solution. The samples were stored at 4 °C and used within 3 days.

Multifrequency lifetime measurements

Fluorescence lifetime measurements were obtained on a ChronosFD Spectrofluorometer (ISS, Champaign, IL, USA). Fluorophores were excited with a 280-nm LED, a 375-nm laser diode, or a 471-nm laser diode with polarizers on the excitation and emission side set to magic angles [42]. The bandpass filters FF01-280/20-25, F01-375/6-25, and FF01-482/18-25 (Semrock, Rochester, NY, USA) were placed after the corresponding excitation source to eliminate spurious light, and the emission was observed through a 420-, 470-, or 525-nm longpass filter. A circulating water bath (Fisher Scientific, Pittsburgh, PA, USA) was used to maintain the temperature. *p*-Terphenyl dissolved in ethanol (1.05 ns), dimethyl POPOP dissolved in ethanol (1.45 ns), and fluorescein dissolved in 0.01 M NaOH (4.05 ns) were used as lifetime references [20].

TNS decay when bound to apomyoglobin

This section involves the reanalysis of data reported previously [43]. Briefly, lifetime data were obtained on a multifrequency phase and modulation fluorometer [44] with modulation frequencies between 10 and 150 MHz. Samples were excited at 327 nm, and emission was monitored through a 510 (±2)-nm interference filter (10 nm full-width half-maximum [FWHM]). 2-*p*-Toluidinyl-6-napthoyl-4′-cyclohexane carboxylic acid (TNS, Molecular Probes, Eugene, OR, USA) was added to apoprotein at a molar concentration of less than 1:50 (probe/protein) to minimize nonspecific binding.

Results and discussion

Mixtures of fluorophores

One of the original motivations of this work was to develop a method that could be used to study mixtures of fluorophores for analytical purposes, that is, to be able to facilely compare different mixtures in such a way that differences in the fluorophore composition would be readily apparent. As mentioned above, a mixture of two monoexponential fluorophores with different fluorescence lifetimes, or a fluorophore characterized by a multiexponential decay, will produce a phasor point within the universal circle, indicating lifetime heterogeneity. The theoretical basis of the phasor plot analysis indicates that this measured phasor point will be located on a line between the points of the individual fluorophores or single-exponential components. Therefore, when three dyes are

combined in solution, the resulting phasor point should be found constrained within a triangle that has vertices defined by the location of the phasor of the individual dyes. Binary and tertiary fluorophore mixtures were studied using fluorophores in ethanol with widely separated lifetimes, namely DENS (fluorescence lifetime $\tau = 29.9$ ns), IAEDANS ($\tau = 5.3$ ns), and Rhodamine B ($\tau = 1.7$ ns). Fig. 2 shows the phasor data at 20 MHz of each individual fluorophore (black dots), solutions containing a mixture of two dyes (DENS/IAEDANS, DENS/Rhodamine B, and IAEDANS/Rhodamine B), and a mixture of all three dyes. As expected, the individual fluorophore's phasor points are located along the universal circle, whereas the phasor points corresponding to mixtures of any two dyes fall on a line between the points on the universal circle corresponding to the individual dyes. For the mixture of the three dyes, the phasor point is located within the triangle defined by the three dual fluorophore mixture lines. The linearity of the summation of multiple fluorescing species (Eqs. (10) and (11)) makes the phasor method suited to the investigation of complex mixtures. We should note, from Fig. 2, that a quantitative extrapolation of exponentials can be used if the location of one component in a mixture is known. If the phasor point of a binary mixture of single-exponential decays is inside the universal circle, and if one of the single-exponential components is known, then the lifetime value of the second component can be determined from the intercept, on the universal circle, of the line between the mixture and the known phasor point. The fractional contribution of each species can be calculated from the relative distance between the phasor point of the pure species and that of the mixture. This analysis can, in theory, be extended to multiple species with multiple lifetime components provided that enough phasor points have been determined. In other words, for the previous case of a binary mixture where one lifetime value is known, this leaves two unknown quantities (τ_2 and f_2; recall that $f_1 = 1 - f_2$) with two independent measurements, resulting in a perfectly determined system of equations. As more unknown quantities arise for more complex samples (with more lifetimes and fractions), more modulation frequencies would be required to determine these additional parameters. However, the errors associated with these measurements can significantly decrease the accuracy of these determinations [45]. We also note that these types of considerations, and the effect of Gaussian lifetime distributions on phasor points, have been discussed by Redford and Clegg [32].

The effect of modulation frequency on the location of the phasor point was also examined. As the modulation frequency is increased, the measured data should have both a decrease in M and an increase in the Φ, causing the phasor point to move counterclockwise along/within the universal circle. Fig. 3 demonstrates this change in the position of the phasor points for the fluorophore mixtures DENS, IAEDANS, and Rhodamine B when the frequency is increased from 15 MHz (circles) to 30 MHz (triangles). Because frequency domain data are typically obtained using numerous (10–15) modulation frequencies, one can choose among a set of phasor points to find the modulation frequencies that lead to the optimal placement or separation of the phasor points for the particular application. Therefore, the use of widely spaced modulation frequencies could be used in turn to selectively weight one of the fluorescing species in an unknown mixture. Such selection would provide information regarding the phasor locations of each species in the solution.

Dipolar solvent relaxation

In the presence of excited state reactions, such as dipolar solvent relaxation and FRET, phasor data points can fall outside of the universal circle [32]. Alterations in the emission properties of a fluorophore can occur in response to solvent dynamics. In the ground state, fluorophores often have a permanent dipole moment, the strength and direction of which depend on the structure and electronic aspects of the molecule. Immediately after the absorption of a photon, electronic reorganization within the molecule occurs, often resulting in a dipole moment with a different orientation and magnitude. As such, solvent molecules possessing dipoles in proximity to the excited fluorophore dipole are no longer in an equilibrium state and will reorient about the excited state dipole to decrease the energy of the system. If the time of this solvent dipole rearrangement is comparable to or shorter than the excited state lifetime, then solvent reorientation will result in a red shift of the emission, that is, to a lower energy excited state. The time required for the solvent molecules to rearrange depends on the polarity and viscosity of the solvent, with higher viscosity solvents taking longer times to reach their minimum free energy states. In frequency domain fluorometry, solvent relaxation is characterized by an increased phase delay of the emission from the relaxed state relative to emission from the unrelaxed state due to the time it takes for the surrounding solvent molecules to reorient around the newly created excited state fluorophore dipole [46]. This phase delay can result in movement of the phasor point to a position outside of the universal circle. A family of naphthalene-based fluorophores—LAURDAN, and 2-dimethylamino-6-naphthoyl-4′-cyclohexane carboxylic acid (DANCA), designed by Weber

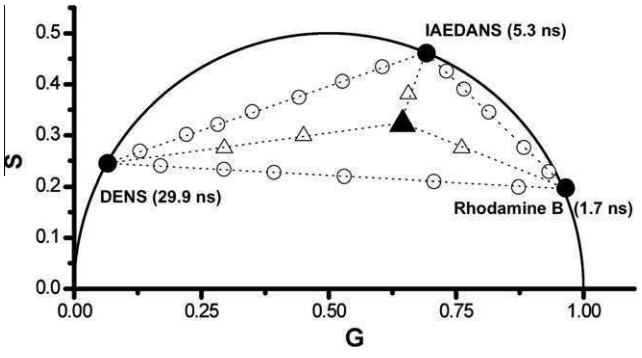

Fig.2. Phasor data corresponding to ethanol solutions of three fluorophores, each of which is characterized by a single-exponential decay. Closed circles correspond to the individual fluorophores. Open circles between individual fluorophores show the mixture, with changing contributions to the photocurrent, of two particular fluorophores. The closed triangle corresponds to a mixture of all three fluorophores at an equal photocurrent contribution. Increasing the fluorescence contribution of one of the components moves the points closer to the specific corner of the triangle (open triangles). All data were collected at a modulation frequency of 20 MHz and 25 °C.

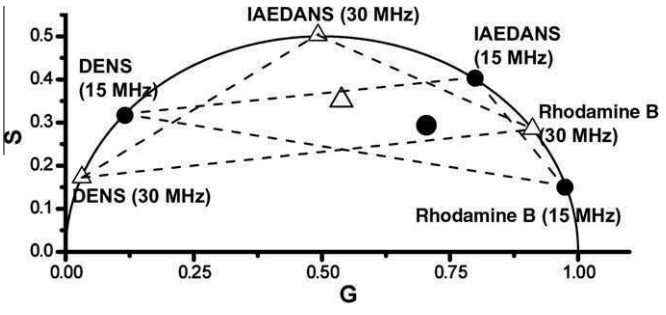

Fig.3. Frequency dependence on the location of phasor points for DENS, IAEDANS, and Rhodamine B alone and in various mixtures. Circles correspond to individual fluorophores at 15 MHz, whereas triangles correspond to individual fluorophores recorded at 30 MHz. Dashed lines between circles and triangles represent the two-component mixture of varying contributions between corresponding fluorophores. The larger circle and triangle in the middle represent mixtures of all three fluorophores, with an equal contribution to the photocurrent from each, at 15 MHz (circle) and 30 MHz (triangle). All data were measured with 375 nm excitation at 25 °C.

[47]—are characterized by particularly large excited state dipoles, and this renders them well-suited to causing dipolar relaxation in appropriate systems.

Dipolar relaxation in vesicles

Dipolar relaxation can occur in heterogeneous systems such as membranes and proteins where the "solvent" molecules are lipids (or water molecules that penetrate into the lipid phase) and amino acid residues, respectively. In these cases, the presence of relaxation processes can provide an indication of the underlying dynamics of the biomolecule under investigation. An example of such relaxation processes for probes embedded in DMPC SUVs is the emission spectra of LAURDAN over a range of temperatures (data not shown). At temperatures below the transition temperature (23 °C [48]), the emission maximum is approximately 440 nm, whereas at higher temperatures, the maximum shifts to approximately 480 nm. At 30 °C, there is a broad peak from 450 to 475 nm, demonstrating the presence of both gel and liquid crystalline phases. In the case of the LAURDAN/DMPC system, the spectral shifts are attributed to the fact that the liquid crystalline lipid phase allows penetration of the water molecules into the bilayer, which is responsible for the dipolar relaxation mechanism [49,50].

Inspection of the LAURDAN/DMPC phasor plot (Fig. 4) shows that the phasor points corresponding to data collected using the 470-nm filter are completely outside of the universal circle, indicative of a dipolar solvent relaxation mechanism. When the entire LAURDAN emission is collected using the 420-nm longpass filter, the phasor points lay along or very close to the universal circle, indicating that the nonrelaxed emission dominates the observed decay. Using the 470-nm longpass filter, the collected emission is weighted primarily from the molecules that undergo dipolar relaxation and the location of the phasor points outside of the universal circle is more pronounced. However, the points above 25 °C show a clear trend above the universal circle, indicating the presence of an excited state event. We should note that the LAURDAN phasor data presented here support the dipolar relaxation models for LAURDAN/vesicle systems [49,50] as opposed to other models [51]. In principle, the phasor plots allow calculation of the rates of dipolar relaxation processes in such systems, but this analysis is beyond the scope of the current study.

TNS with apomyoglobin

Fluorescent molecules, such as 1-anilinonaphthalene-8-*sulfonate* (ANS), TNS, and DANCA, have been used in a number of protein systems to investigate dynamic characteristics of the protein matrix [43,52–54]. In the excited state, the dipole moments of such fluorophores associated with proteins can cause rearrangements of charges and dipoles in the protein matrix, for example, due to charged or polar amino acid side chains or even the dipoles associated with the peptide bonds. If the dynamics of the protein allows for dipolar relaxation of the protein matrix, then distinct alterations in the fluorophore's emission properties can result, analogous to the case of dipolar relaxation of solvent molecules described above. Bismuto et al. [43] compared the emission properties of TNS associated with both sperm whale and tuna apomyoglobin to ascertain whether this probe revealed differences in the heme-binding sites of these phylogenetically related proteins. In the original publication, it was documented that the phase and modulation lifetimes for TNS/tuna myoglobin decreased with increasing frequencies, indicative of heterogeneous emitting population, whereas for TNS/sperm whale myoglobin the phase lifetime became longer than the modulation lifetime with increasing frequency (going negative at the highest frequency). This latter case was concluded to be an excited state reaction, specifically dipolar relaxation within the heme-binding pocket. Time-resolved data could not detect the presence of dipolar relaxation in TNS/tuna myoglobin despite steady state fluorescence data that suggested its presence. The authors concluded that although dipolar relaxation is likely occurring in both proteins, the structural heterogeneity in the heme-binding pocket of tuna myoglobin produces some microenvironments that are not favorable to dipolar relaxation of the TNS molecule.

The phase and modulation data of TNS with apomyoglobin from Bismuto et al.'s study [43] are reproduced in Fig. 5 using the phasor approach. The resultant phasor plot shows distinct differences between the two data sets, with the tuna TNS/apomyoglobin data entirely within the universal circle. TNS in a homogeneous isotropic solvent decays with a single exponential; thus, the multiexponential decay of the tuna apomyoglobin is suggestive of different populations, and hence lifetime heterogeneity, of local probe environments. Although there may be dipolar relaxation in this system, the lifetime heterogeneity keeps the phasor points within the universal circle. In the case of TNS bound to sperm whale apomyoglobin, however, many of the phasor points are outside of the universal circle, and hence an excited state reaction, attributed to dipolar relaxation, is evident. The heterogeneity in the phasor points of TNS/tuna myoglobin suggests multiple conformations of TNS when bound as compared with when bound to sperm whale myoglobin. Thus, it can be concluded that there is more flexibility in the pocket of tuna myoglobin. These conclusions are in line with those made by Bismuto et al. [43].

Energy transfer

FRET is one of the most popular fluorescence techniques in the biological sciences [19,20]. Unlike the crystallographic technique,

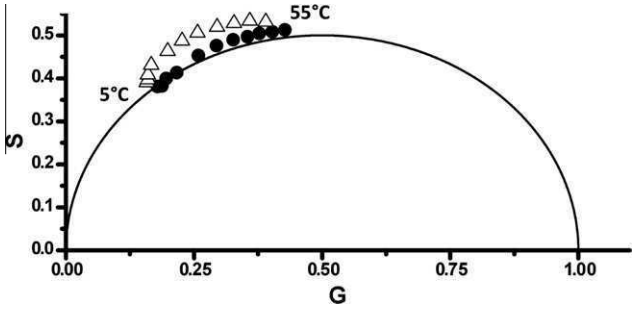

Fig.4. LAURDAN in DMPC vesicles. Circles and triangles represent data collected for temperatures between 5 °C (left) and 55 °C (right), with 5 °C intervals, at modulation frequencies of 55 MHz (circles) and 57 MHz (triangles). Excited at 375 nm; emission was viewed through 420-nm (circles) and 470-nm (triangles) longpass filters.

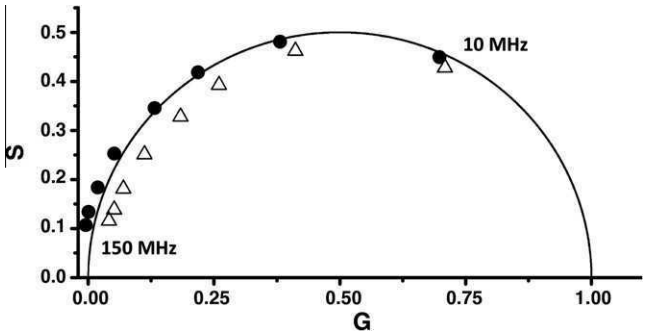

Fig.5. Phasor data for sperm whale TNS/apomyoglobin (circles) and tuna TNS/apomyoglobin (triangles) adducts (modulation frequencies from 10 to 150 MHz [right to left]). Phase and modulation data were taken from Ref. [43].

FRET can provide structural information rapidly and facilely in solution, at low concentrations, and has the potential to report on intermediate or short-lived conformations of proteins [55,56]. Changes in the fluorescence emission from a donor molecule, measured by either the steady state or time-resolved method, in the absence and presence of an acceptor fluorophore (either different from or identical to the donor) can, in turn, be used to estimate distances [19], although the method is subject to caveats such as the precise orientation of donor and acceptor. FRET between a donor, with a single lifetime component, and an acceptor molecule will result in a shortening of the donor lifetime. In a phasor plot, this circumstance will cause the phasor point of the donor to move along the universal circle [35,57]. If there is an unequal ratio of donor to acceptor (donor > acceptor), then a small number of donors will maintain the original lifetime, producing a heterogeneous decay. Phasor analysis of such a sample would produce a point with a shorter average lifetime than the donor alone; however, the point would fall inside the universal circle. Alternatively, the acceptor decay can be monitored through direct excitation or through transfer from an excited donor. Any difference between the phasor points of the acceptor, directly excited or from donor transfer, would be the result of energy transfer. The decay from the acceptor, after energy transfer, should be longer than if the acceptor were directly excited due to the time delay from absorption by the donor, energy transfer between the donor/acceptor pair, and the subsequent emission from the acceptor. This delay is manifested as a lengthening of the measured phase, and such a delay will move the phasor point outside of the universal circle (see, e.g., Refs. [57,58]). Fig. 6 shows the phasor points associated with the visible emission (>525 nm) from EGFP, excited with both visible (471 nm) and ultraviolet (UV, 280 nm) excitation, as a function of modulation frequency (16–300 MHz). As is evident for the phasor plot, 471 nm excitation results in phasor points corresponding to single-exponential decays; that is, the points are all on the universal circle. On the other hand, 280 nm excitation, which will directly excite the single tryptophan residue (as well as the tyrosine residues) in addition to some direct excitation of the EGFP chromophore, results in phasor points that are all outside of the universal circle. Hence, although some of the visible chromophores may be directly excited at 280 nm, there is enough tryptophan-to-chromophore energy transfer to move the phasor point outside of the universal circle. This observation is consistent with the observation by Visser et al. [59] on energy transfer in a fluorescent protein. This demonstration illustrates the utility of the phasor method to visualize photophysical processes and to provide insights into excited state kinetics that are often difficult to obtain by other methods. We note that FRET efficiencies can also be calculated, in principle, from phasor data; the Globals for Images (aka Sim FCS) software mentioned earlier carries out these calculations.

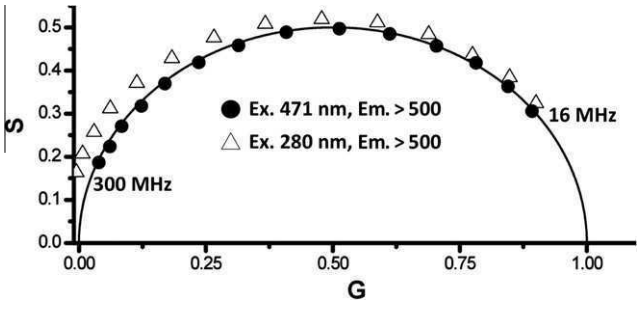

Fig.6. Decay data of EGFP excited at 471 nm (circles) and 280 nm (triangles). All of the data recorded with 280 nm excitation fall outside of the universal circle, an indication of an excited state process, allowing a simple visualization of the energy transfer process between the lone tryptophan (donor) and the EGFP chromophore (acceptor).

Reproducibility

We established, through simulations, data, and test samples, that in our instrument the statistical errors between individual phasor measurements are on the order of ±0.005 for both *G* and *S* values (data not shown). We can then have confidence that movement of the phasor point by approximately 0.01 on the *G* or *S* axis constitutes a statistically significant change.

Conclusion

We have demonstrated that the extension of the phasor method from FLIM to cuvette measurements provides a method that complements other approaches and that, in some cases, provides insights that would otherwise be difficult to obtain. In particular, the method allows facile analysis of sample heterogeneity and ready identification of excited state processes such as dipolar relaxation and FRET. In our next article, we will specifically demonstrate the application of the phasor method to protein studies, including protein–ligand and protein–protein interactions as well as protein unfolding.

Acknowledgments

This work was supported in part by funding from Allergan and from National Institutes of Health Grant RO1GM076665 (D.M.J.). M. Štefl was supported by the Ministry of Education of the Czech Republic via Grant LC06063 and by Charles University in Prague via Fond Mobility. We thank Joseph Albanesi for supplying the EGFP.

Appendix A. Conversion of time domain data to phasors

Throughout the article, we describe how raw data from frequency domain measurements can be converted to phasor plots. Yet raw data from both time domain and frequency domain lifetime measurements can be converted to phasor plots. We have outlined lines of code (below), which can be used in MATLAB, for the conversion of raw time domain data into a phasor plot. We also note that the software package Globals for Images (aka Sim FCS), available from the Laboratory for Fluorescence Dynamics (http://www.lfd.uci.edu), can use frequency or time domain data to construct phasor plots.

```
function [G,S] = plottcspcphasor(decay,ref,ref_tau,freq,delta_t)
%decay is the array of the decay curve from TCSPC
%ref is the decay curve of the reference or IRF curve
%ref_tau is the lifetime of the reference compound (zero for IRF)
%freq is the freq domain freq you want to use to plot the phasor
%delta_t is the size (time) of each of the bins of the decay curve
w=2*pi*freq;
%calculate ref phasor
Gn_ref=0;
Sn_ref=0;
area_ref=0;
for bin = 1:length(ref)-1
   Gn_ref = Gn_ref + ref(bin).*cos(w*delta_t.*(bin-.5))*delta_t;
   Sn_ref = Sn_ref + ref(bin).*sin(w*delta_t.*(bin-.5))*delta_t;
   area_ref = area_ref + (ref(bin) +ref(bin+1)).*delta_t./2;
end
G_ref = Gn_ref./area_ref;
S_ref = Sn_ref./area_ref;
%calculate phase and modulation corrections
M_ref = (1 + (w*ref_tau).^2).^(-0.5);
ph_ref = atan(w*ref_tau);
```

```
M_cor = sqrt(G_ref.^2+S_ref.^2)./M_ref;
ph_cor = -atan2(S_ref,G_ref)+ph_ref;
%calculate data phasor
Gn=0;
Sn=0;
area=0;
for bin = 1:length(decay)-1
   Gn = Gn + decay(bin).*cos(w*delta_t.*(bin-.5))*delta_t;
   Sn = Sn + decay(bin).*sin(w*delta_t.*(bin-.5))*delta_t;
   area = area + (decay(bin) +decay(bin+1)).*delta_t./2;
end
Gdec = Gn./area;
Sdec = Sn./area;
G = (Gdec.*cos(ph_cor) - Sdec.*sin(ph_cor))./M_cor;
S = (Gdec.*sin(ph_cor) + Sdec.*cos(ph_cor))./M_cor;
%Plot phasor point and universal circle
theta = 0:0.01:pi;
plot(0.5+0.5*cos(theta),0.5*sin(theta));
axis([0 1 0 1]);
axis square;
hold on;
xlabel('G')
ylabel('S')
plot(G,S,'b*')
```

The above code calculates the phasor location of a known reference decay curve or the instrument response function (IRF) and then determines the transformation of the point to the appropriate phasor point ((1,0) for the IRF). This transformation consists of a correction to the amplitude (modulation) and a rotation about the origin (phase). The reference decay curve is the complete decay curve of a compound with a known single-exponential lifetime, for example, fluorescein in 0.01 M NaOH (4.05 ns) or *p*-terphenyl in ethanol (1.05 ns). Note that, unlike the background subtraction method in the frequency domain, this correction method is *not* an addition or subtraction of a phasor vector but rather a rotation and rescaling of the phasor.

References

[1] M. Akyuz, H. Cabuk, Particle-associated polycyclic aromatic hydrocarbons in the atmospheric environment of Zonguldak, Turkey, Sci. Total Environ. 405 (2008) 62–70.

[2] Y. Hashi, T.R. Wang, W. Du, J.M. Lin, Rapid and sensitive determination of polycyclic aromatic hydrocarbons in atmospheric particulates using fast high-performance liquid chromatography with on-line enrichment system, Talanta 74 (2008) 986–991.

[3] A. Toriba, Y. Kuramae, T. Chetiyanukornkul, R. Kizu, T. Makino, H. Nakazawa, K. Hayakawa, Quantification of polycyclic aromatic hydrocarbons (PAHs) in human hair by HPLC with fluorescence detection: a biological monitoring method to evaluate the exposure to PAHs, Biomed. Chromatogr. 17 (2003) 126–132.

[4] S.A. Bortolato, J.A. Arancibia, G.M. Escandar, Non-trilinear chromatographic time retention–fluorescence emission data coupled to chemometric algorithms for the simultaneous determination of 10 polycyclic aromatic hydrocarbons in the presence of interferences, Anal. Chem. 81 (2009) 8074–8084.

[5] R. Rodriguez-Acuna, C. Perez-Camino Mdel, A. Cert, W. Moreda, Sources of contamination by polycyclic aromatic hydrocarbons in Spanish virgin olive oils, Food Addit. Contam. A 25 (2008) 115–122.

[6] T. Katoh, S. Yokoyama, Y. Sanada, Analysis of a coal-derived liquid using high-pressure liquid chromatography and synchronous fluorescence spectrometry, Fuel 59 (1980) 845–850.

[7] D. Tasis, J. Mikroyannidis, V. Karoutsos, C. Galiotis, K. Papagelis, Single-walled carbon nanotubes decorated with a pyrene–fluorenevinylene conjugate, Nanotechnology 20 (2009) 135606.

[8] W.B. Williams, B.A. Mullany, W.C. Parker, P.J. Moyer, M.H. Randles, Using quantum dots to tag subsurface damage in lapped and polished glass samples, Appl. Opt. 48 (2009) 5155–5163.

[9] H. Bhatta, E.M. Goldys, R.P. Learmonth, Use of fluorescence spectroscopy to differentiate yeast and bacterial cells, Appl. Microbiol. Biotechnol. 71 (2006) 121–126.

[10] J.A. Ross, D.M. Jameson, Time-resolved methods in biophysics: 8. Frequency domain fluorometry—applications to intrinsic protein fluorescence, Photochem. Photobiol. Sci. 7 (2008) 1301–1312.

[11] N.G. James, J.A. Ross, A.B. Mason, D.M. Jameson, Excited-state lifetime studies of the three tryptophan residues in the N-lobe of human serum transferrin, Protein Sci. 19 (2009) 99–110.

[12] T. Parasassi, F. Conti, E. Gratton, O. Sapora, Membranes modification of differentiating proerythroblasts: variation of 1,6-diphenyl-1,3,5-hexatriene lifetime distributions by multifrequency phase and modulation fluorimetry, Biochim. Biophys. Acta 898 (1987) 196–201.

[13] R. Fiorini, M. Valentino, S. Wang, M. Glaser, E. Gratton, Fluorescence lifetime distributions of 1,6-diphenyl-1,3,5-hexatriene in phospholipid vesicles, Biochemistry 26 (1987) 3864–3870.

[14] R.M. Clegg, A.I. Murchie, A. Zechel, C. Carlberg, S. Diekmann, D.M. Lilley, Fluorescence resonance energy transfer analysis of the structure of the four-way DNA junction, Biochemistry 31 (1992) 4846–4856.

[15] A. Celli, S. Sanchez, M. Behne, T. Hazlett, E. Gratton, T. Mauro, The epidermal Ca^{2+} gradient: measurement using the phasor representation of fluorescent lifetime imaging, Biophys. J. 98 (2010) 911–921.

[16] G. Weber, Enumeration of components in complex systems by fluorescence spectrophotometry, Nature 190 (1961) 27–29.

[17] J. Chen, A. Lee, J. Zhao, H. Wang, H. Lui, D.I. McLean, H. Zeng, Spectroscopic characterization and microscopic imaging of extracted and in situ cutaneous collagen and elastic tissue components under two-photon excitation, Skin Res. Technol. 15 (2009) 418–426.

[18] R.J. Kavanagh, B.K. Burnison, R.A. Frank, K.R. Solomon, G. Van Der Kraak, Detecting oil sands process-affected waters in the Alberta oil sands region using synchronous fluorescence spectroscopy, Chemosphere 76 (2009) 120–126.

[19] B. Valeur, Molecular Fluorescence, Wiley–VCH, Weinheim, Germany, 2002.

[20] J. Lakowicz, Principles of Fluorescence Spectroscopy, Springer, New York, 2006.

[21] B. Smyk, R. Amarowicz, M. Szabelski, I. Gryczynski, Z. Gryczynski, Steady-state and time-resolved fluorescence studies of stripped borage oil, Anal. Chim. Acta 646 (2009) 85–89.

[22] F.V. Bright, T.A. Betts, K.S. Litwiler, Advances in multifrequency phase and modulation fluorescence analysis, Crit. Rev. Anal. Chem. 21 (1990) 389–405.

[23] G. Weber, Resolution of the fluorescence lifetimes in a heterogeneous system by phase and modulation measurements, J. Phys. Chem. 85 (1981) 949–953.

[24] B. Barbieri, E. Terpetschnig, D.M. Jameson, Frequency-domain fluorescence spectroscopy using 280-nm and 300-nm light-emitting diodes: measurement of proteins and protein-related fluorophores, Anal. Biochem. 344 (2005) 298–300.

[25] E. Gratton, D.M. Jameson, N. Rosato, G. Weber, Multifrequency cross-correlation phase fluorometer using synchrotron radiation, Rev. Sci. Instrum. 55 (1984) 486–494.

[26] J.R. Alcala, E. Gratton, F.G. Prendergast, Fluorescence lifetime distributions in proteins, Biophys. J. 51 (1987) 597–604.

[27] J.C. Brochon, Maximum entropy method of data analysis in time-resolved spectroscopy, Methods Enzymol. 240 (1994) 262–311.

[28] D.M. Jameson, E. Gratton, R.D. Hall, The measurement and analysis of heterogeneous emissions by multifrequency phase and modulation fluorometry, Appl. Spectrosc. Rev. 20 (1984) 55–106.

[29] G.D. Reinhart, P. Marzola, D.M. Jameson, E. Gratton, A method for on-line background subtraction in frequency domain fluorometry, J. Fluoresc. 1 (1991) 153–162.

[30] A.H. Clayton, Q.S. Hanley, D.J. Arndt-Jovin, V. Subramaniam, T.M. Jovin, Dynamic fluorescence anisotropy imaging microscopy in the frequency domain (rFLIM), Biophys. J. 83 (2002) 1631–1649.

[31] A.H.A. Clayton, Q.S. Hanley, P.J. Verveer, Graphical representation and multicomponent analysis of single-frequency fluorescence lifetime imaging microscopy data, J. Microsc. 213 (2004) 1–5.

[32] G.I. Redford, R.M. Clegg, Polar plot representation for frequency-domain analysis of fluorescence lifetimes, J. Fluoresc. 15 (2005) 805–815.

[33] Q.S. Hanley, A.H.A. Clayton, AB-plot assisted determination of fluorophore mixtures in a fluorescence lifetime microscope using spectra or quenchers, J. Microsc. 218 (2005) 62–67.

[34] A. Esposito, H.C. Gerritsen, T. Oggier, F. Lustenberger, F.S. Wouters, Innovating lifetime microscopy: a compact and simple tool for life sciences, screening, and diagnostics, J. Biomed. Opt. 11 (2006) 34016.

[35] M.A. Digman, V.R. Caiolfa, M. Zamai, E. Gratton, The phasor approach to fluorescence lifetime imaging analysis, Biophys. J. 94 (2008) L14–L16.

[36] A.H.A. Clayton, The polarized AB plot for the frequency-domain analysis and representation of fluorophore rotation and resonance energy homotransfer, J. Microsc. 232 (2008) 306–312.

[37] C. Stringari, M. Digman, P. Donovan, E. Gratton, Multiple components mapping of live tissue by phasor analysis of fluorescence lifetime imaging, Biophys. J. 98 (2010) 214a.

[38] G.I. Redford, Z.K. Majumdar, J.D. Sutin, R.M. Clegg, Properties of microfluidic turbulent mixing revealed by fluorescence lifetime imaging, J. Chem. Phys. 123 (2005) 224504.

[39] F.W.J. Teale, Phase and modulation fluorometry, in: R.B. Cundall, R.E. Dale (Eds.), Time-Resolved Fluorescence Spectroscopy in Biochemistry and Biology, Plenum, New York, 1983, pp. 59–80.

[40] G. Weber, Polarization of the fluorescence of macromolecules: II. Fluorescent conjugates of ovalbumin and bovine serum albumin, Biochem. J. 51 (1952) 155–167.

[41] T. Parasassi, F. Conti, E. Gratton, Time-resolved fluorescence emission spectra of Laurdan in phospholipid vesicles by multifrequency phase and modulation fluorometry, Cell. Mol. Biol. 32 (1986) 103–108.
[42] R.D. Spencer, G. Weber, Influence of Brownian rotations and energy transfer upon the measurements of fluorescence lifetime, J. Chem. Phys. 52 (1970) 1654–1663.
[43] E. Bismuto, G. Irace, G. Colonna, D.M. Jameson, E. Gratton, Dynamic aspects of the heme-binding site in phylogenetically distant myoglobins, Biochim. Biophys. Acta 913 (1987) 150–154.
[44] E. Gratton, M. Limkeman, A continuously variable frequency cross-correlation phase fluorometer with picosecond resolution, Biophys. J. 44 (1983) 315–324.
[45] D.M. Jameson, E. Gratton, Analysis of heterogeneous emissions by multifrequency phase and modulation fluorometry, in: D. Eastwood (Ed.), New Directions in Molecular Luminescence, American Society for Testing and Materials, Philadelphia, 1983, pp. 67–81.
[46] E. Bismuto, D.M. Jameson, E. Gratton, Dipolar relaxations in glycerol: a dynamic fluorescence study of 4-[2′-(dimethylamino)-6′-naphthoyl]cyclohexanecarboxylic acid (DANCA), J. Am. Chem. Soc. 109 (1987) 2354–2357.
[47] G. Weber, F.J. Farris, Synthesis and spectral properties of a hydrophobic fluorescent probe: 6-propionyl-2-(dimethylamino)naphthalene, Biochemistry 18 (1979) 3075–3078.
[48] M. Caffrey, J. Hogan, LIPIDAT: a database of lipid phase transition temperatures and enthalpy changes—DMPC data subset analysis, Chem. Phys. Lipids 61 (1992) 1–109.
[49] T. Parasassi, G. Ravagnan, R.M. Rusch, E. Gratton, Modulation and dynamics of phase properties in phospholipid mixtures detected by Laurdan fluorescence, Photochem. Photobiol. 57 (1993) 403–410.
[50] T. Parasassi, M. Di Stefano, M. Loiero, G. Ravagnan, E. Gratton, Influence of cholesterol on phospholipid bilayers phase domains as detected by Laurdan fluorescence, Biophys. J. 66 (1994) 120–132.
[51] S. Merlo, P. Yager, W. Burgess, An optical method for detecting anesthetics and other lipid soluble compounds, Sens. Actuators A 23 (1990) 1150–1154.
[52] G. Weber, L.B. Young, Fragmentation of bovine serum albumin by pepsin: I. The origin of the acid expansion of the albumin molecule, J. Biol. Chem. 239 (1964) 1415–1423.
[53] L. Stryer, The interaction of a naphthalene dye with apomyoglobin and apohemoglobin: a fluorescent probe of non-polar binding sites, J. Mol. Biol. 13 (1965) 482–495.
[54] A. Gafni, R.P. DeToma, R.E. Manrow, L. Brand, Nanosecond decay studies of a fluorescence probe bound to apomyoglobin, Biophys. J. 17 (1977) 155–168.
[55] H.C. Cheung, I. Gryczynski, H. Malak, W. Wiczk, M.L. Johnson, J.R. Lakowicz, Conformational flexibility of the Cys697–Cys707 segment of myosin subfragment-1: distance distributions by frequency-domain fluorometry, Biophys. Chem. 40 (1991) 1–17.
[56] W.M. Shih, Z. Gryczynski, J.R. Lakowicz, J.A. Spudich, A FRET-based sensor reveals large ATP hydrolysis-induced conformational changes and three distinct states of the molecular motor myosin, Cell 102 (2000) 683–694.
[57] Y.C. Chen, B.Q. Spring, C. Buranachi, B. Tong, G. Malachowski, R.M. Clegg, General concerns of FLIM data representation and analysis, in: A. Perisasamy, R.M. Clegg (Eds.), FLIM Microscopy in Biology and Medicine, Chapman & Hall/CRC, Boca Raton, FL, 2010, pp. 291–339.
[58] Y.C. Chen, R.M. Clegg, Fluorescence lifetime-resolved imaging [review], Photosynth. Res. 102 (2009) 143–155.
[59] N.V. Visser, J.W. Borst, M.A. Hink, A. van Hoek, A.J. Visser, Direct observation of resonance tryptophan-to-chromophore energy transfer in visible fluorescent proteins, Biophys. Chem. 116 (2005) 207–212.

II

Applications of Phasor Plots to in Vitro Protein Studies

James, N.G., Ross, J.A., Štefl, M., Jameson, D.M.
Analytical Biochemistry, 410(1), 70-76, 2011

Analytical Biochemistry 410 (2011) 70–76

Contents lists available at ScienceDirect

Analytical Biochemistry

journal homepage: www.elsevier.com/locate/yabio

Applications of phasor plots to in vitro protein studies

Nicholas G. James [a], Justin A. Ross [a], Martin Štefl [b], David M. Jameson [a,*]

[a] Department of Cell and Molecular Biology, John A. Burns School of Medicine, University of Hawaii, Honolulu, HI 96813, USA
[b] J. Heyrovský Institute of Physical Chemistry, v.v.i., Academy of Sciences of the Czech Republic, Dolejškova 3, Prague 18223, Czech Republic

ARTICLE INFO

Article history:
Received 27 July 2010
Received in revised form 5 November 2010
Accepted 7 November 2010
Available online 13 November 2010

Keywords:
Protein fluorescence
Lifetimes
Kinetics
Protein unfolding
Protein interactions
Ligand binding

ABSTRACT

In a recent article, we described the application of phasor analysis to fluorescence intensity decay data on in vitro samples. As detailed in that article, this method provides researchers with a simple graphical method for viewing lifetime data that can be used to quantify individual components of a mixture as well as to identify excited state reactions. In the current article, we extend the use of in vitro phasor analysis to intrinsic protein fluorescence. We show how alterations in the excited state properties of tryptophan residues are easily visualized using the phasor method. Specifically, we demonstrate that protein–ligand and protein–protein interactions can result in unique shifts in the location of phasor points, indicative of protein conformational changes. Application of the method to a rapid kinetic experiment is also shown. Finally, we show that the unfolding of lysozyme with either urea or guanidine hydrochloride results in different phasor trajectories, indicative of unique denaturation pathways.

Excited state fluorescence lifetime measurements have become a popular and powerful method for gaining information on the local environment of fluorophores in biomolecular systems such as proteins, membranes, and nucleic acids. Excited state intensity decay (lifetime) data are typically obtained using either time domain or frequency domain methods [1,2]. In time domain measurements, the sample is excited with a short pulse of light and the time evolution of the fluorescence intensity decay is recorded, whereas in frequency domain measurements, the sample is typically (but not always) excited with sinusoidally modulated light and the shift in phase and modulation of the emission with respect to the excitation is recorded. Data from each method are essentially equivalent, with the frequency domain data being the Fourier transform of the time domain data [3]. Traditional methods of extracting decay parameters involve fitting the data to models, such as discrete exponentials or distributions [4], until a "good" fit, as judged by the χ^2 value, is reached. A model-less approach, the maximum entropy method, has also been used to describe excited state decay data in terms of the intensity decay components [5]. For a large number of seemingly simple fluorophore systems (e.g., proteins containing a single tryptophan residue), however, the excited state decay cannot be described by single- or even multiexponential models. In some cases, the complexities of the decay may be due to the fact that the fluorophore can sample different molecular environments during the excited state lifetime or to the presence of excited state reactions such as resonance energy transfer, dipolar relaxation, and transient quenching mechanisms.

Tryptophan residues are the most commonly used intrinsic protein probes, and their popularity increased when the method of site-directed mutagenesis allowed the removal or insertion of these residues into specific locations in the protein sequence (although we note that tyrosine fluorescence has also been used in the case of proteins lacking tryptophan residues). The sensitivity of tryptophan's fluorescence properties, including its emission maximum, quantum yield, and lifetime, to local environments in the protein matrix has been used by a number of researchers over the years to characterize a variety of biological processes [2,6–8]. The use of tryptophan analogs, introduced into proteins using molecular biological methods, has also become increasingly popular in studies of protein fluorescence [9,10]. A complete description of all such applications to protein systems is beyond the scope of this article, however, a few examples include the use of tryptophan fluorescence to monitor ligand interactions [11,12], kinetic rate determinations [13,14], and protein–protein, protein–DNA, and protein–RNA interactions [15,16] as well as structural and dynamic features of proteins [17–19] and Förster resonance energy transfer (FRET)[1] [20]. Excited state characterization of tryptophan, free in

* Corresponding author. Address: Department of Cell and Molecular Biology, John A. Burns School of Medicine, University of Hawaii, 651 Ilalo Street, Biosciences 222, Honolulu, HI 96813, USA. Fax: +1 808 692 1968.
E-mail address: djameson@hawaii.edu (D.M. Jameson).

[1] *Abbreviations used:* FRET, Förster resonance energy transfer; NATA, *N*-acetyl-L-tryptophanamide; HSA, human serum albumin; $Na_2S_2O_3$, sodium thiolsulfate; GdHCl, guanidine hydrochloride; PH, pleckstrin homology; GED, GTPase effector region; PRD, proline/arginine-rich domain; hTF, human serum transferrin; hTF N-lobe, recombinant N-lobe of human serum transferrin comprising residues 1–337; FLIM, fluorescence lifetime imaging.

0003-2697/$ - see front matter © 2010 Elsevier Inc. All rights reserved.
doi:10.1016/j.ab.2010.11.011

solution and incorporated into proteins, has revealed the complex decay parameters for this intrinsic probe [21]. The environmental sensitivity of tryptophan's ^1L_A transition [22], the possibility of tryptophan rotamer conformations within the protein matrix [23], and excited state reactions of tryptophan residues with neighboring amino acid side chains [24] all have been suggested to play a role in the nonexponential behavior of tryptophan decay [2].

Analyzing tryptophan lifetimes using the traditional approaches, including fits to discrete exponentials or continuous distributions, does not always allow an adequate description of the decay process or provide meaningful physical interpretation. In addition, many proteins have multiple tryptophan residues and may exhibit energy transfer between these residues, and this frustrates attempts to fit the lifetime data to straightforward models. In many cases, however, the goal is simply to use the intrinsic protein fluorescence to monitor a process such as ligand binding, unfolding, or refolding or to detect a conformational change in a particular region of the protein. In such cases, a less constrained approach may provide a useful tool for monitoring alterations in intrinsic protein decay. The phasor plot offers such an approach, although we note that quantitative information can also be obtained.

We recently explored the application of the phasor approach to in vitro studies and briefly described its general utility in the characterization of heterogeneous emissions and systems demonstrating dipolar relaxation as well as intrinsic protein fluorescence [25]. In the previous article, we discussed the basics of the phasor approach and illustrated its application to heterogeneous mixtures of fluorophores as well as excited state reactions such as dipolar relaxation and FRET. In the current article, we extend these observations to studies of protein conformations. Specifically, we apply the phasor plot approach to a number of protein-related systems, including the effect of pH on tryptophan's lifetime, quenching, and the effect of ligand binding, kinetics, protein–protein interactions, and protein unfolding pathways.

Materials and methods

L-Tryptophan and Mes were obtained from Fluka (St. Louis, MO, USA). *N*-Acetyl-L-tryptophanamide (NATA), fluorescein, human serum albumin (HSA), KI, NaCl, sodium thiolsulfate ($Na_2S_2O_3$), ethanol, Ches, and Hepes were obtained from Sigma (St. Louis, MO, USA). Lysozyme was obtained from Fisher Scientific (Pittsburgh, PA, USA). Thrombin (alpha) and antithrombin III were purchased from Hematologic Technologies (Essex Junction, VT, USA). Sephacryl S-300 resin was obtained from GE Healthcare (Piscataway, NJ, USA). Guanidine hydrochloride (GdHCl) was obtained from Mann Research Laboratories. Urea was purchased from ICN Biomedicals (Irvine, CA, USA). Dynamin 2 was a generous gift from Joseph Albanesi and Barbara Barylko (University of Texas Southwestern Medical School). Recombinant human serum transferrin N-lobe, residues 1–337, was a generous gift from Anne B. Mason (University of Vermont).

HSA purification

Many reports have detailed the fact that even 99% pure lyophilized HSA contains up to 10% higher order oligomers such as dimers, trimers, tetramers, and higher order aggregates formed via disulfides linkage (see, e.g., [26]). To isolate the monomeric protein, HSA (20 mg/ml) was loaded onto a 100-ml Sephacryl S-300 column equilibrated with 20 mM Hepes (pH 7.5). Identification of the oligomeric state and purity of each fraction were determined by nondenaturing native gel electrophoresis (data not shown). The final half of the dominant (monomeric) peak was pooled. HSA concentration was determined using 34,445 M^{-1} cm^{-1} as the molar absorption coefficient at 280 nm [27].

Time-resolved measurements

Phase and modulation data were obtained with an ISS Chronos Fluorometer using either a 280- or 300-nm LED as the light source [28]. The bandpass filter FF01-280/20-25 or FF01-295/15-25 (Semrock, Rochester, NY, USA) was used where appropriate, with the excitation light and the emission collected through a longpass filter (WG315 or WG320, Schott) or a 357/50-nm bandpass filter. Polarizers were set at magic angles to eliminate polarization effects [29]. Reference lifetime standard of NATA at pH 7.5 (2.70 ns at 25 °C and 2.95 ns at 20 °C) was used at an excitation wavelength of 280 or 300 nm [30]. For those experiments in which temperature was varied, glycogen (0.00 ns) was used as a reference. Absorbance values at the exciting wavelengths were kept below 0.05 to avoid inner filter affects.

For measurements involving acrylamide quenching, small aliquots of an 8-M stock solution were added to the sample cuvette to obtain the desired acrylamide concentration. For KI quenching, NaCl was present to maintain the ionic strength between each measurement. The stock solution of KI (3 M) contained a small amount (10^{-4} M) of $Na_2S_2O_3$ to prevent the formation of I_3^-, which absorbs in the excitation region of tryptophan fluorescence.

Phasor plots

The theory underlying the phasor approach is presented in another article [31].

Results and discussion

Tryptophan lifetime/phasor as a function of pH

The sensitivity of tryptophan fluorescence to a number of factors (pH, temperature, and polarity of solvent/environment) makes it ideal to monitor alterations in the protein matrix. Such sensitivity has also made interpretation of fluorescence changes in response to specific biological events difficult at best, highlighting the complexity of this fluorescent probe. We examined the excited state properties of L-tryptophan under changing conditions to illustrate the application of the phasor method for analyzing the heterogeneous lifetime decay of proteins. The phasor plot for L-tryptophan as a function of pH (at 25 MHz) is shown in Fig. 1. As the pH is increased from 6.0 to 11.0, the zwitterion form of tryptophan is converted to the anion form ($pK_a \sim 9.39$), each of these forms has its own unique lifetime and quantum yield [2,32–34]. At pH 9.5, there should be a nearly 1:1 anion-to-zwitterion molecular ratio. However, we should note that the phasor point corresponding to pH 9.5 is not midway between the high and low pH points. The exact distance of the phasor point along the line joining the starting and ending points on the universal circle depends not only on the relative concentration but also on the quantum yields of the species in question (in the case of L-tryptophan, the ratio of the lifetimes and quantum yields of the anion-to-zwitterion forms is ~2.8 [34]). The frequencies used will also weight the fractional contributions of the components differently, that is, lower frequency phasor points will weight the longer lifetime component, whereas higher frequencies will favor the shorter component [35].

Quenching and temperature studies

Quenching of a protein's intrinsic tryptophan fluorescence, with molecules such as I^-, NO_3^-, Cs^-, acrylamide, and molecular oxygen [17–19], is commonly used to probe the dynamics of protein matrices. Chemical quenchers may provide information on the exposure of a tryptophan residue to the solvent as a consequence

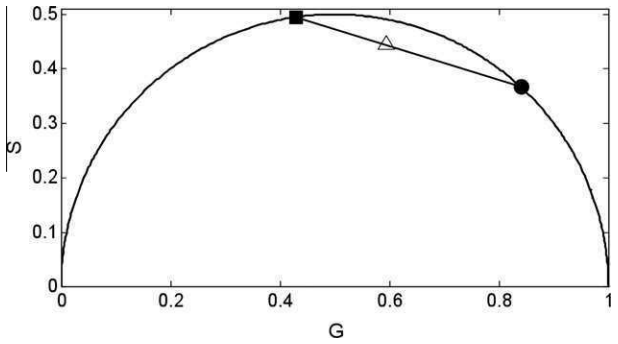

Fig.1. Phasor plot of L-tryptophan at various pH values. The points represent pH 6.0 (circle), pH 9.5 (triangle), and pH 11.0 (square) data at 25 MHz. The lifetime data were collected at 280 nm excitation and 25 °C.

of collision of the excited fluorophore with the quencher molecule (dynamic quenching) or, in some cases, by formation of a ground state dark complex (static quenching) [1]. Both steady state and time-resolved methodologies can be used to obtain quenching information.

As shown in Fig. 2, we examined the effects of quenching molecules on the phasor plot of tryptophan-containing samples. NATA was chosen as a model system because it has a single-exponential decay under our conditions, and the quenching with acrylamide is expected to move the phasor toward shorter lifetimes along the universal circle. The protein lysozyme was used because the photophysics of the tryptophans in this protein have been well investigated [36,37]. Fig. 2 shows the quenching of NATA and lysozyme using the quencher acrylamide. The data were recorded at 89 MHz and 20 °C using a 300-nm LED as the excitation source, and emission was observed through a WG315 longpass filter. As expected, the position of the phasor points is dependent on the quencher concentration. The lifetime of NATA is a single exponential at each quencher concentration and follows a clockwise trajectory along the universal circle toward $G = 1.0$ and $S = 0$ (i.e., 0 ns). With lysozyme, one notes that the phasor points are all within the universal circle, indicating the heterogeneous nature of the lifetime data. The addition of acrylamide results in shorter lifetimes, indicating that one or more of the tryptophan residues in lysozyme are sensitive to dynamic quenching, and the subsequent shift in the phasor points in a clockwise direction. The addition of the quencher iodide (data not shown) also shifted the phasor point, following a similar trajectory to shorter lifetimes, albeit to a lesser extent, as with the acrylamide quenching.

Temperature studies are often used to study protein stability and dynamic aspects of the protein matrix [38]. We examined how temperature affects the phasor points for NATA and lysozyme. As shown in Fig. 3, the phasor points corresponding to NATA as a function of temperature remain on the universal circle and move clockwise as the temperature increases, indicating decreased lifetimes. The phasor points for lysozyme also progress clockwise with increasing temperatures, however, these points begin to migrate more toward the universal circle with increasing temperatures indicating decreases in the lifetime heterogeneity. This correlation of heterogeneity and temperature is similar to what was observed in human superoxide dismutase, which provided support for treatment of tryptophan decay as a continuous lifetime distribution [38]. At 70 °C, a change in trajectory occurs, likely indicating a complete thermal unfolding of the protein and a broadening of the distribution of lifetime values. These results are in agreement with the large volume of thermal denaturation literature on lysozyme [39,40]. Specifically, Morozova and coworkers [41], along with others, reported that the unfolding takes place in two steps, with the first reversible step occurring at approximately 40 °C and a second irreversible step occurring at approximately 70 °C.

Protein–ligand and protein–protein interactions

The sensitivity of tryptophan fluorescence to its environment makes it an ideal probe to monitor local and global structural movements and to provide insights into protein conformational changes associated with ligand binding. Using two protein systems, we investigated how phasor plots (derived from the intrinsic protein fluorescence) change during interactions with different ligands. Dynamin 2 is a 100-kDa GTPase associated with the pinching off of the plasma membrane during vesicle fission [42]. Dynamin 2 is composed of five domains—an N-terminal GTPase domain, a middle domain, a pleckstrin homology (PH) domain, a GTPase effector region (GED), and a proline/arginine-rich domain (PRD)—and contains five tryptophan residues, four of which are in the PH domain and one of which is in the C-terminal PRD. Previous work from our lab has shown that the tryptophans in dynamin can transfer energy to a fluorescent nucleotide [43,44]. In Fig. 4A, the phasor points of dynamin alone, GDP-bound dynamin, and GTPγS (a slowly hydrolyzable GTP analogue)-bound dynamin are presented. The data shown were collected with 300 nm excitation at 84 MHz and 20 °C. The addition of the guanine nucleotides clearly causes the phasor point to shift, and the position of the phasor point depends on the precise nucleotide used. These results indicate that there is a conformational change around one or more tryptophan residues associated with guanine nucleotide binding, moreover, the GDP and GTPγS ligands elicit different responses, indicating that the conformation of the protein matrix is not identical in the two cases. Solomaha and Palfrey [45], using steady state tryptophan fluorescence and limited proteolysis, concluded that

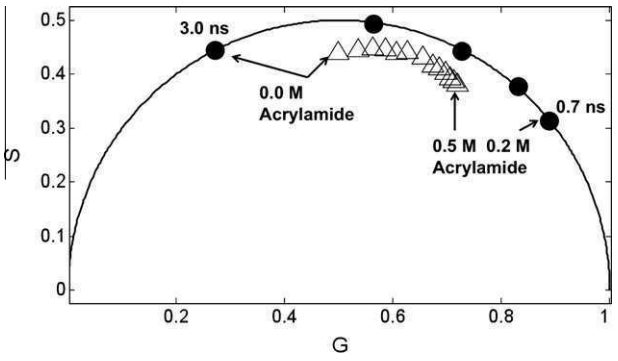

Fig.2. NATA (circles) and lysozyme (triangles) phasor points at 89 MHz, at 300 nm excitation and 20 °C, with the addition of various concentrations of acrylamide (0–0.2 M with NATA and 0–0.5 M with lysozyme).

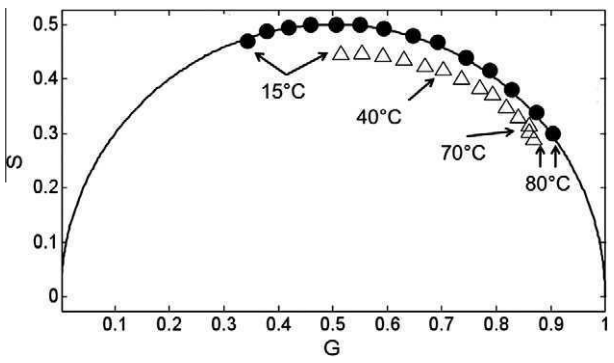

Fig.3. Phasor plot, at 70 MHz and 280 nm excitation, of NATA (circles) and lysozyme (triangles) as a function of increasing temperatures.

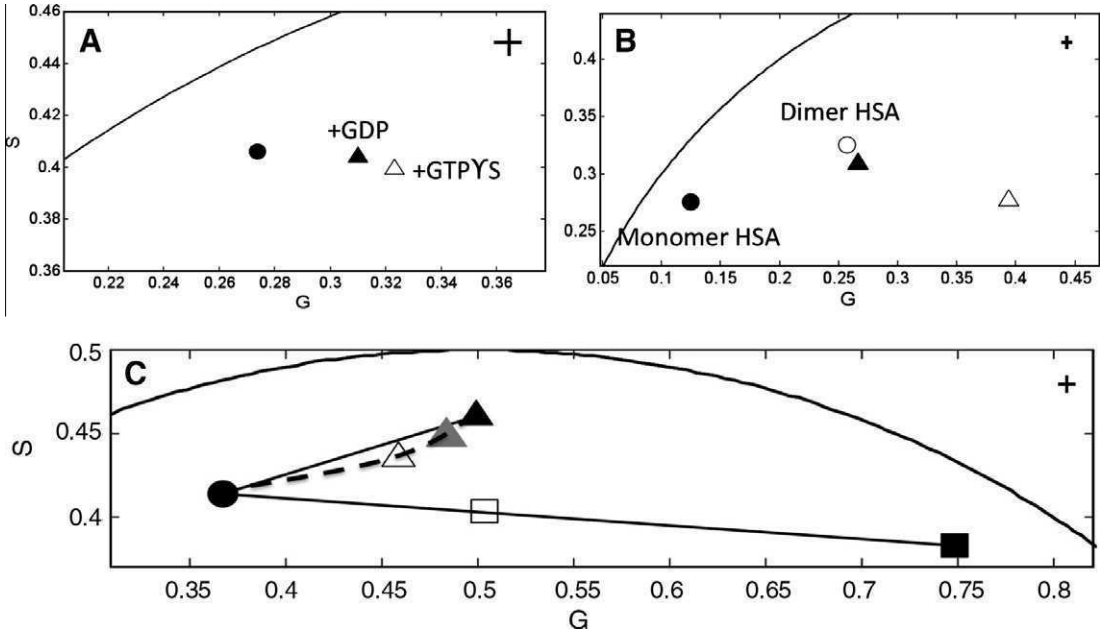

Fig.4. (A) Phasor plot for dynamin 2 alone (circle), GDP-bound dynamin (closed triangle), and GTPγS-bound dynamin (open triangle). (B) Monomeric HSA (closed circle) plotted with furosemide-bound HSA (open triangle) and D-thyroxine-bound HSA (closed triangle). Dimeric HSA (open circle), which can be found up to 10% in lyophilized HSA, has a unique decay/phasor point compared with monomeric HSA. (C) Phasor plot showing point movements due to protein–protein interaction. Solid lines between antithrombin (circle), lysozyme (closed square), and thrombin (closed triangle) are the projected linear movement of the phasor point for noninteracting species. Mixtures of antithrombin/lysozyme (both at 1 μM, open square) and antithrombin/thrombin (gray triangle 0.5:1;open triangle 1:1) are shown on the plot. The dashed line represents the projected phasor movement for increasing concentrations of antithrombin in the presence of thrombin. Crosshairs seen in the upper part of each figure represent the statistical error for each phasor point under the expanded phasor plot scale.

although GDP and GTP bind with similar affinities (13.0 and 7.1 μM, respectively), they produce distinct structural changes, in agreement with our phasor plot data.

HSA, which contains a single tryptophan residue (Trp214), has been the subject of numerous fluorescence studies, including time-resolved studies (see, e.g., [33,46–51]). HSA is commonly targeted for drug uptake studies, and often these drug interactions are studied via changes in tryptophan fluorescence. In Fig. 4B, we show the phasor point, collected using 300 nm excitation at 84 MHz and 25 °C, of the intrinsic fluorescence from monomeric HSA. In the presence of furosemide or D-thyroxine, two drugs known to bind to HSA and to quench the tryptophan fluorescence [11,52], the phasor point shifts clockwise, indicating a shortening of the average lifetime. These shifts in the phasor point indicate that drug binding induces changes in the protein matrix near the tryptophan residue and also that the conformational state of the protein differs depending on the nature of the drug, likely due to different binding sites (thyroxine has been shown to have multiple sites) on HSA. We also note that the phasor point corresponding to dimeric HSA, isolated from the monomeric protein using size exclusion chromatography, differs from the monomeric phasor point (seen in Fig. 4B). Hazan and coworkers [47] also showed that monomeric and dimeric HSA have different excited state lifetime properties. This difference underscores the necessity of isolating monomeric HSA from the aggregates usually found in commercial lyophilized preparations before undertaking a study of its intrinsic tryptophan fluorescence, an obvious step that, surprisingly, is sometimes overlooked.

One may also expect, from the previous sets of experiments, that protein–protein interactions could also be investigated using intrinsic tryptophan fluorescence and phasor plot analysis. For two interacting proteins with distinct average lifetimes, complex formation may be expected to change one or both protein conformations and result in a phasor point that deviates from the "normal" linear combination typically seen for noninteracting mixtures [53]. Fig. 4C shows a set of data (acquired with 280 nm excitation at 43 MHz and 20 °C) for thrombin, antithrombin, lysozyme, and mixtures therein. Antithrombin and lysozyme are not predicted to interact, therefore a solution containing the two proteins should produce a phasor point that falls directly on a line between their individual points. This outcome is clearly observed (Fig. 4C) for the phasor plot of a 1:1 (at 1 μM) mixture of the two proteins. On the other hand, thrombin/antithrombin is known to form a tight complex [54] and may be expected to produce a distinct phasor point away from the linear combination. The phasor point of the thrombin/antithrombin (1:1 at 1 μM for each protein) indeed shifts inward away from the line connecting the points corresponding to the two pure proteins, indicating a change in intrinsic fluorescence on protein interaction. This demonstration shows how phasor plots can provide a facile indication of protein interaction.

Kinetics of protein–ligand binding/dissociation

Determination of the rate constants associated with protein–ligand binding/dissociation reactions is a major goal in many studies. Kinetics of such reactions often proceed on a rapid time scale (seconds to a few minutes). Steady state fluorescence methodologies, such as stopped-flow fluorescence, are frequently preferred over lifetime methods because traditional frequency domain lifetime measurements usually require 1 or 2 min for reasonable precision (although specialized fast scanning methods are available) [55,56]. However, the phasor plot method, recorded at a single frequency, is well-suited for rapidly tracking changes in the phase and modulation data. To illustrate this point and validate the phasor method for tracking kinetics of protein–ligand dissociation, the phase and modulation of the intrinsic fluorescence of human serum transferrin (the isolated N-lobe) were recorded over approximately 300 s at 80 MHz in pH 6.0 buffer and the presence of a chelator. Human serum transferrin (hTF) is a bilobal glycoprotein

that serves as the major transporter of iron in humans (reviewed in [57]). Both lobes, termed the N- and C-lobes, coordinate ferric iron via four amino acid ligands and a synergistic carbonate anion. Numerous studies on hTF have shown that binding of iron quenches the intrinsic tryptophan fluorescence through radiative and nonradiative means [14,58,59]. Thus, rate constants for iron removal are determined by tracking the enhancement in fluorescence emission over time under endosomal-like conditions (~pH 5.5, ~150–200 mM salt, and the presence of a chelator), and this takes place within seconds to minutes.

The lifetime of iron-bound and apo hTF N-lobe (which contains three tryptophan residues) was determined previously [58]. The two discrete lifetime values associated with the hTF N-lobe (~1.4 and ~4.1 ns) undergo minimal change (±0.3 ns) during iron removal. The fractional fluorescence of each lifetime component, however, undergoes large changes (0.66/0.28 for iron-bound and 0.20/0.79 for apo). Based on the theoretical description (see previous article), the decay during iron release would be predicted to be a line between the iron-bound and apo phasor points. Fig. 5, which shows the phasor plot (taken at 80 MHz and 300 nm excitation) during iron release (black line) and the points for iron-bound (circle) and apo (triangle), clearly demonstrates the predicted linear progression in the phasor point during iron release from the iron-bound point toward the apo phasor point. Sample heterogeneity, which was expected based on the fitting to a discrete exponential model, is seen in the phasor vectors of hTF N-lobe given that each point is inside the universal circle. Calculation of the distance at each point over time can provide information regarding excited state changes during iron removal (i.e., one can recover the fractional contribution of each emitting state using standard linear methods). Interestingly, the phasor data during iron release indicate that the change in the excited state properties of the hTF N-lobe occurs in two modes: a faster initial mode (during the first ~90 s) followed by a slower progression toward apo (~90–300 s). These results are similar to those observed following the steady state emission changes, in which the faster rate was conclusively determined to be iron release and the slower rate was assigned to conformational events [14]. Data can be acquired on a subsecond time scale with the use of a stopped-flow attachment, however, such an attachment was not available to us to directly demonstrate more rapid measurements. This kinetic run demonstrates how the phasor method can be used for tracking excited state changes during protein–ligand dissociation, which can complement data obtained using other methods. We also point out that the phasor approach was applied in fluorescence lifetime imaging (FLIM) by Redford and Clegg [53] to follow the kinetics of mixing in turbulent flow at the microsecond time scale.

Protein unfolding/folding pathways

Protein folding has been intensely investigated, both theoretically and experimentally, for many decades. One of the most popular experimental approaches to protein folding involves examination of the unfolding pathway(s) by means of chemical denaturation [60,61]. Chaotropic agents, such as GdHCl and urea, are commonly used denaturants. Unfolding experiments using such chemical denaturants have one major underlying assumption—that the overall thermodynamic unfolding of the protein is independent of denaturing agent, although the structural changes associated with the change are dependent [62,63]. The molecular mechanisms for protein unfolding by GdHCl and urea are still unclear, even though mechanisms were proposed as early as 1936 [64]. Models describing the direct interaction of the denaturant with the protein and disruption of the hydrophobic interactions via disruption of the hydrogen bonding network are the commonly accepted mechanisms [65,66]. Recently, Almarza and coworkers [67] proposed a more detailed model for urea-induced protein unfolding in which urea molecules interact with protonated histidines followed by hydrogen bond formation with polar residues, leading to hydrophobic collapse of the protein.

Because the detailed molecular mechanisms for protein unfolding due to GdHCl and urea are likely different, it would stand to reason that the intrinsic fluorescence properties will be different during denaturation depending on which chaotropic agent is present. Tryptophan fluorescence is sensitive to changes in the local environment, and if the structural changes leading to unfolding of the protein are intrinsically different, then the environment around the tryptophan residues could differ depending on the chaotropic agent, resulting in distinct fluorescence properties. The phasor plot of lysozyme with increasing concentrations of GdHCl (0–6 M) and urea (0–8 M) is shown in Fig. 6. Initial additions of either denaturant cause similar changes, yet by 2 M the trajectories of the phasor points diverge, with GdHCl shifting the phasor points in a counterclockwise direction. The final points between GdHCl and urea are dramatically different, indicating unique unfolded forms. Similar deviations between unfolding with GdHCl and urea were observed with monomeric HSA (data not shown). It is clear that the phasor plot method has the potential for illustrating different unfolding pathways given that both proteins tested showed significant deviations in phasor point trajectories depending on the denaturant.

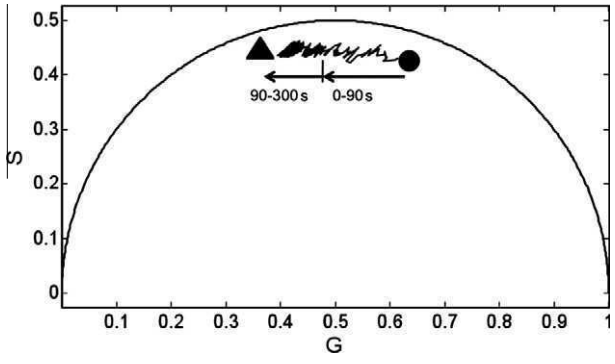

Fig.5. Phasor plot of iron release from hTF N-lobe. Iron-bound and apo phasor vectors are drawn as circle and triangle, respectively. The change in phasor during iron removal, at pH 6.0 with 4 mM ethylenediaminetetraacetic acid (EDTA) over 300 s, is drawn as a black line. Over the first ~ 90 s, there is a rapid change in the excited state data followed by a much slower change. Data shown were collected at 80 MHz and 25 °C.

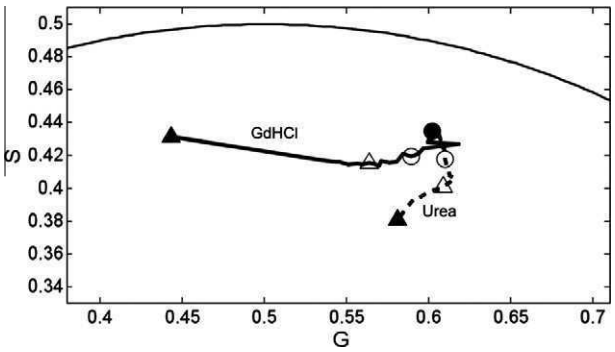

Fig.6. Phasor point trajectory of lysozyme denaturation as a function of increasing GdHCl (solid line) and urea (dashed line) concentrations. Concentrations of 0 M (closed circle), 1 M (open circle), 2 M (open triangle), and 6/8 M (closed triangle) GdHCl and urea are highlighted. Data were recorded at 280 nm, and data plotted were at 70 MHz and 25 °C.

Conclusions

In this article, we have described the application of the phasor method to time-resolved studies on intrinsic protein fluorescence. Using this approach, the complex decay of protein fluorescence, due to either multiple emitting tryptophan residues or excited state reactions such as tyrosine-to-tryptophan energy transfer, can be reduced to a single point on a phasor plot. Activities such as ligand or protein binding and protein denaturation, which result in changes in the microenvironment of the tryptophan residue(s), lead to movements of the phasor point. The trajectory of the phasor point in response to a physical or chemical perturbation can be followed to provide insights into the processes under investigation.

Acknowledgments

This work was supported in part by Allergan and by the National Institutes of Health (RO1GM076665). M. Štefl was supported by the Ministry of Education of the Czech Republic via grant LC06063 and by Charles University in Prague via Fond Mobility. We thank Joseph Albanesi and Barbara Barylko for supplying the dynamin 2. We also thank Anne B. Mason for supplying the iron-bound human serum transferrin N-lobe.

References

[1] B. Valeur, Molecular Fluorescence, Wiley–VCH, Weiheim;Germany, 2002.
[2] J.A. Ross, D.M. Jameson, Time-resolved methods in biophysics: 8. Frequency domain fluorometry – applications to intrinsic protein fluorescence, Photochem. Photobiol. Sci. 7 (2008) 1301–1312.
[3] G. Weber, Resolution of the fluorescence lifetimes in a heterogeneous system by phase and modulation measurements, J. Phys. Chem. 85 (1981) 949–953.
[4] J.R. Alcala, E. Gratton, F.G. Prendergast, Interpretation of fluorescence decays in proteins using continuous lifetime distributions, Biophys. J. 51 (1987) 925–936.
[5] J.C. Brochon, Maximum entropy method of data analysis in time-resolved spectroscopy, Methods Enzymol. 240 (1994) 262–311.
[6] J.M. Beechem, L. Brand, Time-resolved fluorescence of proteins, Annu. Rev. Biochem. 54 (1985) 43–71.
[7] C.N. Bialik, B. Wolf, E.L. Rachofsky, J.B. Ross, W.R. Laws, Dynamics of biomolecules: assignment of local motions by fluorescence anisotropy decay, Biophys. J. 75 (1998) 2564–2573.
[8] J.T. Vivian, P.R. Callis, Mechanisms of tryptophan fluorescence shifts in proteins, Biophys. J. 80 (2001) 2093–2109.
[9] J.B. Ross, A.G. Szabo, C.W. Hogue, Enhancement of protein spectra with tryptophan analogs: fluorescence spectroscopy of protein–protein and protein–nucleic acid interactions, Methods Enzymol. 278 (1997) 151–190.
[10] N.G. James, S.L. Byrne, A.B. Mason, Incorporation of 5-hydroxytryptophan into transferrin and its receptor allows assignment of the pH induced changes in intrinsic fluorescence when iron is released, Biochim. Biophys. Acta 1794 (2009) 532–540.
[11] J.R. Voelker, D.M. Jameson, D.C. Brater, In vitro evidence that urine composition affects the fraction of active furosemide in the nephrotic syndrome, J. Pharmacol. Exp. Ther. 250 (1989) 772–778.
[12] Z. Akyol, J.A. Bartos, M.A. Merrill, L.A. Faga, O.R. Jaren, M.A. Shea, J.W. Hell, Apo-calmodulin binds with its C-terminal domain to the *N*-methyl-D-aspartate receptor NR1 C0 region, J. Biol. Chem. 279 (2004) 2166–2175.
[13] C.A. Dunlap, M.D. Tsai, Use of 2-aminopurine and tryptophan fluorescence as probes in kinetic analyses of DNA polymerase beta, Biochemistry 41 (2002) 11226–11235.
[14] N.G. James, C.L. Berger, S.L. Byrne, V.C. Smith, R.T. MacGillivray, A.B. Mason, Intrinsic fluorescence reports a global conformational change in the N-lobe of human serum transferrin following iron release, Biochemistry 46 (2007) 10603–10611.
[15] D.M. Jameson, E. Gratton, J.F. Eccleston, Intrinsic fluorescence of elongation factor Tu in its complexes with GDP and elongation factor Ts, Biochemistry 26 (1987) 3894–3901.
[16] V.V. Bulygin, Y.M. Milgrom, Studies of nucleotide binding to the catalytic sites of *Escherichia coli* βY331W–F1-ATPase using fluorescence quenching, Proc. Natl. Acad. Sci. USA 104 (2007) 4327–4331.
[17] S.S. Lehrer, Solute perturbation of protein fluorescence. The quenching of the tryptophyl fluorescence of model compounds and of lysozyme by iodide ion, Biochemistry 10 (1971) 3254–3263.
[18] M.R. Eftink, C.A. Ghiron, Dynamics of a protein matrix revealed by fluorescence quenching, Proc. Natl. Acad. Sci. USA 72 (1975) 3290–3294.
[19] J.R. Lakowicz, G. Weber, Quenching of fluorescence by oxygen: a probe for structural fluctuations in macromolecules, Biochemistry 12 (1973) 4161–4170.
[20] J.R. Unruh, K. Kuczera, C.K. Johnson, Conformational heterogeneity of a leucine enkephalin analogue in aqueous solution and sodium dodecyl sulfate micelles: comparison of time-resolved FRET and molecular dynamics simulations, J. Phys. Chem. B 113 (2009) 14381–14392.
[21] D.M. Rayner, A.G. Szabo, Time resolved fluorescence of aqueous tryptophan, Can. J. Chem. 56 (1978) 743–745.
[22] P.R. Callis, ^1L_a and ^1L_b transitions of tryptophan: applications of theory and experimental observations to fluorescence of proteins, Methods Enzymol. 278 (1997) 113–150.
[23] A.H. Clayton, W.H. Sawyer, Tryptophan rotamer distributions in amphipathic peptides at a lipid surface, Biophys. J. 76 (1999) 3235–3242.
[24] Y. Chen, M.D. Barkley, Toward understanding tryptophan fluorescence in proteins, Biochemistry 37 (1998) 9976–9982.
[25] N.G. James, M. Stefl, J.A. Ross, D.M. Jameson, Application of phasor plots to analysis of fluorophore heterogeneity;excited state reactions;and protein conformations, Biophys. J. 98 (2010) 750a.
[26] H.R. Costantino, L. Shieh, A.M. Klibanov, R. Langer, Heterogeneity of serum albumin samples with respect to solid-state aggregation via thiol–disulfide interchange: implications for sustained release from polymers, J. Control. Release 44 (1997) 255–261.
[27] C.N. Pace, F. Vajdos, L. Fee, G. Grimsley, T. Gray, How to measure and predict the molar absorption coefficient of a protein, Protein Sci. 4 (1995) 2411–2423.
[28] B. Barbieri, E. Terpetschnig, D.M. Jameson, Frequency-domain fluorescence spectroscopy using 280-nm and 300-nm light-emitting diodes: measurement of proteins and protein-related fluorophores, Anal. Biochem. 344 (2005) 298–300.
[29] R.D. Spencer, G. Weber, Influence of Brownian rotations and energy transfer upon the measurements of fluorescence lifetime, J. Chem. Phys. 52 (1970) 1654–1663.
[30] N. Boens, W. Qin, N. Basaric, J. Hofkens, M. Ameloot, J. Pouget, J.P. Lefevre, B. Valeur, E. Gratton, M. Van De Ven, N.D. Silva Jr., Y. Engelborghs, K. Willaert, A. Sillen, G. Rumbles, D. Phillips, A.J. Visser, A. van Hoek, J.R. Lakowicz, H. Malak, I. Gryczynski, A.G. Szabo, D.T. Krajcarski, N. Tamai, A. Miura, Fluorescence lifetime standards for time and frequency domain fluorescence spectroscopy, Anal. Chem. 79 (2007) 2137–2149.
[31] M. Štefl, N.G. James, J.A. Ross, D.M. Jameson, Applications of phasors to in vitro time-resolved fluorescence measurements, Anal. Biochem. (2010), doi:10.1016/j.ab.2010.11.010.
[32] A. White, Effect of pH on fluorescence of tryosine, tryptophan, and related compounds, Biochem. J. 71 (1959) 217–220.
[33] W.B. De Lauder, P. Wahl, PH dependence of the fluorescence decay of tryptophan, Biochemistry 9 (1970) 2750–2754.
[34] D.M. Jameson, G. Weber, Resolution of the pH-dependent heterogeneous fluorescence decay of tryptophan by phase and modulation measurements, J. Phys. Chem. 85 (1981) 953–958.
[35] R.D. Spencer, G. Weber, Measurement of subnanosecond fluorescence lifetimes with a cross-correlation phase fluorometer, Annu. NY Acad. Sci. 158 (1969) 361–376.
[36] T. Imoto, L.S. Forster, J.A. Rupley, F. Tanaka, Fluorescence of lysozyme: emissions from tryptophan residues 62 and 108 and energy migration, Proc. Natl. Acad. Sci. USA 69 (1972) 1151–1155.
[37] S.S. Lehrer, G.D. Fasman, Fluorescence of lysozyme and lysozyme substrate complexes: separation of tryptophan contributions by fluorescence difference methods, J. Biol. Chem. 242 (1967) 4644–4651.
[38] N. Rosato, E. Gratton, G. Mei, A. Finazzi-Agro, Fluorescence lifetime distributions in human superoxide dismutase. Effect of temperature and denaturation, Biophys. J. 58 (1990) 817–822.
[39] S. Segawa, M. Nakayama, M. Sakane, Rates of structural fluctuations of lysozyme in the range of thermal unfolding transition, Biopolymers 20 (1981) 1691–1705.
[40] J. Jacob, C. Krafft, K. Welfle, H. Welfle, W. Saenger, Melting points of lysozyme and ribonuclease A crystals correlated with protein unfolding: a Raman spectroscopic study, Acta Crystallogr. D 54 (1998) 74–80.
[41] L. Morozova, P. Haezebrouck, F. Van Cauwelaert, Stability of equine lysozyme: I. Thermal unfolding behaviour, Biophys. Chem. 41 (1991) 185–191.
[42] S.D. Conner, S.L. Schmid, Regulated portals of entry into the cell, Nature 422 (2003) 37–44.
[43] D.D. Binns, M.K. Helms, B. Barylko, C.T. Davis, D.M. Jameson, J.P. Albanesi, J.F. Eccleston, The mechanism of GTP hydrolysis by dynamin II: a transient kinetic study, Biochemistry 39 (2000) 7188–7196.
[44] J.F. Eccleston, D.D. Binns, C.T. Davis, J.P. Albanesi, D.M. Jameson, Oligomerization and kinetic mechanism of the dynamin GTPase, Eur. Biophys. J. 31 (2002) 275–282.
[45] E. Solomaha, H.C. Palfrey, Conformational changes in dynamin on GTP binding and oligomerization reported by intrinsic and extrinsic fluorescence, Biochem. J. 391 (2005) 601–611.
[46] S. Kasai, T. Horie, T. Mizuma, S. Awazu, Fluorescence energy transfer study of the relationship between the lone tryptophan residue and drug binding sites in human serum albumin, J. Pharm. Sci. 76 (1987) 387–392.
[47] G. Hazan, E. Haas, I.Z. Steinberg, The fluorescence decay of human serum albumin and its subfractions, Biochim. Biophys. Acta 434 (1976) 144–153.
[48] P. Marzola, E. Gratton, Hydration and protein dynamics: frequency domain fluorescence spectroscopy of proteins in reverse micelles, J. Phys. Chem. 95 (1991) 9488–9495.
[49] J.R. Lakowicz, I. Gryczynski, Tryptophan fluorescence intensity and anisotropy decays of human serum albumin resulting from one-photon and two-photon excitation, Biophys. Chem. 45 (1992) 1–6.

[50] D.M. Davis, D. McLoskey, D.J. Birch, P.R. Gellert, R.S. Kittlety, R.M. Swart, The fluorescence and circular dichroism of proteins in reverse micelles: application to the photophysics of human serum albumin and *N*-acetyl-L-tryptophanamide, Biophys. Chem. 60 (1996) 63–77.
[51] M.K. Helms, C.E. Petersen, N.V. Bhagavan, D.M. Jameson, Time-resolved fluorescence studies on site-directed mutants of human serum albumin, FEBS Lett. 408 (1997) 67–70.
[52] C.E. Petersen, C.E. Ha, D.M. Jameson, N.V. Bhagavan, Mutations in a specific human serum albumin thyroxine binding site define the structural basis of familial dysalbuminemic hyperthyroxinemia, J. Biol. Chem. 271 (1996) 19110–19117.
[53] G.I. Redford, R.M. Clegg, Polar plot for frequency-domain analysis of fluorescence lifetimes, J. Fluoresc. 15 (2005) 805–815.
[54] D. Beeler, R. Rosenberg, R. Jordan, Fractionation of low molecular weight heparin species and their interaction with antithrombin, J. Biol. Chem. 254 (1979) 2902–2913.
[55] O. Bilsel, L. Yang, J.A. Zitzewitz, J.M. Beechem, C.R. Matthews, Time-resolved fluorescence anisotropy study of the refolding reaction of the α-subunit of tryptophan synthase reveals nonmonotonic behavior of the rotational correlation time, Biochemistry 38 (1999) 4177–4187.
[56] B.A. Feddersen, D.W. Piston, E. Gratton, Digital parallel acquisition in frequency domain fluorimetry, Rev. Sci. Instrum. 60 (1989) 2929–2936.
[57] A.B. Mason, S.J. Everse, Iron transport by transferrin, in: H. Fuchs (Ed.), Iron Metabolism and Disease, Research Signpost, Kerala, India, 2008, pp. 83–123.
[58] N.G. James, J.A. Ross, A.B. Mason, D.M. Jameson, Excited-state lifetime studies of the three tryptophan residues in the N-lobe of human serumn transferrin, Protein Sci. (2010) 99–110.
[59] S.S. Lehrer, Fluorescence and absorption studies of the binding of copper and iron to transferrin, J. Biol. Chem. 244 (1969) 3613–3617.
[60] K.A. Dill, S.B. Ozkan, M.S. Shell, T.R. Weikl, The protein folding problem, Annu. Rev. Biophys. 37 (2008) 289–316.
[61] A.R. Fersht, From the first protein structures to our current knowledge of protein folding: delights and scepticisms, Nat. Rev. Mol. Cell Biol. 9 (2008) 650–654.
[62] W. Pfeil, P.L. Privalov, Thermodynamic investigations of proteins: II. Calorimetric study of lysozyme denaturation by guanidine hydrochloride, Biophys. Chem. 4 (1976) 33–40.
[63] G.I. Makhatadze, P.L. Privalov, Protein interactions with urea and guanidinium chloride: a calorimetric study, J. Mol. Biol. 226 (1992) 491–505.
[64] A.E. Mirsky, L. Pauling, On the structure of native;denatured;and coagulated proteins, Proc. Natl. Acad. Sci. USA 22 (1936) 439–447.
[65] R.B. Simpson, W. Kauzmann, The kinetics of protein denaturation: I. The behavior of the optical rotation of ovalbumin in urea solutions, J. Am. Chem. Soc. 75 (1953) 5139–5152.
[66] M. Roseman, W.P. Jencks, Interactions of urea and other polar compounds in water, J. Am. Chem. Soc. 97 (1975) 631–640.
[67] J. Almarza, L. Rincon, A. Bahsas, F. Brito, Molecular mechanism for the denaturation of proteins by urea, Biochemistry 48 (2009) 7608–7613.

III

Limitations of Electronic Energy Transfer in the Determination of Lipid Nanodomain Sizes

Šachl, R., Humpolíčková, J., Štefl, M., Johansson, L.B. -A., Hof, M.
Biophysical Journal, 101(11), L60-L62, 2011

Limitations of Electronic Energy Transfer in the Determination of Lipid Nanodomain Sizes

Radek Šachl,[†‡] Jana Humpolíčková,[†] Martin Štefl,[†] Lennart B.-Å. Johansson,[‡] and Martin Hof[†*]
[†]J. Heyrovský Institute of Physical Chemistry, v.v.i., Academy of Sciences of the Czech Republic, Prague, Czech Republic; and [‡]Department of Chemistry: Biophysical Chemistry, Umeå University, Umeå, Sweden

ABSTRACT Even though superresolution microscopy indicates that size of plasma membrane rafts is <20 nm, those structures have never been observed. Förster resonance energy transfer (FRET) is therefore still the most powerful optical method for characterization of such domains. In this letter we investigate relation between nanodomain affinity of a donor-acceptor (D/A) pair and the detectable nanodomain size/area. We show that probes with high affinity to the liquid-ordered (L_o) phase are required for detecting domain sizes of a few nanometers, and/or domains that occupy a few percent of the bilayer area. A combination of donors and acceptors that prefer different phases is the more favorable approach. For instance, a D/A pair with the distribution constant of donors $K_D = 5$ and acceptors $K_A = 0.01$ can resolve a broad spectrum of nanodomain sizes. On the other hand, currently available donors and acceptors that prefer the same phase, either the liquid-disordered (L_d) or L_o phase, are not so convenient for determining domain sizes <20 nm. Here the detection limits of FRET experiments employing several commonly used D/A pairs have been investigated.

Received for publication 12 September 2011 and in final form 3 November 2011.

*Correspondence: martin.hof@jh-inst.cas.cz

INTRODUCTION

Despite the advances in far-field optical microscopy, subwavelength lipid domains have never been directly visualized, but their size was predicted to be <20 nm (1). Förster resonance energy transfer (FRET) is therefore often employed in characterization of these domains (2,3), also due to the fact that FRET can report on nanodomains even if they are formed transiently. The size determination of these nanodomains by FRET requires knowledge about partitioning of donors (D) and acceptors (A) between nanodomains and the remaining liquid-disordered (L_d) bilayer. Unfortunately, there is a lack of probes exhibiting substantial affinity to the liquid-ordered (L_o) phase, which would be ideal for studies on the nanometer scale. Hitherto, labeled cholera toxin shows the highest affinity (4). Yet, cholera toxin is a less favorable reporter, because it triggers the phase separation (2). The presence of other L_o preferring probes, such as perylene or NBD-DPPC, is assumed to have less impact on the phase composition, although K is considerably lower. Assuming realistic distribution coefficients, this work explores the theoretical limits for the FRET nanodomain size determination. Apart from that, the validity of FRET experiments using common D/A pairs (2,3,5) is discussed.

MONTE CARLO SETUP

For the Monte Carlo setup ((6) and see the Supporting Material), the distribution of donors and acceptors between the domains and the remaining bilayer is described by the distribution constant K_i ($= [i]_{Lo}/[i]_{Ld}$, i = A or D). The donors were uniformly distributed in the interior of the lipid bilayer, whereas the acceptors resided at the lipid-water interface. As shown in the Supporting Material, the z position of the donors has a minor influence on the generated curves. The D/A to lipid ratio was 1:200. The outcome of the simulation is a fluorescence decay of donors quenched by acceptors in bilayers containing circular nanodomains. This decay was compared with the decay that corresponds to a uniform distribution of donors and acceptors in the bilayer, i.e., to the case when the bilayer did not contain any domains but had composition similar to that when domains were present. The FRET experiments can also be carried out in the steady-state mode, whereby one compares the steady-state intensities obtained for nonuniform (F) and uniform (F_{uni}) distributions of D/A. This intensity is obtained from the simulations by integrating the decay.

THEORETICAL LIMITS OF FRET FOR NANODOMAIN DETECTION

Intrinsically, the resolution of FRET experiments in the determination of domain size depends on the affinity of D/A pairs to the L_o and L_d phases. Three distinct cases have been considered: I), D/A pairs reside inside L_o nanodomains. II), D/A pairs are excluded from said nanodomains. III), donors and acceptors exhibit an increased affinity to the different phases. Cases I and II provide faster decays as compared to uniform D/A distributions, whereas the FRET efficiency is decreased in Case III. According to our experience, any changes in the steady-state intensity ratio $F/F_{uni} < 1.15$ can hardly be

Editor: Petra Schwille.

doi: 10.1016/j.bpj.2011.11.001

interpreted as a reproducible change. Colors used in Figs. 1–3 have the following meaning (compare to Fig. 1): red, domains are clearly beyond the resolution of time-resolved (TR) FRET, i.e., decays for the uniform (UD) and nonuniform (ND) distribution of probes coincide with each other and $F/F_{uni} < 1.05$; orange, domains are close to the detection limit for TR FRET, i.e., decays for the UD and ND are poorly separated (by eye) and $1.05 < F/F_{uni} < 1.1$; yellow, domains are detectable by FRET and are close to the detection limit by the steady-state intensity of donors, i.e., decays for the UD and ND are well separated and $1.1 < F/F_{uni} < 1.2$; green, domains are resolved by both approaches, i.e., $F/F_{uni} > 1.2$.

Case I considers probes that show an increased affinity to the L_o phase. The favorable green region is reached if both K_D and $K_A > 10$ (compare to Fig. 2 and see the Supporting Material). Unfortunately, such probes are not yet available. For more realistic values of K_D and $K_A = 3$ (compare to Fig. 2), domains with an area exceeding 20% and radii $> 1.6\ R_0$ (R_0 denotes the Förster radius) might be resolved by TR FRET (*green* region), whereas for $K_D = 5$ and $K_A = 5$ (i.e., comparable to labeled cholera toxin), domains with an area >15% and radii $>1\ R_0$ can be detected by TR FRET (*yellow-green* region). The fluorescence lifetime of probes might depend on the lipid phase composition. Suppose that the donor lifetime is longer in the L_o phase (8 ns) and shorter in the L_d phase (6 ns), which has been obtained for perylene (compare to the Supporting Material). Then the decay rate of donors becomes longer due to longer lifetime of donors emitting from the domains, and simultaneously shorter due to increased FRET in the same phase. This contraproductive behavior implies that $K_D = 5$ and $K_A = 5$ would not still be high enough to visualize the domains (compare to Fig. 2, *right*). Even for $K_D = K_A = 10$, domains with an area <10% and radii $<1\ R_0$ still belong in the red-orange region. Thus, even when using the data from Hammond et al. (2) and Chiantia et al. (4) with the favorable combination of perylene as donor and labeled cholera toxin as acceptor, Case I is not a realistic approach for determining domain sizes <20 nm.

Case II appears to be most common, as is evident from the K values of membrane labels used. The design of experiments

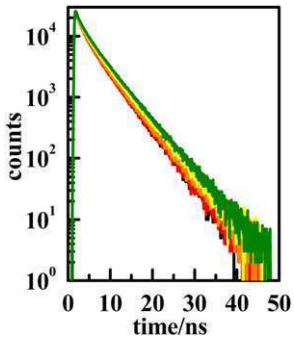

FIGURE 1 Decays generated for the uniform distribution of D/A (*black*), and those corresponding to the red, orange, yellow, and green regions. $R = 10$ nm, area varied between 4 and 34%.

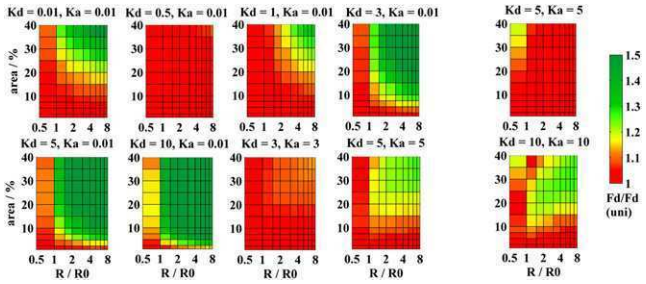

FIGURE 2 Resolution of FRET represented by the ratio of the intensity of donors (F_D) to the intensity of donors when D/A pairs are distributed uniformly in the bilayer (F_D(uni)) as a function of the domain area and the relative domain radius. The donor lifetime was 6 ns in the L_o and L_d phase (*left*) or it was 6 ns in the L_d and 8 ns L_o phase (*right*). For [$K_D = 0.01$, $K_A = 0.01$], [$K_D = 3$, $K_A = 3$], [$K_D = 5$, $K_A = 5$], and [$K_D = 10$, $K_A = 10$], the ratio F_D(uni)/F_D is displayed instead. Values >1.5 are displayed with the same color as the limiting value.

in which donors and acceptors prefer the L_d phase, i.e., outside the domains, is less useful for radii $\approx R_0$. This fact is illustrated in Fig. 2. Even for D/A pairs with high affinity to L_d phase ($K_D = K_A = 0.01$), domains must occupy >20% to resolve radii $>1.5\ R_0$. The FRET approach fails completely if donors are inefficiently excluded from the domains. Though such probes are available, they are not useful.

Case III means that donors preferentially reside in domains and acceptors are excluded from them, respectively. Here $K_A = 0.01$ was used, because probes with such high affinity to L_d phase are available. The value of $K_D = 5$ is high enough for observing domains over a broad range of sizes. However, domains that occupy <2.5% of the overall area and domains with radii $<1\ R_0$ and occupying ≤10% of the area are beyond the experimental resolution. To be able to monitor the initial states of domain formation ($R < R_0$ and area of a few %), the values of $K_D \geq 40$ are needed to reach the orange region even for a radius of $0.5\ R_0$ and area of 1% (compare to the Supporting Material). The resolution rapidly decreases for $K_D < 5$. At $K_D = 3$, domain fractions between 7.5 and 40% and radii ranging between 1.5 and $8\ R_0$ still belong in the yellow-green region. At $K_D = 1$, domains that cover 20–40% with radii from 2 to $8\ R_0$ are clearly resolvable. The role of donors and acceptors may be exchanged, but that does not have an impact

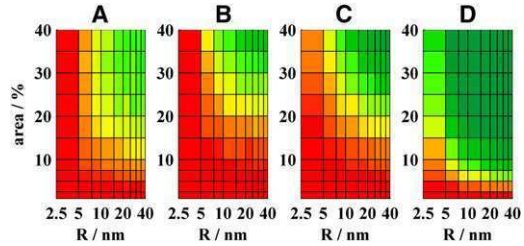

FIGURE 3 Resolution of FRET represented by the ratio F_D/F_D(uni) as a function of the domain area and the radius for (*A*) NBD-PE/Rhodamine-PE, (*B*) BODIPY-PC/fast-DiI, (*C*) Perylene/DiI with $K_D = 1$ and $K_A = 0.01$, and (*D*) Perylene/DiI with $K_D = 3$ and $K_A = 0.01$. See Fig. 2 for more details.

on the conclusions. Although membrane labels with a preferred affinity to the L_o phases are practically limited to labeled cholera toxins, this circumstance can be utilized to determine domains down to 5 nm by TR FRET. Thus, the design of new domain markers improves simple steady-state experiments.

VALIDITY OF FRET EXPERIMENTS USING VARIOUS D/A PAIRS

NBD-PE/Rhodamine-PE FRET ($R_0 \approx 5$ nm)

For NBD-PE/Rhodamine-PE FRET ($R_0 \approx 5$ nm) (5), NBD-PE has, in POPC/Sph/Chol bilayer, a modest affinity to the L_o domains with $K_D = 4.3$, whereas Rhodamine-PE with $K_A = 0.37$ tends to stay in the L_d phase. Nanodomains with $R > 10$ nm and area >15% can be characterized (compare to Fig. 3 *A*). On the other hand, nanodomains with $R < 5$ nm or area <5% are beyond the resolution.

BODIPY-PC/fast-DiI FRET ($R_0 = 6.5$ nm)

This pair with K_D and K_A at ~0.1 was used to characterize domains in the DOPC/DSPC/Chol system by steady-state measurements (3). The authors speculated that the domains had sizes in the range of 2–8 nm. According to our study, the domains that have radii >5 nm and occupy >25% of the entire surface can be detected. Another possibility would be domains constituting a lower amount of the bilayer (down to 15%) and having $R > 10$ nm (compare to Fig. 3 *B*).

Alexa Fluor 647 cholera toxin/DiD FRET ($R_0 = 5.4$ nm)

Concerning the K values for this pair, $K_D = 11 \pm 5$ (4) or 6 ± 3 as determined by us (compare to the Supporting Material) and $K_A = 0.004$, it is the best pair available so far, which could determine radii down to 5 nm and areas of only few % (compare to Fig. 2, $K_D = 3$–10, $K_A = 0.01$; concerning the limits, there is no difference between $K_A = 0.01$ or $K_A = 0.004$). Disadvantage of cholera toxins is that they affect the phase composition. (Note that Alexa Fluor 647 cholera toxin is a product of Molecular Probes, Eugene, OR.)

Perylene/fast-DiI FRET ($R_0 = 5.1$ nm)

Perylene/fast-DiI FRET ($R_0 = 5.1$ nm) (2) seems to be a useful D/A pair, with acceptors participating in the L_d phase. However, there is a complicated picture concerning 1), photophysics of perylene and 2), the correct value of K_D: a), The lifetime of perylene changes with the lipid phase (i.e., 6 ns and 8 ns in L_d and L_o phase, respectively; compare to the Supporting Material). This property improves the resolution for the case III moderately (compare to Fig. 3, *C* and *D*). The improved detection is ascribed to an additive mechanism (i.e., slower FRET, with respect to the UD of D/A pairs plus emission of donors from the domains on a longer timescale). However, due to 1/6 power dependence of FRET efficiency on the lifetime, the FRET rate remains nearly constant as compared to the case when the donor-lifetime does not depend on the phase (compare to the Supporting Material). b), Limitations are apparent for $K_D \leq 5$ and gradually grow with $K_D \rightarrow 1$. In this study, a value $K_D = 0.8$ is obtained for perylene in the DOPC/DOPG/Chol/Sph bilayer. Hammond et al. (2) claim that perylene exhibits a pronounced affinity to the L_o phase. Based on the simulations and even by using an ~4× higher K_D value as determined by us ($K_D = 3$, compare to Fig. 3) and a low value of K_A for fast-DiI ($K_A = 0.01$), the formation of nanodomains <20 nm cannot be excluded due to the absence of changes in perylene steady-state intensities for the DOPC/DOPG/Sph/Chol/GM1 system (2). Determining the resolution limits of perylene/DiI FRET experiments is difficult because of the above-mentioned uncertainties. A reasonable guess is that $K_D = 1$, i.e., domains <20 nm are only visible for areas ≥20%.

CONCLUSIONS

TR FRET, and currently available probes, enable resolution of nanodomains <20 nm. The best approach appears to be D/A preferring a different phase when a D/A pair with $K_D = 5$ and $K_A = 0.01$ already resolves a broad range of domain sizes. However, only probes with high affinity to the L_o phase will enable detection of very small domains or domains occupying only a few percent of the bilayer area. A situation when D/A prefer the same phase, either the L_d or L_o phase, is not yet a realistic approach for determining domain sizes <20 nm.

SUPPORTING MATERIAL

Five figures and one table are available at http://www.biophysj.org/biophysj/supplemental/S0006-3495(11)01309-9.

ACKNOWLEDGMENTS

This work was financially supported by the Grant Agency of the Czech Republic via P208/10/1090 (J.H. and R.S.) and P208/10/0376 (M.H.), by the Grant Agency of Charles University via 3130/2011 (M.S.), and the Swedish Research Council (L.B.-Å.J.).

REFERENCES and FOOTNOTES

1. Eggeling, C., C. Ringemann, …, S. W. Hell. 2009. Direct observation of the nanoscale dynamics of membrane lipids in a living cell. *Nature.* 457:1159–1162.
2. Hammond, A. T., F. A. Heberle, …, G. W. Feigenson. 2005. Crosslinking a lipid raft component triggers liquid ordered-liquid disordered phase separation in model plasma membranes. *Proc. Natl. Acad. Sci. USA.* 102:6320–6325.
3. Heberle, F. A., J. Wu, …, G. W. Feigenson. 2010. Comparison of three ternary lipid bilayer mixtures: FRET and ESR reveal nanodomains. *Biophys. J.* 99:3309–3318.
4. Chiantia, S., J. Ries, …, P. Schwille. 2006. Combined AFM and two-focus SFCS study of raft-exhibiting model membranes. *ChemPhysChem.* 7:2409–2418.
5. de Almeida, R. F. M., L. M. S. Loura, …, M. Prieto. 2005. Lipid rafts have different sizes depending on membrane composition: a time-resolved fluorescence resonance energy transfer study. *J. Mol. Biol.* 346:1109–1120.
6. Johansson, L. B. A., S. Engstrom, and M. Lindberg. 1992. Electronic energy transfer in anisotropic systems. 3. Monte Carlo simulations of energy migration in membranes. *J. Chem. Phys.* 96:3844–3856.

Limitations of Electronic Energy Transfer in the Determination of Lipid Nanodomain Sizes

Radek Šachl,[†‡] Jana Humpolíčková,[†] Martin Štefl,[†] Lennart B.-Å. Johansson,[‡] and Martin Hof[†]

[†]Department of Biophysical Chemistry, J. Heyrovský Institute of Physical Chemistry of the Academy of Sciences of the Czech Republic, Prague, Czech Republic; and [‡]Department of Chemistry: Biophysical Chemistry, Umeå University, Umeå, Sweden

Supplementary material

MC simulations (1)

The simulation started by redistribution of probes between the circular domains and the remaining bilayer according to the affinity of the probes to the particular phase. In order to obtain the generated decay the time a randomly excited D molecule spends in the excited state was calculated. This time depends on the overall energy transfer rate Ω_i according to $\Delta t_i = -\ln\alpha/\Omega_i$, where α is a randomly generated number between 0-1. New configurations were generated 3000 times, whereas each configuration step was used 100 times. Periodic boundary conditions were used and the size of the replicated box was 20 R_0 × 20 R_0. Input parameters of the simulation were: area the domains occupy in the bilayer, the domain radius, distribution constants of D:s and A:s, R_0, the D-lifetime and surface concentration of D:s/A:s. Simulations have been carried out under the dynamic limit conditions and among isotropically oriented DA.

Additional figures showing the limits of FRET

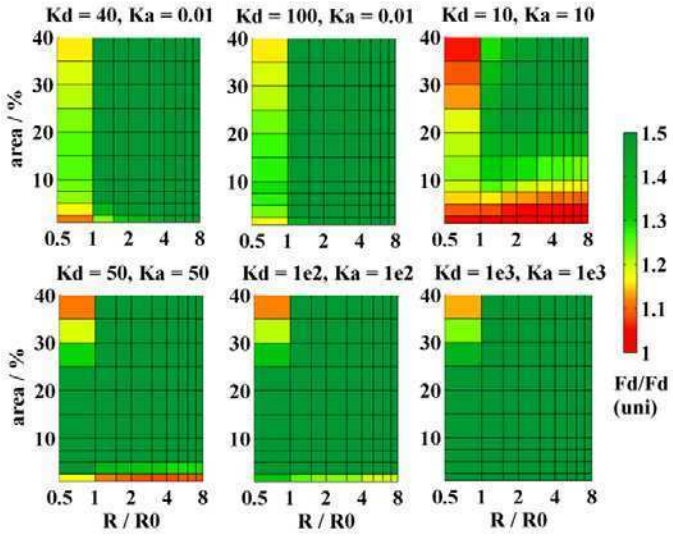

Fig. S1: Resolution of FRET represented by the ratio of the intensity of D (F_D) to the intensity of D when DA are distributed uniformly in the bilayer (F_D(uni)) as a function of the domain area and the domain radius divided by R_0. Lifetime of D was fixed at 6 ns for both L_o and L_d. The red colour corresponds to the classification (clas.) 1, orange colour to the clas. 2, yellow colour to the clas. 3 and green colour to the clas. 4. For [K_D = 10, K_A = 10], [K_D = 50, K_A = 50], [K_D = 100, K_A = 100] and [K_D = 1000, K_A = 1000] the ratio F_D(uni)/F_D is displayed instead. Values above 1.5 are displayed with the same colour at the limiting value.

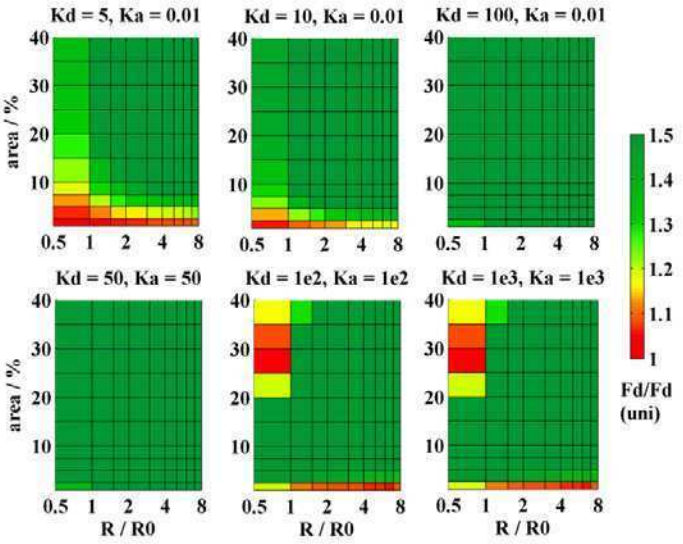

Fig.S2: Resolution of FRET represented by the ratio of the intensity of D (F_D) to the intensity of D when DA are distributed uniformly in the bilayer (F_D(uni)) as a function of the domain area and the domain radius divided by R_0. Lifetime of D was 6 ns the L_d and 8 ns in the L_o phase. For [K_D = 50, K_A = 50], [K_D = 100, K_A = 100] and [K_D = 1000, K_A = 1000] the ratio F_D(uni)/F_D is displayed instead. For more details see Fig. 1.

Lifetime of perylene

As is obvious from Fig. S3 lifetime of perylene depends on the physical state of the lipid bilayer, and possibly also on its chemical composition. For the L_o state the fitting routine yielded A_1 = 0.87, τ_1 = 8 ns A_2 = 0.13, τ_2 = 3.24 ns with the average lifetime of 7.8 ns whereas for the L_d state the optimization minimum was reached at A_1 = 0.93, τ_1 = 6.6 ns A_2 = 0.07, τ_2 = 3.00 ns with the average lifetime of 6.45 ns. A_i are preexponential factors and τ_i the fluorescence lifetimes. Since perylene has K around 1it could be used for detection of domains that occupy at least tens of percent of the entire bilayer surface.

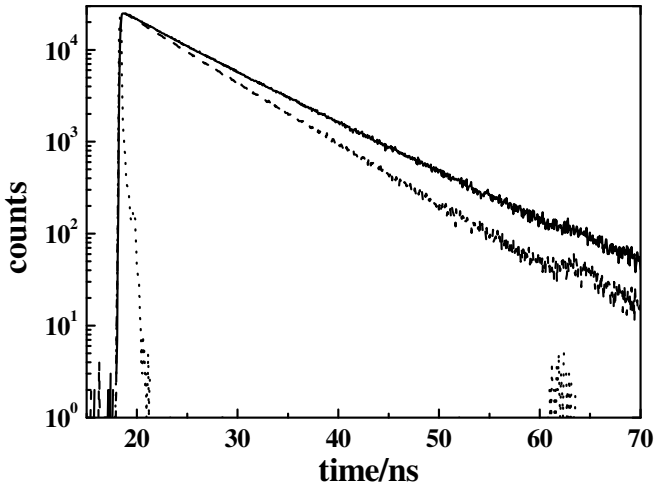

Fig. S3: Time-resolved fluorescence decay of perylene in Sph/Chol (70/30) bilayer, which was in the L_o state (solid), and DOPC/Chol bilayer, which was in the L_d state (dashed). Lamp profile is displayed as well (dotted).

Distribution constants of some probes with increased affinity to the L_o raft phase in bilayers containing cholesterol

Tab.S1: Distribution coefficients of some probes that have increased affinity to the L_o phase in bilayers with Chol.

Probe	Bilayer composition	*K*
Perylene	DOPC/Sph/Chol/DOPG/DPPE-biotin (29/39/25/5/2)	0.8 ± 0.2
Cholera toxin	DOPC/Sph/Chol/DOPG/DPPE-biotin (44/24/25/5/2)	6 ± 3
Cholera toxin	DOPC/Sph/Chol	11 ± 5 (2)
NBD-DPPE	POPC/Sph/Chol	4.3 ± 1.2 (3)

Determination of distribution coefficients

Distribution coefficients of Alexa488 labelled cholera toxin subunit B (CtxB-488) and perylene between L_o and L_d phase was determined in giant unilamellar vesicles (GUVs). GUVs were prepared by a gentle hydration approach. 1 mL of lipid mixture (*cf.* Table 1) in chloroform containing 1 mg of lipids was dried with a rotary evaporator and kept for additional two hours under vacuum. Thin lipid film was hydrated with 3 mL of pre-warmed buffer (10 mM HEPES, 150 mM NaCl, 1 mM $CaCl_2$, 0.1 M sucrose, pH = 7) saturated with nitrogen. The tube was then sealed, heated to 60 ºC, kept overnight at this temperature, and slowly cooled down. White cloud containing liposomes was gently vortexed before further use. The measurements on GUVs were performed in FCS2 chamber (Bioptechs, Butler, PA). The chamber with a BSA-biotin/streptavidin coated coverslip was filled with a buffer solution (10 mM HEPES, 150 mM NaCl, 1 mM $CaCl_2$, 0.1 M glucose, pH = 7), 20 µL of the solution containing GUVs was added and after 30 minutes when enough liposomes were attached to the coverslip, the chamber was carefully flushed with excess of the buffer solution.

In the case of perylene, the dye was present already in the lipid mixture in chloroform. The probe-to-lipid ratio was 1:200. In the case of CtxB-488, 20 µL of CTxB-488 (1 µg/mL) was added to the chamber containing already immobilized GUVs and after 15 minutes flushed with excess of the buffer solution.

Images of the GUV cross-sections were acquired with MicroTime 200 inverted confocal microscope (PicoQuant, Germany) with a water immersion objective (1.2 NA, 60x) (Olympus, Hamburg, Germany). Pulsed diode lasers (LDH-P-C-470, 470 nm, and LDH-D-C-440, 440 nm PicoQuant, Berlin, Germany) with 40 MHz repetition rate were used. The signal was detected on the single photon avalanche diode (SPCM-AQR-14, PerkinElmer, Waltham, MA) using 515/50 (CtxB-488) and 480/40 (perylene) band pass filters (Chroma Rockingham, VT), respectively.

In the images, pixels corresponding to L_o and L_d phase were identified and the mean pixel intensity of the two phases (I_{Lo} and I_{Ld}) calculated. The distribution coefficient was obtained as:

$$K = \frac{I_{L_o}}{I_{L_d}} \cdot \frac{\tau_{L_d}}{\tau_{L_o}},$$

where τ stands for fluorescent lifetime of the label in the given phase (important for perylene).

FRET efficiency versus fluorescence lifetime

The lifetime of perylene changes with the lipid bilayer composition (*i.e.* 6 ns and 8 ns in L_d and L_o phase, respectively; *cf.* SI). This property improves FRET resolution. This is because the decay becomes slower due to the slower FRET (as compared to the uniform distribution of D/A) as well as the fact that donors residing in the rafts emit on a longer timescale. The FRET rate remains, however, nearly constant with respect to the case when D-lifetime is not influenced by the phase composition. This happens because of the 1/6 power dependence of the FRET efficiency on the lifetime and is demonstrated in Fig. S4.

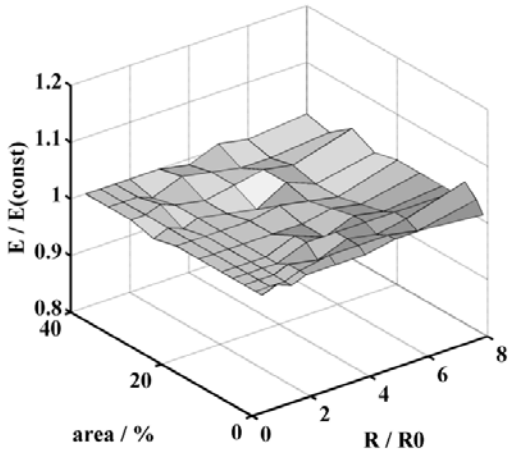

Fig. S4: Ratio of the FRET efficiencies with the lifetime of 6 ns in L_o and L_d , E, and the lifetime of 6 ns in L_d and 8 ns in L_o, E(const) as a function of the domain radius R/R_0 and the domain area.

Influence of the z-positions on the results

As is shown in Fig. S5 vertical z-position of the donors in the bilayer has only a modest impact on the generated curves. The conclusions drawn in the paper are thus general.

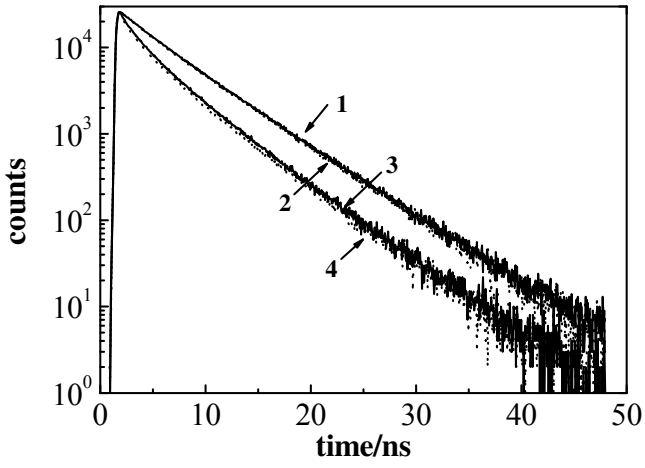

Fig. S5: Generated decays for D with K_D = 100, K_A = 100 localized at the interface (solid, curve 1) or inside the bilayer (dotted, curve 2) and with K_D = 1, K_A = 1 localized at the interface (solid, curve 3) or inside the bilayer (dotted, curve 4).

Supporting references

1. Johansson, L. B. A., S. Engstrom, and M. Lindberg. 1992. Electronic Energy Transfer in Anisotropic Systems. 3. Monte Carlo Simulations of Energy Migration in Membranes. J. Chem. Phys. 96:3844-3856.
2. Chiantia, S., J. Ries, N. Kahya, and P. Schwille. 2006. Combined AFM and two-focus SFCS study of raft-exhibiting model membranes. ChemPhysChem 7:2409-2418.
3. de Almeida, R. F. M., L. M. S. Loura, A. Fedorov, and M. Prieto. 2005. Lipid rafts have different sizes depending on membrane composition: A time-resolved fluorescence resonance energy transfer study. J. Mol. Biol. 346:1109-1120.

IV

Dynamics and Size of Crosslinking-Induced Lipid Nanodomains in Model Membranes

Štefl, M., Šachl, R., Humpolíčková, J., Cebecauer, M., Macháň, R., Kolářová, M., Johansson, L.B.-A., Hof, M.
Biophysical Journal, 102(9), 2104-2113, 2012

Dynamics and Size of Cross-Linking-Induced Lipid Nanodomains in Model Membranes

Martin Štefl,[†] Radek Šachl,[†‡] Jana Humpolíčková,[†*] Marek Cebecauer,[†] Radek Macháň,[†] Marie Kolářová,[†] Lennart B.-Å. Johansson,[‡] and Martin Hof[†]

[†]Department of Biophysical Chemistry, J. Heyrovsky Institute of Physical Chemistry of the Academy of Sciences of the Czech Republic, Dolejškova, Prague, Czech Republic; and [‡]Department of Chemistry: Biophysical Chemistry, Umeå University, Umeå, Sweden

ABSTRACT Changes of membrane organization upon cross-linking of its components trigger cell signaling response to various exogenous factors. Cross-linking of raft gangliosides GM1 with cholera toxin (CTxB) was shown to cause microscopic phase separation in model membranes, and the CTxB-GM1 complexes forming a minimal lipid raft unit are the subject of ongoing cell membrane research. Yet, those subdiffraction sized rafts have never been described in terms of size and dynamics. By means of two-color z-scan fluorescence correlation spectroscopy, we show that the nanosized domains are formed in model membranes at lower sphingomyelin (Sph) content than needed for the large-scale phase separation and that the CTxB-GM1 complexes are confined in the domains poorly stabilized with Sph. Förster resonance energy transfer together with Monte Carlo modeling of the donor decay response reveal the domain radius of ~8 nm, which increases at higher Sph content. We observed two types of domains behaving differently, which suggests a dual role of the cross-linker: first, local transient condensation of the GM1 molecules compensating for a lack of Sph and second, coalescence of existing nanodomains ending in large-scale phase separation.

INTRODUCTION

Plasma membrane serves as an interface between exogenous signal and cellular function. Molecular organization of the membrane landscape, such as clustering of its components, therefore plays a crucial role in the variety of membrane-associated processes. In particular, ligand-induced clustering has been related to various aspects of plasma membrane, such as signaling of immune receptors (1,2). Similarly, cross-linker-induced patching of membrane components induced signaling in cells (3–5). In addition, it was shown to affect partitioning of saturated phospholipid analogs between different lipid phases (6) and to promote large-scale phase separation accompanied with spatial redistribution of transmembrane peptides in model membranes (7). It has not been proven so far if formation of cross-linker-induced nanoscaled domains along the trajectory heading from a liquid-disordered (L_d) to liquid-ordered (L_o) phase in a phase diagram precedes the large-scale phase separation.

Direct observation of nanoscaled heterogeneities in plasma membrane by means of optical microscopy fails either due to its poor resolution or anticipated transient character of rafts. Cholera toxin β (CTxB)-induced nanosized clusters in membranes of mildly fixed resting cells have been visualized by means of near-field scanning optical microscopy (8). Its resolution depends on the size of the used subwavelength aperture, which is typically around 80 nm. The study evidences structural connectivity between raft-associating proteins and the clusters that are established even though direct redistribution of the proteins to the clusters does not occur, concluding that the resting plasma membrane is prealigned toward large-scale coalescence upon cell activation.

In living cells, dynamic characterization of lipid rafts has been achieved by the combination of fluorescence fluctuation analysis and stimulated emission depletion (STED) microscopy. Dependence of mean transition time through the STED focal area on its size reveals transient trapping of raft integrating lipids and glycosylphosphatidylinositol-anchored proteins in molecular clusters. Authors deduce that the trapped molecules dwell within areas with $<$20 nm diameter (9).

Cross-linking of gangliosides GM1 by its pentavalent ligand CTxB was addressed in a vast amount of studies. It has been shown that clustering of GM1 via CTxB induces microscopic L_o and L_d phase separation both in giant unilamellar vesicles (GUVs) formed by lipid mixtures consisting of dioleoylphosphatidylcholine (DOPC), sphingomyelin (Sph), and cholesterol in a certain ratio (7) and in plasma membrane spheres (10).

In agreement with commonly observed cholesterol and Sph importance for lipid raft formation (11), the cholesterol dependence of CTxB-induced clustering was demonstrated in cell membranes (8) and the Sph requirement for CTxB triggered large-scale phase separation was evidenced in the model membranes (7). These findings suggest that the cross-linker will have the greatest impact if the lipid composition approaches the phase separation boundary, most probably close to the single L_d phase as indicated by the work of de Almeida et al. (12).

In this work, we aimed to investigate early stages of the cross-linking-induced phase separation, i.e., formation,

Submitted January 26, 2012, and accepted for publication March 23, 2012.

*Correspondence: jana.humpolickova@jh-inst.cas.cz

Editor: Petra Schwille.

0006-3495/12/05/2104/10 $2.00

doi: 10.1016/j.bpj.2012.03.054

size, and dynamic properties of nanodomains in dioleoylphosphatidylcholine (DOPC)/Sph/cholesterol mixtures containing a small percentage of GM1 upon their pentamerization with CTxB. By means of z-scan fluorescence correlation spectroscopy (FCS) (13) and simulations published by Wawrezinieck et al. (14), the distribution coefficient of CTxB between the two phases and the residential time within the nanodomains are estimated. Size of the nanodomains is determined by Förster resonance energy transfer (FRET) from donor-labeled CTxB to an acceptor, a lipid tracer preferentially segregating to the L_d phase, and Monte Carlo (MC) modeling of the measured data. We demonstrate the existence of two types of nanodomains differing in size and ability to confine CTxB-GM1 complexes.

EXPERIMENTAL SECTION

DOPC, porcine brain Sph, cholesterol, 1,2-dioleoyl-*sn*-glycero-3-phosphoglycerol (DOPG), GM1, and 1,2-dipalmitoyl-*sn*-glycero-3-phosphoethanolamine-*N*-(cap biotinyl) (Biotinyl Cap PE) were purchased from Avanti Polar Lipids (Alabaster, AL). Bodipy FL DHPE, $DiIC_{18}$ (5)-DS (DiD), Alexa Fluor 488- and Alexa Fluor 647-labeled CTxB (CTxB-488, CTxB-647) were purchased from Invitrogen (Carlsbad, CA). Perylene, streptavidin, biotin-labeled bovine serum albumin (biotin-BSA), and CTxB were purchased from Sigma (St. Louis, MO).

GUV preparation

GUVs were prepared by a gentle hydration approach described elsewhere (15). 1 mL of lipid mixture in chloroform containing 1 mg of lipids was dried with a rotary evaporator and kept for an additional 2 h under vacuum. Thin lipid film was hydrated with 3 mL of prewarmed buffer (10 mM HEPES, 150 mM NaCl, 1 mM $CaCl_2$, 0.1 M sucrose, pH = 7) saturated with nitrogen. The tube was then sealed, heated to 60°C, kept overnight at this temperature, and slowly cooled. White cloud containing liposomes was gently vortexed before further use. All the prepared lipid mixtures contained 5 mol % of DOPG, negatively charged lipid necessary for the given preparation technique and 4 mol % of biotinyl Cap PE necessary for attaching GUVs to BSA-biotin/streptavidin-coated glass. All the measurements on GUVs were performed in a FCS2 chamber (Bioptechs, Butler, PA). The chamber with a coated coverslip was filled with 200 μL of buffer solution (10 mM HEPES, 150 mM NaCl, 1 mM $CaCl_2$, 0.1 M glucose, pH = 7), 20 μL of the solution containing GUVs was added and after 30 min when enough liposomes were attached to the coverslip, the chamber was carefully flushed with excess of the buffer solution.

FCS and fluorescence lifetime imaging microscopy-FRET measurements

Both types of measurements were performed on a MicroTime 200 inverted confocal microscope (PicoQuant, Berlin, Germany) with a water immersion objective (1.2 NA, 60×) (Olympus, Hamburg, Germany). Pulsed diode lasers (LDH-P-C-470, 470 nm, and LDH-D-C-635, 635 nm PicoQuant) with 10 MHz repetition rate each were used. The lasers were pulsing alternatively to avoid artifacts caused by signal bleed-through. The signal was split on two single photon avalanche diodes using 515/50 and 685/50 band pass filters (Chroma, Rockingham, VT) for the green and red channel, respectively. In the case of the FCS measurements, laser intensity at the back aperture of the objective was around 5 μW for each laser line. The z-scan was performed on the top of selected unilamellar liposomes. Membrane was first placed to the laser beam waist, and then moved 1.5 μm below the waist and consequently vertically scanned in 20 steps (150 nm spaced). At every position, a 60 s measurement was performed. Details of the data analysis are given in the Supporting Material. For the fluorescence lifetime imaging microscopy (FLIM)-FRET measurements, intensities of the lasers were chosen low enough to avoid a pile-up effect, i.e., around 1 μW for 470 nm and <0.1 μW for 635 nm. Each GUV was scanned in the cross section, an image of 512 × 512 pixels (0.6 ms/pixel) was acquired.

For z-scan FCS measurements, membrane was stained with Bodipy FL DHPE (BDP-DHPE) in label/lipid ratio 1:50000. CTxB-647 was stepwise added to the immobilized GUVs. 15 min after the portion of CTxB-647 was added, the FCS2 chamber was flushed with excess of a buffer and then several z-scans FCS experiments were performed. Portions of CTxB-647 were added in the following manner: 1), 10 μL (1 μg/mL), 2), 2 μL (20 μg/mL), 3), 4 μL (20 μg/mL). The final concentrations of the CTxB-647 in the FCS2 before final flushing were 1), 0.05 μg/mL, 2), 0.2 μg/mL, and 3), 0.4 μg/mL.

For the two-color cross correlation FCS experiments, 4 μL of both CTxB-488 and CTxB-647 (20 μg/mL) was added to the immobilized GUVs, which corresponds to 0.4 μg/mL in the final solution.

For FLIM- FRET measurements, membrane was stained with DiD (acceptor) in label/lipid ratio 1:100. 20 μL of CTxB-488 (1 μg/mL) was added to the GUVs (i.e., final concentration of CTxB in FCS2 was 0.1 μg/mL), after 15 min GUVs were flushed with buffer, FLIM images of selected liposomes were taken, 10 μL of nonlabeled CTxB (2 mg/mL) were added (i.e., 100 μg/mL in final solution – complete saturation), after 15 min flushed again, and FLIM images of the same liposomes were again acquired.

All measurements presented in this work were held at 24°C.

RESULTS AND DISCUSSION

Cross-linker and lipid dynamics characterized by z-scan FCS

Because nanodomains are expected to form in the region close to the phase separation boundary, literature available phase diagrams were inspected (see Fig. 1). The solid curve in Fig. 1 stands for the phase separation boundary obtained from an electron spin resonance experiment performed by Smith et al. as well as the tie-lines (16). The dotted curve

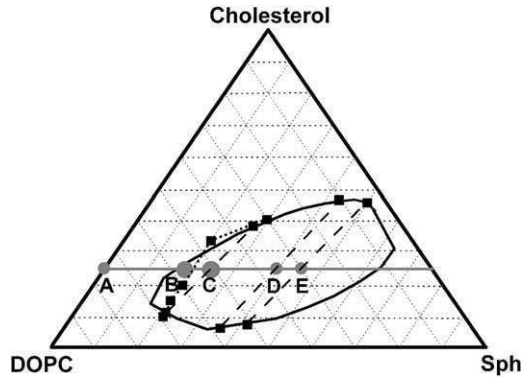

FIGURE 1 Ternary phase diagram for DOPC/Sph/Cholesterol lipid mixtures given in the literature: solid curve, tie-lines, and the dotted curve were published by Smith et al. (16) and Farkas et al. (17), respectively. The line connecting points **A** to **E** denotes constant cholesterol content. All measurements were done in marked points **A** to **E** corresponding to the lipid compositions given in Table 1.

shows the boundary observed by Farkas et al. by means of diffraction limited optical microscopy (17). Both of the two boundary lines were acquired for systems similar to the one investigated here, however differing in details such as resolution of the used observation technique, presence of a charged lipid, and GM1 or type of Sph. We would like to point out that the literature facts shown here serve only as a qualitative basis for presentation of our own data, the precise position of the boundary line as well as the exact tie-line field are beyond the scope of this contribution.

In the system of our interest, GUVs created from a lipid mixture corresponding to the selected compositions (see Table 1) were prepared having been stained with Bodipy FL DHPE (BDP-DHPE) which preferentially resides in the L_d phase (18). Phase separation along the marked line, denoting constant content of cholesterol, was investigated. In the putative boundary region, the compositions **B** and partially **C** (see below) showed no optically resolvable phase separation. Of note, liposomes created for a given composition were not absolutely uniform, particularly in the composition **C**; some GUVs (minority of them) were already phase separated. To avoid ambiguity caused by the different phase states of particular GUVs at this composition, all measurements were held in the nonseparated GUVs at compositions **A**, **B**, and **C** (majority was nonseparated) and in the L_d phase of the separated GUVs in the remaining cases. It is a commonly observed phenomenon that individual lipids in GUVs are not evenly distributed. Thus, it is difficult to relate the observed behavior to the precise lipid composition. We experienced that in the composition **C**, the phase separated GUVs behaved fundamentally different (similar to the composition **D**) compared to those that were (optically) not separated yet. Therefore, we focused only on those nonseparated implying that their average lipid composition might have contained less Sph and/or cholesterol as claimed in the Table 1. Furthermore, we show that the chosen nonseparated GUVs are phase separated on the length scale that is beyond the optical resolution.

First, diffusion of BDP-DHPE was measured in the top membrane of several selected GUVs by means of z-scan FCS. The lateral diffusion coefficient for the BDP-DHPE did not significantly differ for all tested compositions giving values of around $7.1 \pm 0.9\ \mu m^2.s^{-1}$ at 24°C.

Alexa Fluor 647-labeled CTxB (CTxB-647) was then added to the flow cell containing immobilized GUVs in portions so that the concentration of the cross-linker was stepwise increasing (see Material and Methods). After each addition, two-color z-scan FCS was simultaneously performed for CTxB-647 and BDP-DHPE (19). Diffusion of BDP-DHPE did not undergo any change upon CTxB-647 addition in all the investigated compositions.

The data obtained from the two-color z-scan FCS approach were evaluated in two different ways:

1. The correlation curves corresponding to the situation when a membrane is located in the middle of the laser focus were fit with a model accounting for free two-dimensional diffusion (see the Supporting Material). The mean transition time τ_D, the average time a labeled molecule stays in the laser-illuminated area, served as a main readout parameter. The values of τ_D for individual lipid composition at various loads of the CTxB-647 are summarized in Table 2.

Visually, the correlation curves for the investigated compositions are compared in Fig. 2.

2. Because the two-color FCS measurements were performed in the z-scan manner, autocorrelation functions were measured at different positions of the model membrane with respect to the beam waist, i.e., fluctuations arising from illuminated areas differing in size were acquired. Dependence of mean transition time, the average time a molecule passes though the illuminated area, on the area size, provides information on the diffusion character of the fluorescent particles (14).

In Fig. 3, mean transition time is plotted versus relative size of the illuminated region, which shows a so-called apparent diffusion law (see the Supporting Material for details) for BDP-DHPE (L_d phase marker) and for CTxB-647 in differently composed GUVs.

Even though the z-scan FCS approach does not enable direct accessing of diffusion properties in the areas smaller than the diffraction limit, such as FCS combined with STED microscopy (9), or what zero-mode waveguides for nanometric apertures (20) can do, the slopes and the offsets of the depicted plots allow mapping of the apparent diffusion laws the molecules obey. Wawrezinieck et al. (14) have shown by means of kinetic MC simulations that the positive offset value can result from the formation of domains. The apparent diffusion law is described by a simple formula:

$$\tau_D^{app} = t_0 + \frac{\omega^2}{4D_{eff}},$$

where $\tau_D{}^{app}$ stands for mean transition time, t_0 is the temporal offset, ω is the beam waist radius, and D_{eff} corresponds to the effective diffusion coefficient. According to the proposed model, a raft-associating molecule freely diffuses in the nondomain region with a diffusion coefficient D_{free}, at the moment when it enters a domain its diffusion decreases and additionally, the molecule becomes confined

TABLE 1 Molar fractions of lipids in GUV lipid compositions discussed in this work

	DOPC	Sph	Chol.	DOPG	GM1
A	0.68	0	0.25	0.05	0.02
B	0.49	0.19	0.25	0.05	0.02
C	0.44	0.24	0.25	0.05	0.02
D	0.29	0.39	0.25	0.05	0.02
E	0.23	0.45	0.25	0.05	0.02

TABLE 2 Mean transition times of CTxB-647 through the illuminated spot—the minimum value obtained when membrane was centered in the beam waist

	A	B – low load	B – medium load	B – high load	C – low load	C – medium load	C – high load	D	E
τ_D/ms	6.6	5.9	40.3	46.5	12.8	14.6	12.0	7.1	22.1
Stdev/ms	0.08	0.21	2.24	10.54	0.92	2.86	6.82	0.66	4.99
n	4	6	2	5	4	3	5	3	4

n gives number of z-scans acquired for the given composition.

in the domain for a certain time τ_{conf}. Following this assumption a time-based distribution coefficient α can be defined as a fraction of time a molecule spends in the domain region on average. This leads to the expression for D_{eff}: $D_{eff} = (1-\alpha)D_{free}$ (details are in the Supporting Material). The t_0 value can be approximated by the following formula (14) $t_0 \approx 2\alpha\tau_{conf}$.

The results obtained by the two mentioned data treatments reveal different dynamics of the molecules of interest in the investigated compositions:

Composition **A** is a Sph free lipid mixture that serves as a blank experiment. Diffusion behavior of the CTxB-647 is independent of its load and the apparent diffusion law (Fig. 3) suggests free diffusion both for the labeled lipid and cross-linker molecules.

Composition **B** lies in the phase boundary region. Although the optical microscopy does not give any evidence of the phase separation and the diffusion of the labeled lipid is similar to the value obtained in composition **A**, diffusion behavior of the labeled cross-linker significantly differs from the Sph free system. Diffusion behavior of CTxB-647 in **B** i), is dependent on its load (Fig. 2, Table 2), and ii), the apparent diffusion law (Fig. 3) for high loads shows a significant temporal offset suggesting that the molecular motion may be trapped due to putative confinement in domains.

When the cross-linker load exceeds a certain threshold, substantially prolonged fluctuations in fluorescence intensity appear (Fig. 2, *lower part*) and are translated to almost a sevenfold longer transition time. The long transition times can be either caused by massive aggregation of CTxB at the membrane surface, forming large, slowly diffusing protein clusters, or due to the tendency of locally condensed GM1 molecules to coalesce into nanodomains confining the cross-linker molecules.

To investigate whether the mutual cross-linker interactions or the interactions between lipid molecules rules the decreased diffusion, the following experiments were carried out: i), relative brightness (number of detected photons generated by a single molecule/cluster/s) of CTxB-647 was calculated for every concentration used. ii), Equimolar mixture of CTxB-647 and Alexa Fluor 488-labeled CTxB (CTxB-488) was applied for cross-linking of GM1 followed by a cross correlation FCS experiment. Although the relative molecular brightness of CTxB-647 increased from 2.2 ± 0.5 (low load) to 5.0 ± 1.7 (high load) kHz per

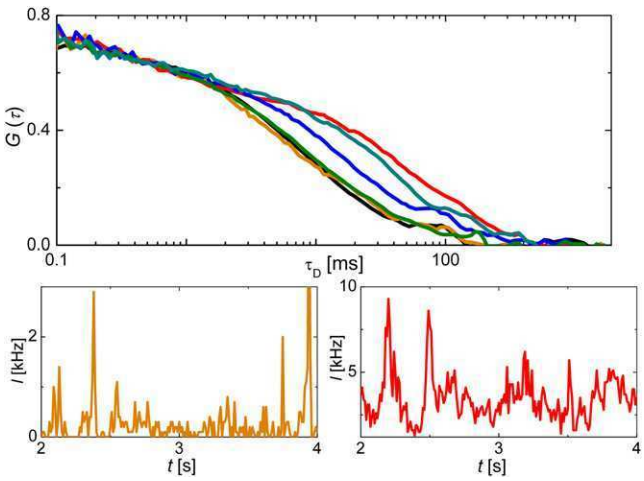

FIGURE 2 Upper part: autocorrelation curves for CTxB-647 in upper GUV membrane centered in the waist of the focal spot at different lipid compositions: **A** (*black*), **B** – low load of CTxB-647 (*orange*), **B** – high load of CTxB-647 (*red*), **C** (*blue*), **D** (*olive*), **E** (*dark cyan*). Lower part: intensity traces for CTxB-647 in **B** composed membranes at low (*orange*) and high (*red*) load of CTxB-647.

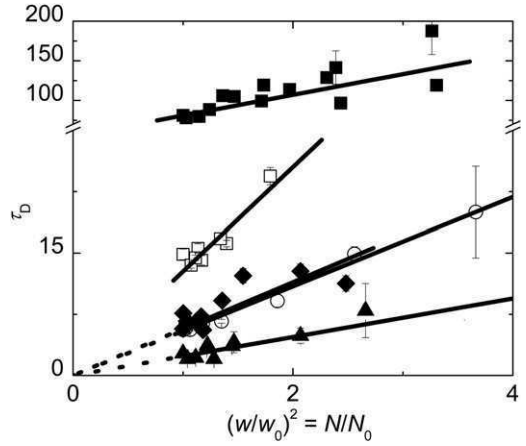

FIGURE 3 Apparent diffusion laws (dependence of the mean transition time through the illuminated spot on its relative size) obtained for diffusion of CTxB-647 in membranes composed of the lipid mixtures: **A** (*open circles*), **B** – low (*diamonds*), and high (*solid squares*) load of the cross-linker, and **C** (*open squares*). Diffusion law for BDP-DHPE (*triangles*) in **B** composed membrane at high cross-linker load is shown for comparison. Error bars represent standard errors of the mean. The dotted lines are guides for eyes, values of fitting parameters are given in Table S1.

particle, no detectable evidence of cross correlation between signals from the two dyes appeared (see Table S2 and Fig. S2). This suggests that CTxB-GM1 complexes were further associated, which is also supported by the FRET data (see below), however, motion and residing of the individual complexes in those assemblies is independent of one another, which indicates that it is, indeed, an interaction between lipids that drives the CTxB-GM1 complexes together.

Character of the diffusion represented by the diffusion law shown in Fig. 3 also changes at high load of the cross-linker. Analysis of the dependence of the diffusion time on the illuminated spot size according to the model proposed by Wawrezinieck et al. gives α of around 0.85, which is the time fraction when the motion of the cross-linker is trapped, the confinement time τ_{conf} was calculated to be around 30 ms.

Composition **C** still falls to the boundary region, because a majority of the GUVs do not show any phase separation. Upon adding CTxB-647, some GUVs become phase separated as described by Hammond et al. (7), however, there is a vast majority of liposomes where no separation is optically detectable.

Even though composition **C** is assumed to contain a higher amount of Sph compared to **B**, and thus slower diffusion in **C** than in **B** would be naturally anticipated, the observed behavior contradicted these expectations (the comparison between these two compositions was independently repeated three times with an identical result). In **C**, i), no concentration dependence of the CTxB-647 transition time was evidenced, ii), all obtained transition times were significantly shorter than in high-loaded composition **B**, however at the same time significantly longer than in **A** and low-loaded **B**, and iii), as displayed in Fig. 3, the temporal offset t_0 in the apparent diffusion law is substantially smaller than in the case **B** (high load). Unfortunately, the t_0 value obtained from the z-scan FCS is rather sensitive to the data quality and the level of photobleaching. The t_0 value obtained for individual **C** composed GUVs oscillates in the range from 0 to 6 ms, which is clearly distinguishable from the composition **B**, but comparison with other compositions or drawing conclusions on the diffusion character would be too speculative.

Eventually, the composition **C** seems to have a tendency to form nanodomains as the apparent diffusion is substantially decreased and as FRET experiments confirm (see below). Such domains, however, have considerably different permeability for the GM1-CTxB complex. The complex is slowed down when entering a domain, but the time it stays confined in the domain is substantially shorter than in the high loaded composition **B**, i.e., it can leave the domain easier when approaching its boundary.

We hypothesize that compositions **B** and **C** contain two different kinds of nanodomains that confine GM1-CTxB complexes differently. The hypothesis explaining such observations assumes that i), in case **B**, the starting lipid mixture is homogeneous and the domains are formed when a certain cross-linker level is exceeded; and ii), in the lipid mixture **C**, the nanoscopic phase separation is already established before the addition of the cross-linker, which is in agreement with the fact that some GUVs are phase separated even on the large length scale and additionally it can be confirmed by FRET between perylene and $DiIC_{18}(5)$ (DiD) (Fig. S4, and the corresponding text). Added CTxB-647 in this case probably does not cause the separation, but only label already existing structures and/or help them coalesce.

Composition **D** lies in the L_d and L_o coexistence region. The notion of composition of individual phases can be obtained from the tie-lines drawn in Fig. 1. The L_d phase is depleted in cholesterol and it is probably the lack of cholesterol that prevents the L_d phase from forming nanodomains. Consequently, diffusion of CTxB-647 is almost identical to the diffusion in the composition **A**, which is expected to be homogeneous. This is in agreement with the documented need of cholesterol assistance for raft formation (9).

Composition **E**, which is similar to **D**, belongs to the two-phase region. Contrary to **D**, in the L_d phase of the composition **E,** additional Sph compensates for the decreased cholesterol level, and CTxB-647 diffusion again slows down similar to the case **B** (see Fig. 2, Table 2) and subwavelength domains within the L_d phase appear. In equilibrium however, those nanodomains would probably fuse with the microscopic L_o phase to minimize the line tension. Because this does not happen in **E**, we might speculate that the nanodomains do not only differ in size but also in the lipid composition. The accommodation of the two kinds of domains within single GUVs would also indicate that our hypothesis suggesting different domains in **B** and **C** is realistic.

Identification of nanodomains by FLIM-FRET using phasor analysis

Our fluorescence dynamics experiments indicate existence of subwavelength domains and allow for the estimation of dynamic parameters, such as time the raft-associating components reside in the domains. The alternative fluorescence method that can report on the existence of molecular assemblies and characterize them in terms of structure is the FLIM-FRET approach. In our experiments, energy transfer from labeled CTxB (CTxB-488, donor) to DiD (acceptor), a lipid tracer preferentially residing in the L_d phase, was monitored by changes in a fluorescence decay histogram of the donor. In the homogenous lipid bilayer, donor fluorescence decay is heavily affected by energy transfer to acceptors that are in the close vicinity of the donor. Noticeably, the donor decay is a result of broadly distributed energy transfer rates that depend on distance between the particular acceptor and the donor, which makes the decay rather

complex (21). When domains are formed or a large-scale coalescence occurs, donors and acceptors with different partitioning between the lipid phases become more separated and the effect of FRET is lowered.

To avoid problems with the complexity of donor decays and the parameter compensating effects when fitting with exponential functions, for purposes of FLIM, the graphical, nonfitting phasor plot approach was employed (22). Detailed description of the method applied in this work is given in the Supporting Material. Briefly, for each donor decay acquired at every pixel of the GUV image, one frequency of the intensity normalized Fourier transform is calculated according to the formula:

$$\begin{bmatrix} \mathrm{Re} \\ \mathrm{Im} \end{bmatrix} = \frac{1}{\sum_{i=1}^{L} I_i} \begin{bmatrix} \sum_{i=1}^{L} I_i \cos\frac{2\pi n}{L}(i-i_0) \\ \sum_{i=1}^{L} I_i \sin\frac{2\pi n}{L}(i-i_0) \end{bmatrix},$$

where Re and Im stand for real and imaginary parts of the value obtained via Fourier transform, I_i represents fluorescence intensity in the ith time-correlated single photon counting channel, L is the number of the channels, i_0 is a channel position of the decay rising edge, and n is an arbitrarily chosen frequency. Re and Im are coordinates of the position in the phasor plot that are assigned to the particular decay function reflecting the level of FRET. For all pixels in the image, these coordinates are calculated. The two-dimensional histogram of their occurrence depicts distribution of different decay functions within the image. Usually, one or more spots/clusters appear in the phasor plot corresponding to different types of decays (i.e., spatially resolvable areas with different acceptor distributions).

In our experiments, a small aliquot of CTxB-488 was added to immobilized GUVs heavily stained with DiD. The amount of CTxB-488 was chosen to correspond to the concentration level, where no significant changes in diffusion (at composition **B**) were observed. FLIM images were acquired for GUVs consisting of lipid compositions denoted in Fig. 1. As expected, GUVs without observable large-scale phase separation revealed one cluster of decays in the phasor plot (**A**, **B**, and **C**). Phase-separated GUVs showed either two components, low- and high-FRET, (**D**) spatially corresponding to the L_o and L_d phase, respectively, or only one component, low-FRET, assigned to the L_o phase (**E**). The missing high FRET component was not observed due to high partitioning of CTxB-488 to the L_o phase.

Positions of the clusters in phasor plots obtained for different GUV compositions are given in Fig. 4 (see Fig. S4 for entire plots). The most striking is the finding of entirely different decays for three microscopically homogenous compositions **A**, **B**, and **C**. **A** does not contain Sph, no lipid segregation occurs, and FRET accelerates CTxB-488 decay considerably due to a high probability of an acceptor presence in close vicinity of a donor. **B** and **C** are close to the phase separation boundary and the occurrence of nanodomains is therefore expected. In the domain, the donor molecule is separated from the acceptor so that the molecule either cannot transfer its energy to an acceptor if the domains are much greater than the Förster radius, or it transfers the energy with lower average efficiency when size of the domains is comparable to the Förster radius. Fig. 4 shows that the composition **B** exhibits reduced FRET already at a low dose of CTxB-488, which is even more pronounced at the composition **C**.

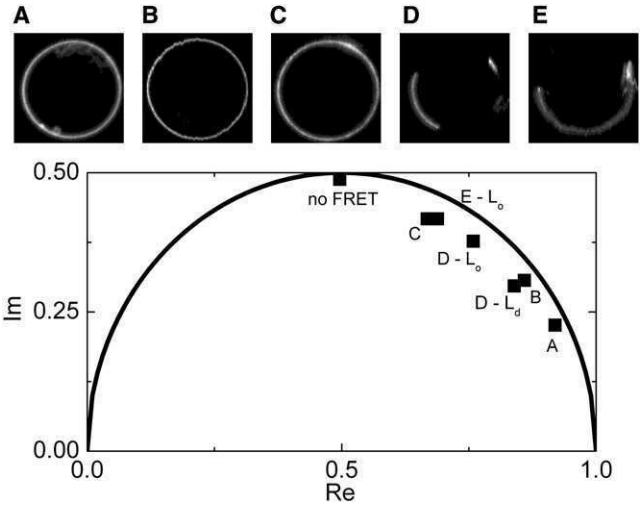

FIGURE 4 FLIM-FRET phasor diagram depicting peak positions of the two-dimensional histogram of transformed donor fluorescence decay functions measured at every pixel of the GUV image. Upper part: fluorescence intensity images of CTxB-488 (*donor*) stained GUVs at different lipid compositions. GUVs are colabeled with DiD (*acceptor*). For **D**, two clusters appeared in the phasor diagram, corresponding to the L_o and L_d phase. The circular line depicts positions of monoexponential decays and position of the acceptor free decay, i.e., no FRET, is marked.

GUVs consisting of compositions **A**, **B**, and **C** were further treated with an excess of nonlabeled CTxB and the FLIM image of the same liposome was taken again. For compositions **A** and **C**, no change occurred, whereas in the case of **B**, addition of cross-linker surplus led to further reduction of FRET (**B**′). This suggests that in the case of the mixture **C**, domains were already well established at low concentration of CTxB-488, whereas composition **B** required more cross-linker to enhance the effect (see Fig. 5). As noted previously, we performed the same experiments with a different FRET pair (perylene-DiD), which also confirms lipid clustering in **C** before cross-linker addition (Fig.S5).

Size determination of nanodomains by MC simulations of FLIM-FRET data

Having proved that the existence of nanodomains can be visualized by FRET, decay functions assigned to compositions **A**, **B**, **B**′, and **C** were further analyzed. We have shown

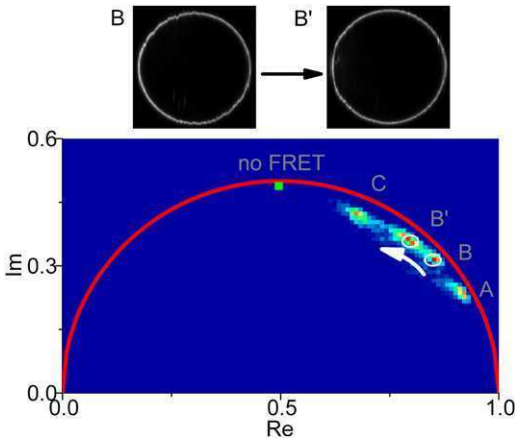

FIGURE 5 FLIM-FRET phasor diagram displaying shift of the CTxB-488 decay functions toward lower FRET when excess of a nonlabeled cross-linker is added. Upper part: CTxB-488 intensity images of the investigated GUV before and after adding of nonlabeled CTxB. No resolvable phase separation occurs.

in our previous work that the FRET pair we used here can reveal formation of domains that are smaller than 20 nm (23). Composition **A** corresponds to the situation of randomly distributed donors and acceptors in a lipid bilayer. The time-resolved energy transfer can be analyzed according to the model that was analytically derived by Baumann and Fayer (B-F model) (21). Details of the model are given in the Supporting Material. By fitting the model to the donor decay function, the concentration of the acceptor molecules was obtained as a readout parameter and kept constant also in the further analysis.

Distribution constants of the donor (K_D) and the acceptor (K_A), input parameters required for MC simulations of domain-containing membranes, were estimated from mean pixel intensities of donor and acceptor in the phase separated GUVs corresponding to the lipid mixture **D**. The values are in good agreement with the literature (18).

The donor decays corresponding to situation **B** and **B′** (see Fig. 5), i.e., the situation with a low amount of CTxB-488 and with an excess of nonlabeled CTxB, respectively, and situation **C** (see Fig. 5) were modeled by means of MC simulations (24–26) (see the Supporting Material for details) and compared to the experimental decay curves. The number of fitting parameters was reduced to R, the domain radius, and Ar, the area domains take up in the bilayer. As shown in Fig. 6, the optimization routine provides a pronounced minimum for **B** when $R = 5$–5.4 nm and $Ar = 6$–9% and for **B′** when $R = 8$ nm and $Ar = 6\%$. For situation **C** $R = 24$ nm and $Ar = 3\%$. The calculated area for the composition **C** is much smaller than would be expected upon the analysis of the phase diagram. This might be caused by several facts. First of all, the distribution coefficients are not known precisely and as shown further, the K_D value has a nonnegligible impact on the calculated fractions, but not on the domain radius. Furthermore, the phase diagram presented in Fig. 1 has more or less an illustrative character because it applies for a system similar to ours but with few alterations as already discussed. Unfortunately, these alterations will have the greatest impact in the discussed boundary region.

Because both $K_D = 6 \pm 3$ and $K_A = 0.004 \pm 0.002$ have been estimated with a certain error and since they are expected to moderately change across the tie-line field (Fig. 1), it is reasonable to test how the values of distribution constants influence the positions of the minima. We have realized that domain radii stay almost unaffected, whereas the domain area reflects the changes of K_D. In the case of **B′** for example, reduction of K_D from 6 to 3 leads to $R = 8$ nm and $Ar = 12\%$, whereas an increase of K_D to 9 leads to $R = 7$ nm and $Ar = 5\%$. It is not surprising that change of K_A in the range $\pm$ 0.002 does not affect the shape of the decay because K_A is so low that practically all acceptors are still excluded from the domains. Similarly, we tried to vary concentration of the acceptor molecules (which was

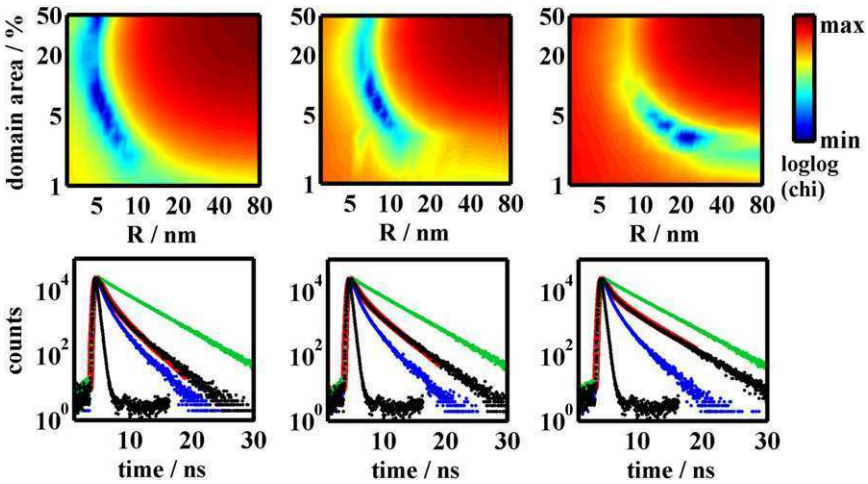

FIGURE 6 Upper part: Best fitting χ^2-square parameter as a function of the domain radius and the area domains take up in the bilayer. A minimum is found at $R = 5$ nm and domain area 9% for composition **B** (*on the left*), $R = 8$ nm and domain area 6% for composition **B′** (*in the middle*), and at $R = 24$ nm and domain area 3% for the composition **C** (*on the right*). Lower part: Displayed time resolved fluorescence decays of CTxB-488 serving as the donor (*D*) representing the bilayer containing i), *D* only (*green line*); ii), *D* and *A* (*acceptors*) distributed between domain and nondomain regions (*black line*) and iii), *D* and *A*, where both *D* and *A* are uniformly distributed in the bilayer without any domains (*blue line*). The red line almost coinciding with the black line is the best fit calculated by means of MC simulations. Instrument response function is displayed too. Figures in the lower part correspond to those in the upper part.

estimated by the B-F model) in the range ± 10% for **B′**. The impact on both *R* and *Ar* was negligible. Therefore, it can be concluded that the domain radius increases in the order 5 → 8 → 24 nm when going from **B** over **B′** to **C**, although the area the domains occupy does not significantly change.

It is worth noticing that the radius of pentameric CTxB is around 4.5 nm (27), which suggests that in situation **B**, a domain is formed at most by a single pentamer unit (domain radius ~5 nm). Because the FRET contribution is lowered in case **B** compared to the homogenous composition **A**, the pentameric unit is probably encircled by a raft-lipid collar separating donor and acceptor molecules and forming a disk-like domain with a protein-cross-linked GM1 core and Sph-enriched shell.

The domain radius (~8 nm) in the case of **B′** suggests that maximum 2–3 pentameric CTxB units form the enlarged domain. Because both the FCS and FRET demonstrations of domains show dependency on the cross-linker load, coalescence of two to three units implicates the domain formation. Once a CTxB molecule would separate from the cluster, the enlarged domain would be perturbed and inevitably disappear. Therefore, the domains in case **B′** are probably transient with the lifetime corresponding roughly to the residential time obtained from the z-scan FCS (30 ms). Because it is the cross-linker concentration that makes domains detectable in our experiments, we hypothesize that domain is formed upon collision between two and three CTxB disks. This implies that they can be observed if the collision rate is sufficient. We have calculated theoretical collision rates and the mean times between two collisions for the 5 nm disks diffusing freely in the planar bilayer (28) (see Table S3) and realized that while in the composition **B** highly loaded with CTxB-647, the mean intercollision time is around 31 ms, at low cross-linker load, this time increases to almost 1 s. At high cross-linker load, CTxB-GM1 complexes spend half of their time trapped in the domains, whereas at low load, this time is in the range of only a few percents and therefore the domains were not detected. Similar confinement times indicating trapped molecular diffusion and estimated raft sizes (i.e., <20 nm) were also reported in the STED-FCS study of glycosylphosphatidylinositol-anchored proteins (9), which might indicate the general character of the described phenomenon.

CONCLUSION

In this work, a detailed dynamic and structural study of a cross-linker-triggered formation of nanodomains is presented. We show evidence of such structures in the model membranes at lipid compositions closely approaching the optically resolvable phase separation boundary. It has to be noted that the phase separation boundary has been commonly determined (29) based on observation of two distinct phases in model membranes by means of optical microscopy. Recent work of Heberle et al. (30) predicts optically nonresolvable phase coexistence in ternary lipid mixtures even in the putative one-phase region.

Here, fluorescence dynamic experiments carried out in two lipid membrane compositions (**B** and **C**) slightly differing in the Sph content reveal two different types of subwavelength domains. Although the FRET analysis predicts three times larger domain radius in the liposomes composed of mixture **C** compared to **B**, apparent diffusion of the cross-linker molecules is approximately by factor three slower in the composition **B** (compared to **C**) and follows a different diffusion law. Because in **B**, the diffusion character changes at an increased cross-linker load, we propose that these nanodomains are transiently constituted upon collision of CTxB-GM1 complexes. In **B** the domain formation is therefore initiated exclusively by the cross-linker and consequently stabilized by Sph. In contrast, our data indicate that small lipid domains are already formed in the composition **C** before the cross-linker is added and their existence is attributed mainly to lipid-lipid interactions. We hypothesize that the addition of the cross-linker induces further coalescence into larger membrane assemblies that eventually leads to microscopic phase separation (10).

It has to be pointed out that the noncytosolic leaflet of the plasma membrane contains much more cholesterol (up to 50%) than used in this study (31). To get an idea whether the domains are still formed under biologically more relevant conditions, we explored the diffusion behavior of labeled CTxB also along the 35% cholesterol line (data not shown) and observed the very same slowing down of the apparent diffusion when approaching the phase separation boundary (at 29% of Sph). This suggests that the transiently forming domains causing the trapped diffusion may be also preserved at cholesterol contents relevant for plasma membranes. The approaches used in this study are however applicable generally, i.e., also in the living cells (see (32) for FCS-based diffusion laws).

CTxB is not only an important model of a pentavalent lipid cross-linker, but it also significantly responses to the imposed membrane curvature by strong enhancing curvature-mediated lipid sorting close to the phase separation boundary (33,34). It is believed that the reason for this behavior arises from the ability of CTxB pentamers to form clusters bending inward, which are also responsible for the cellular uptake of the toxin (35). Our results show that close to the boundary region, the CTxB-GM1 pentamers are probably enriched in Sph forming rigid disk-like (perhaps even negatively curved) platforms that would be expelled from membranes of highly positive curvature. The CTxB-induced sorting enhancement could therefore stem from association of the raft lipids with the platforms.

CTxB together with other bacterial toxins such as Shiga toxin and some viruses from the polyoma family such as simian virus 40 are involved in glycosphingolipid receptor clustering, which induces membrane curvature responsible

for caveolin-independent endocytoses. It has been shown that the membrane invaginations responsible for the toxin uptake are subjected to the overall membrane tension, bending rigidity in the receptor-enriched domains related to the ability to cause the spontaneous curvature as well as the L_o of the domains responsible for the aggregation of the pentameric clusters. Therefore, understanding of the nanodomain formation on the level of a few single pentamers may also cast light on the molecular mechanism and dynamics of the previously mentioned phenomena.

SUPPORTING MATERIAL

Details of the data analysis, five figures, three tables, and references (22,25,28,32,36–38) are available at http://www.biophysj.org/biophysj/supplemental/S0006-3495(12)00395-5.

M.Š. acknowledges support of the Grant Agency of Charles University (grant No. 3130/2011), Ministry of Education of the Czech Republic for a scholarship, and to specific University Research Project (grant No. 33779266), R.M., M.H., J.H., M.C., and R.Š. acknowledge support of the Czech Science Foundation (ESF EUROMEMBRANE project MEM/09/E006, P305/11/0459, and P208/10/1090). M.C. wishes to further acknowledge a Purkyne Fellowship award.

REFERENCES

1. Grakoui, A., S. K. Bromley, …, M. L. Dustin. 1999. The immunological synapse: a molecular machine controlling T cell activation. *Science.* 285:221–227.
2. Schamel, W. W. A., I. Arechaga, …, B. Alarcón. 2005. Coexistence of multivalent and monovalent TCRs explains high sensitivity and wide range of response. *J. Exp. Med.* 202:493–503.
3. Holowka, D., and B. Baird. 2001. Fc(epsilon)RI as a paradigm for a lipid raft-dependent receptor in hematopoietic cells. *Semin. Immunol.* 13:99–105.
4. Janes, P. W., S. C. Ley, and A. I. Magee. 1999. Aggregation of lipid rafts accompanies signaling via the T cell antigen receptor. *J. Cell Biol.* 147:447–461.
5. Stefanová, I., V. Horejsí, …, H. Stockinger. 1991. GPI-anchored cell-surface molecules complexed to protein tyrosine kinases. *Science.* 254:1016–1019.
6. Dietrich, C., Z. N. Volovyk, …, K. Jacobson. 2001. Partitioning of Thy-1, GM1, and cross-linked phospholipid analogs into lipid rafts reconstituted in supported model membrane monolayers. *Proc. Natl. Acad. Sci. USA.* 98:10642–10647.
7. Hammond, A. T., F. A. Heberle, …, G. W. Feigenson. 2005. Cross-linking a lipid raft component triggers liquid ordered-liquid disordered phase separation in model plasma membranes. *Proc. Natl. Acad. Sci. USA.* 102:6320–6325.
8. van Zanten, T. S., J. Gómez, …, M. F. Garcia-Parajo. 2010. Direct mapping of nanoscale compositional connectivity on intact cell membranes. *Proc. Natl. Acad. Sci. USA.* 107:15437–15442.
9. Eggeling, C., C. Ringemann, …, S. W. Hell. 2009. Direct observation of the nanoscale dynamics of membrane lipids in a living cell. *Nature.* 457:1159–1162.
10. Lingwood, D., J. Ries, …, K. Simons. 2008. Plasma membranes are poised for activation of raft phase coalescence at physiological temperature. *Proc. Natl. Acad. Sci. USA.* 105:10005–10010.
11. Brown, D. A., and E. London. 2000. Structure and function of sphingolipid- and cholesterol-rich membrane rafts. *J. Biol. Chem.* 275:17221–17224.
12. de Almeida, R. F. M., L. M. S. Loura, …, M. Prieto. 2005. Lipid rafts have different sizes depending on membrane composition: a time-resolved fluorescence resonance energy transfer study. *J. Mol. Biol.* 346:1109–1120.
13. Benda, A., M. Benes, …, M. Hof. 2003. How to determine diffusion coefficients in planar phospholipid systems by confocal fluorescence correlation spectroscopy. *Langmuir.* 19:4120–4126.
14. Wawrezinieck, L., H. Rigneault, …, P. F. Lenne. 2005. Fluorescence correlation spectroscopy diffusion laws to probe the submicron cell membrane organization. *Biophys. J.* 89:4029–4042.
15. Akashi, K., H. Miyata, …, K. Kinosita, Jr. 1996. Preparation of giant liposomes in physiological conditions and their characterization under an optical microscope. *Biophys. J.* 71:3242–3250.
16. Smith, A. K., and J. H. Freed. 2009. Determination of tie-line fields for coexisting lipid phases: an ESR study. *J. Phys. Chem. B.* 113:3957–3971.
17. Farkas, E. R., and W. W. Webb. 2010. Precise and millidegree stable temperature control for fluorescence imaging: application to phase transitions in lipid membranes. *Rev. Sci. Instrum.* 81:093704.
18. Chiantia, S., J. Ries, …, P. Schwille. 2006. Combined AFM and two-focus SFCS study of raft-exhibiting model membranes. *Chem. Phys. Chem.* 7:2409–2418.
19. Stefl, M., A. Kułakowska, and M. Hof. 2009. Simultaneous characterization of lateral lipid and prothrombin diffusion coefficients by z-scan fluorescence correlation spectroscopy. *Biophys. J.* 97:L01–L03.
20. Wenger, J., F. Conchonaud, …, P. F. Lenne. 2007. Diffusion analysis within single nanometric apertures reveals the ultrafine cell membrane organization. *Biophys. J.* 92:913–919.
21. Baumann, J., and M. D. Fayer. 1986. Excitation transfer in disordered two-dimensional and anisotropic 3-dimensional systems - effects of spatial geometry on time-resolved observables. *J. Chem. Phys.* 85:4087–4107.
22. Digman, M. A., V. R. Caiolfa, …, E. Gratton. 2008. The phasor approach to fluorescence lifetime imaging analysis. *Biophys. J.* 94:L14–L16.
23. Sachl, R., J. Humpolíčková, …, M. Hof. 2011. Limitations of electronic energy transfer in the determination of lipid nanodomain sizes. *Biophys. J.* 101:L60–L62.
24. Engstrom, S., M. Lindberg, and L. B. A. Johansson. 1988. Monte-Carlo simulations of electronic-energy transfer in 3-dimensional systems - a comparison with analytical theories. *J. Chem. Phys.* 89:204–213.
25. Johansson, L. B. A., S. Engstrom, and M. Lindberg. 1992. Electronic energy transfer in anisotropic systems. 3. Monte Carlo simulations of energy migration in membranes. *J. Chem. Phys.* 96:3844–3856.
26. Šachl, R., I. Mikhalyov, …, L. B. Johansson. 2011. Distribution of BODIPY-labelled phosphatidylethanolamines in lipid bilayers exhibiting different curvatures. *Phys. Chem. Chem. Phys.* 13:11694–11701.
27. Dwyer, J. D., and V. A. Bloomfield. 1982. Subunit arrangement of cholera toxin in solution and bound to receptor-containing model membranes. *Biochemistry.* 21:3227–3231.
28. Hardt, S. L. 1979. Rates of diffusion controlled reactions in one, two and three dimensions. *Biophys. Chem.* 10:239–243.
29. Veatch, S. L., and S. L. Keller. 2003. Separation of liquid phases in giant vesicles of ternary mixtures of phospholipids and cholesterol. *Biophys. J.* 85:3074–3083.
30. Heberle, F. A., J. Wu, …, G. W. Feigenson. 2010. Comparison of three ternary lipid bilayer mixtures: FRET and ESR reveal nanodomains. *Biophys. J.* 99:3309–3318.
31. van Meer, G., D. R. Voelker, and G. W. Feigenson. 2008. Membrane lipids: where they are and how they behave. *Nat. Rev. Mol. Cell Biol.* 9:112–124.
32. Humpolícková, J., E. Gielen, …, Y. Engelborghs. 2006. Probing diffusion laws within cellular membranes by Z-scan fluorescence correlation spectroscopy. *Biophys. J.* 91:L23–L25.
33. Tian, A., and T. Baumgart. 2009. Sorting of lipids and proteins in membrane curvature gradients. *Biophys. J.* 96:2676–2688.
34. Sorre, B., A. Callan-Jones, …, P. Bassereau. 2009. Curvature-driven lipid sorting needs proximity to a demixing point and is aided by proteins. *Proc. Natl. Acad. Sci. USA.* 106:5622–5626.

35. Ewers, H., W. Römer, …, L. Johannes. 2010. GM1 structure determines SV40-induced membrane invagination and infection. *Nat. Cell Biol.* 12:11–18.

36. Palmer Iii, A. G., and N. L. Thompson. 1989. Optical spatial intensity profiles for high order autocorrelation in fluorescence spectroscopy. *Appl. Opt.* 28:1214–1220.

37. Bergenstahl, B. A., and P. Stenius. 1987. Phase diagrams of dioleoylphosphatidylcholine with formamide, methylformamide, and dimethylformamide. *J. Phys. Chem.* 91:5944–5948.

38. Margineanu, A., J. I. Hotta, …, J. Hofkens. 2007. Visualization of membrane rafts using a perylene monoimide derivative and fluorescence lifetime imaging. *Biophys. J.* 93:2877–2891.

Dynamics and Size of Cross-Linking-Induced Lipid Nanodomains in Model Membranes

Martin Štefl,[†] Radek Šachl,[†‡] Jana Humpolíčková,[†] Marek Cebecauer,[†] Radek Macháň,[†] Marie Kolářová,[†] Lennart B.-Å. Johansson,[‡] and Martin Hof[†]

[†]Department of Biophysical Chemistry, J. Heyrovsky Institute of Physical Chemistry of the Academy of Sciences of the Czech Republic, Dolejškova, Prague, Czech Republic; and [‡]Department of Chemistry: Biophysical Chemistry, Umeå University, Umeå, Sweden

Supporting Information

Two-color z-scan FCS

Z-scan FCS is a calibration-free FCS method which allows for precise determination of diffusion coefficients in planar systems.[1] The principle of z-scan FCS is based on acquiring individual fluorescence intensity traces at different positions of the planar system (bilayer) with respect to the optical axis (z-axis) of the focal volume. The intensity traces $I(t)$ obtained at every position are individually correlated according to the formula:

$$G(\tau) = \frac{\langle I(t)I(t+\tau)\rangle}{\langle I(t)\rangle^2}, \qquad \text{Eq. 1}$$

where the angle brackets represent temporal averaging. Resulting autocorrelation functions are subsequently fit with suitable model. In our case, we have applied two-dimensional Brownian diffusion model assuming Gaussian point spread function (PSF). The theoretical shape of the autocorrelation function $G(\tau)$ is described by:

$$G(\tau) = 1 + \left[1 - T + Te^{\frac{-\tau}{\tau_T}}\right] \frac{\gamma}{N(1-T)} \frac{1}{1+\frac{\tau}{\tau_D}}, \qquad \text{Eq. 2}$$

where T corresponds to a fraction of fluorophores in the triplet state, τ_T is a parameter characterizing the triplet state transition, γ is a factor accounting for beam geometry ($\gamma = ½$ for 2D), N stands for average number of particles in the illuminated spot and τ_D is the transition time, i.e. the time the molecule needs to pass through the illuminated area. When fitting our data T, τ_T, N, and τ_D were free parameters. Since the triplet fraction is usually small (~ 5 %) if any and τ_T is in μs-time range, these two parameters do not have a significant impact for the fit. Due to Loretzian character[2] of intensity profile in the tightly focus laser beam, the read-out parameters τ_D and N plotted versus the position of the bilayer with respect to the laser focus z follow the equations:

$$\tau_D(z) = \frac{\omega_0^2}{4D}\left(1 + \frac{\lambda^2 (z - z_0)^2}{n^2 \pi^2 \omega_0^4}\right), \qquad \text{Eq. 3}$$

$$N(z) = \pi c_s \omega_0^2 (1 + \frac{\lambda^2 (z - z_0)^2}{n^2 \pi^2 \omega_0^4}), \qquad \text{Eq. 4}$$

where ω_0 is the radius of the waist of the laser focus, λ is excitation wavelength, n stands for refractive index, D is a diffusion coefficient, z_0 is the z-coordinate corresponding to the situation when the bilayer is in the waist of the laser beam, and c_s is planar concentration of diffusing molecules. When fitting the parabolas to the measured τ_D- and N-dependences, D, c_s, and ω_0 are free parameters.

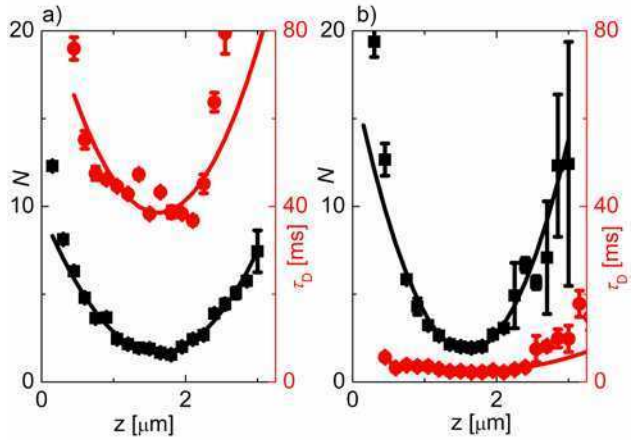

Figure S1. Dependence of the particle number (black) and the mean transition time (red) on the relative position of a bilayer with respect to the optical axis for CTxB-647 (a) and BDP-DHPE (b) measured in the upper GUV membrane composed of lipid mixture **B** at high crosslinker load.

A typical example of the two color z-scan experiment is depicted in Fig. S1. In this particular example, intensity fluctuations of CTxB-647 (high loaded composition **B**) and BDP-DHPE were simultaneously acquired and processed as described above. Particle number and the transition time dependences for both the dyes show the expected parabolic behavior. When fitting the parabolas with models given by Eg. 3 and Eq. 4, the diffusion coefficient (or apparent diffusion coefficient if the diffusion is not free) and surface concentration can be withdrawn.

Diffusion law and its application in z-scan FCS

Wawrezinieck *et al* studied the dependence of the mean transition time through the

illuminated area on the area size.[3] Due to the fact that in optical microscopy the minimum size of the illuminated area is diffraction limited and that the expected diffusion barriers such as rafts or cytoskeleton meshwork are much smaller than the limit, Monte Carlo simulations were employed. The particular type of the barriers was generated and the apparent transition times simulated as a function of the area size. The dependence is linear if the structures of interest are much smaller compared to the illuminated spot and follow the so called "diffusion law":

$$\tau_D^{app} = t_0 + \frac{\omega^2}{4D_{eff}}. \qquad \text{Eq. 5}$$

τ_D^{app} is the time a molecule passes through the detection area, ω stands for the spot radius, D_{eff} is an effective diffusion coefficient which bears the information about the barrier-free diffusion coefficient, probability of crossing the barriers and the density of membrane structures (in the case of isolated domains). The intercept t_0 is equal to zero for homogeneous membranes, negative in the case of meshwork, and positive in presence of isolated domains in the membrane. With knowledge of the diffusion coefficient in a homogenous membrane D_{free} and D_{eff} determined from Eq. 5, the time based partition coefficient α (fraction of time a molecule spends in the domains) can be calculated:

$$D_{eff} = (1-\alpha)D_{free}. \qquad \text{Eq. 6}$$

The intercept t_0 is related to the confinement time, i.e. the time a molecule is trapped in the domain, τ_{conf} and the time the molecule diffuses from the center of the domain to its boundary τ_D^{domain}:

$$t_0 = 2\alpha(\tau_{conf} - \tau_D^{domain}). \qquad \text{Eq. 7}$$

Usually, it is assumed that $\tau_{conf} \gg \tau_D^{domain}$.

Since the illuminated spot size is being inherently changed during the z-scan, and the number of particles serves as a measure of the size, the diffusion law can be constructed from the z-scan FCS data as introduced by Humpolíčková *et al*.[4] Eq. 6 is extended as follows:

$$\tau_D^{app} = t_0 + \frac{\omega_0^2}{4D_{eff}} \frac{N}{N_0}. \qquad \text{Eq. 8}$$

Fig. 3 in the manuscript shows dependences of the CTxB-647/BDP-DHPE transition time on the N/N_0 ratio for selected GUVs at investigated compositions. Table S1 gives values of intercepts and slopes of the given dependences obtained by linear fitting.

Species/Composition	Intercept	Error	Slope	Error
	[ms]	[ms]	[ms]	[ms]
BDP-DHPE/**B**(high load)	-0.9	0.6	3.1	0.5
CTxB-647/**A**	0.6	0.9	5.0	0.8
CTxB-647/**B**(low load)	2.5	2.8	3.5	2.5
CTxB-647/**B**(high load)	54.9	7.3	26.1	4.9
CTxB-647/**C**	-0.6	2.8	13.2	2.3

Table S1. Intercepts and slopes for the linear $\tau_D^{app} \sim N/N_0$ dependences given in Fig. 3.

Relative brightness of CTxB-647 labeled clusters and two-color cross-correlation experiments

To better understand the source of long transition times observed for the highly loaded **B**-composed GUVs, relative brightness of CTxB-647 clusters, i.e. number of photons generated by a single cluster per second, was estimated for every concentration of the crosslinker. We assume that changes in relative brightness would roughly correspond to the clustering degree, i.e. refer to the average number of CTxB- 647-GM1 pentamers in a nanodomain. The results are shown in Table S2.

composition **B**, CTxB-647 load	low	medium	high
relative brightness [kHz/molecule]	2.2	3.1	5.0
SD	0.5	0.7	1.7
n	4	4	4
relative average aggregation number	1.0	1.4	2.2

Table S2. Relative brightness of CTxB-647 clusters obtained from z-scan FCS experiments performed on **B**-composed liposomes for different crosslinker concentrations. *SD* stands for a standard deviation, and *n* is a number of z-scans acquired.

The relative brightness β was calculated as follows: $\beta = counts/N$, where "counts" is the average countrate in the red detection channel arising upon excitation with the red laser, N is a number of particles obtained from amplitude of ACF. The relative brightness changes with the position of the bilayer with respect to the focused beam giving a distinct maximum when the bilayer is in the focus. The maximal values are those used in Table S2.

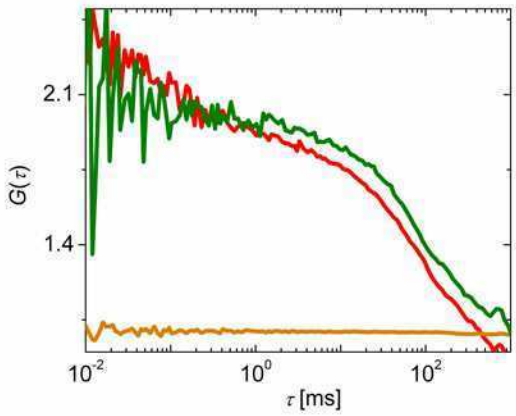

Figure S2. ACFs for CTxB-647 (red curve) and CTxB-488 (green curve) acquired in two-color z-scan FCS experiment performed in upper membrane of **B**-composed GUVs. Orange curve is a cross-correlation function between the red and green dignal. The curves shown correspond to the situation when membrane is in the laser focus.

In order to understand whether the assemblies revealed in the given brightness analyses are solid patches coupling the motion of individual CTxB-647 particles together, liposomes were treated with an equimolar mixture of CTxB-647 and CTxB-488 and the cross-correlation between the red and green signal was investigated (see Fig. S2). The fact that no cross-correlation appears indicates uncoupled motion of CTxB-GM1

complexes, which supports our assumption that the nanodomains result from lipid-lipid interactions rather than mutual interactions between the crosslinker molecules.

Phasor approach in FLIM-FRET analysis

Phasor plot is a graphical, non-fitting approach for visualization of different fluorescence decay functions in FLIM images.[5] In our experiments, phasor plots were used to characterize changes in donor decays in a FRET experiment. Fig. S3 shows an example of a GUV formed by lipid mixture **D**. This example is used to demonstrate the data treatment applied to our FLIM-FRET data.

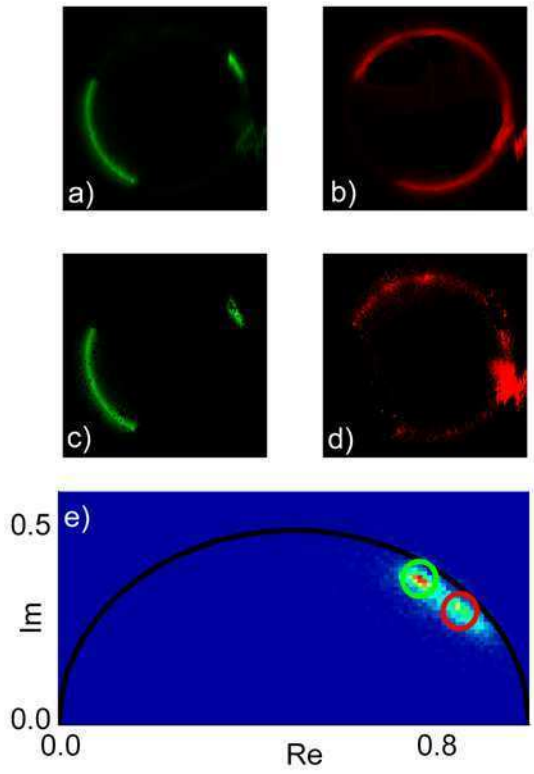

Figure S3. a) and b): intensity images of CTxB-488 and DiD measured for a GUV formed by the lipid mixture **D**. c) and d) depicts pixels corresponding to the different decay functions of CTxB-488 observed in the phasor plot (e).

For the FRET experiments, GUVs were labeled with DiD, acceptor molecules, residing in the L_d phase. The donor molecule, CTxB-488, binds to gangliosides GM1

preferentially occupying the L_o phase. Acquisition of every image is done using two-color, pulse-interleaved excitation (470 and 640 nm) and the fluorescence signal is split on two detectors, therefore simultaneously measured intensity images of the donor and the acceptor can be reconstructed (Fig. S3a and S3b). At every pixel of the image, the decay histogram is acquired using time-correlated single photon counting (TCSPC). The resulting 3D matrix is converted to the phasor diagram in the following way:

i) For every pixel, the phasor plot coordinates are calculated using formula:

$$\begin{bmatrix} \mathrm{Re} \\ \mathrm{Im} \end{bmatrix} = \frac{1}{\sum_{i=1}^{L} I_i} \begin{bmatrix} \sum_{i=1}^{L} I_i \cos\frac{2\pi n}{L}(i - i_0) \\ \sum_{i=1}^{L} I_i \sin\frac{2\pi n}{L}(i - i_0) \end{bmatrix}, \qquad \text{Eq. 9}$$

I_i is fluorescence intensity in the i-th TCSPC channel, L stands for the number of TCSPC channels, n is an arbitrarily chosen integer (here $n = 4$) corresponding to the frequency in the Fourier space, i_0 is a channel position of the decay rising edge. i_0 is commonly determined by measuring TCSPC histogram of a single exponential dye (fluorescein). Its value is being varied as long as the position of the single exponential decay in the phasor diagram lies on the universal circle (black line in Fig. S3e).

ii) 2D histogram of the phasor plot coordinates is constructed (Fig. S3e). Clusters in the phasor plot correspond to various spatially resolvable decay functions. The two clusters in Fig.S3e are assigned to the pixels with higher FRET (red circle in Fig. S3e and Fig. S3d) and the lower FRET contribution (green circle in Fig. S3e and Fig. S3c). Figure S3 proves that the lower FRET is observed in the L_o phase while higher contribution of energy transfer corresponds to the L_d phase. If the phases are not spatially resolvable, every pixel contains both low and high FRET contributions, which results in a single cluster in the phasor plot.

Fig. 4 in the manuscript gives only peak positions of individual lifetime clusters, the entire phasor plots for CTxB-488 donor lifetime in GUVs are given in Fig. S4:

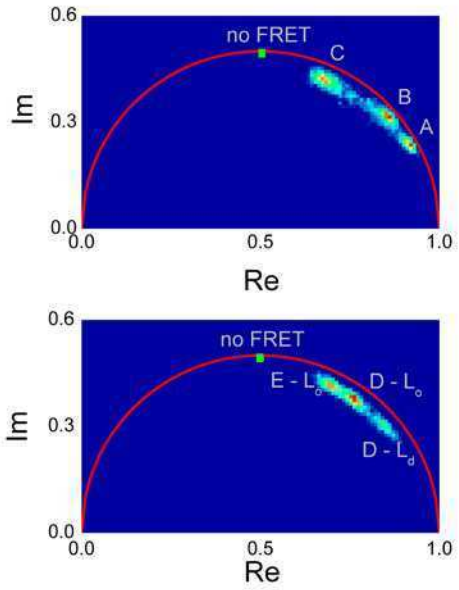

Figure S4. Positions of CTxB-488 donor decay clusters in the phasor plot for GUVs composed of lipid mixture A to C (upper part), and D to E (lower part). Position of a decay corresponding to no FRET is marked. No FRET decay was measured in solution containing CTxB-488.

Baumann-Fayer model

Baumann-Fayer[6] model accounts for energy transfer/migration within one leaflet of the bilayer in a two-dimensional geometry, or between two parallel planes separated from each other at distance *d*. According to the model, the energy transfer contributes to the fluorescence decay $F(t)$ of a donor according to:

$$F(t) = G^s(t)\sum_i \alpha_i \exp\left(-\frac{t}{\tau_i}\right) \qquad \text{Eq. 10}$$

In Eq. 10, α_i and τ_i describe the donor fluorescence in the absence of acceptors. The function $G^s(t)$ stands for the probability that a donor initially excited at $t = 0$ is still excited at time t later. In a lipid bilayer where both D and A reside at the interface of the bilayer excited energy can be transferred to either A localized in the same leaflet, this

process is described by the intra-layer probability $G^{s}_{intra}(t)$, or to an acceptor localized in the opposite leaflet. This event is then described by an inter-layer probability $G^{s}_{inter}(t)$. The total probability $G^{s}(t)$ is given by the joint probability $G^{s}(t) = G^{s}_{intra}(t)G^{s}_{inter}(t)$. For isotropically oriented donor and acceptors which reorient fast as compared to the rate of energy transfer (*i.e.* the dynamic limit condition), $G^{s}_{intra}(t)$ is given by

$$\ln G^{s}_{intra}(t) = -C_2 \Gamma(2/3)(t/\tau)^{1/3} \qquad \text{Eq. 11}$$

Here C_2 is a so called reduced concentration corresponding to the average number of acceptors within a circle limited by the Förster radius of the donor (R_0) and Γ is the gamma function. The probability of inter-leaflet energy transfer is given by

$$\ln G^{s}_{inter}(\mu) = \frac{C_2}{3}(d/R_0)^2 (2\mu/3)^{1/3} \int_0^{2/3\mu} (1 - e^{-s}) s^{-4/3} ds \qquad \text{Eq. 12}$$

In Eq. 12, d is the distance between the leaflets where the chromophores reside, $\mu = 3t(R_0/d)^6/2\tau$ and $s = 2\mu\cos^6\theta_r/3$, where θ_r denotes the angle between the bilayer normal and the vector $\boldsymbol{r}$ which connects the locations of the donor and acceptor dipoles.

Monte Carlo simulations

Analytical equations describing FRET exist for a limited number of basic geometries and are quite complex and not easy to derive. Therefore it is convenient to apply Monte Carlo simulations, which successively mimic various random processes. Here we have used this technique to simulate FRET in a lipid bilayer containing circular nanodomains. The following steps have been carried out: (i) A certain number of domains corresponding to a pre-defined area occupied by the domains was generated. (ii) Donors and acceptors were distributed with a certain probability of being localized within and outside the domains. The distribution is described by an equilibrium constant ($K_{D,A}$ = [donors (acceptors) within]/[donors (acceptors) outside]). (iii) A donor was randomly excited and assumed to transfer its excitation energy to an acceptor, which was localized either in the same plane or in the opposite leaflet. The time Δt_i elapsed from the excitation to the transfer event depends on the overall energy transfer rate Ω_i according to:

$$\Delta t_i = -\frac{\ln \alpha}{\Omega_i}, \qquad \text{Eq. 13}$$

where α denotes a random number between 0-1. The total energy transfer rate is calculated as a sum of energy transfer rates from the excited donor i to all acceptors. Acceptors that are beyond the cut-off distance $10\,R_0$ are included via the continuum approach (periodic boundary):

$$\Omega_i = \sum_j \frac{3}{2}\kappa_{ij}^2 \left(\frac{R_0}{R_{ij}}\right)^6 \tau_D^{-1} + C_2 \left(\frac{R_0}{R_C}\right)^4 \tau_D^{-1}, \qquad \text{Eq. 14}$$

Here j goes from 1 to the number of acceptors found within the cut-off distance R_C. R_{ij} is the distance between the i-th donor and j-th acceptor, R_0 the Förster radius, τ_D lifetime of the donor in the absence of any acceptor and κ_{ij}^2 is the so called kappa factor. The second term in Eq. 14 accounts for rates between the excited donor and the continuum of acceptors exceeding the donor-acceptor distance R_C distributed over two parallel planes.[7] Due to 1/6 power dependence of FRET rate efficiency on R and rather large size of the replicated box ($10\,R_0 \times 10\,R_0$) this term constitutes negligibly to Ω. New configurations were generated approximately 3000 times and each generated configuration set was 100 times excited and used in the calculation step (iii). The outcome of the simulation is the $G(t)$ function , which is related to the fluorescence decay via B-F model (Eq. 10). The generated decay was then fitted to the experimental one by changing the variable input parameters, the domain radius and the area occupied by the domains. The remaining parameters were fixed: R_0 = 5.4 nm, K_D, K_A, reduced surface concentration C_2 obtained from the B-F model, parameters A_i and τ_i of the donor decay in the absence of acceptors and the bilayer thickness d = 38 Å.[8]

Perylene-to-DiD energy transfer and changes in perylene lifetime

To support our hypothesis that while in the composition **B**, the domain formation is initiated by the crosslinker, in the composition **C**, the domains are formed already prior crosslinker addition, we have measured lifetime of perylene (donor) in GUVs formed of the lipid mixture **B** and **C** in the presence of DiD (acceptor) before and after addition of the non-labeled crosslinker (CTxB). The distribution constant K of perylene between the

liquid-ordered and liquid-disordered phase was estimated to be around 0.8 (intensity image of phase separated GUV formed of the mixture **D** was analysed, K was calculated as: $K = \left(I(\mathrm{L_o})\tau(\mathrm{L_d})\right)/\left(I(\mathrm{L_d})\tau(\mathrm{L_o})\right)$, where I and τ are average pixel intensities and lifetimes of perylene, respectively, in the given phase). Additionally, perylene has a longer lifetime in the L_o phase (7-8 ns) than in the L_d phase (5.5-6 ns). Thus, when nanodomains are formed, certain perylene fraction becomes separated from the acceptor, which results in longer average lifetime first, due to lower FRET and second, due to occupation of the L_o phase. Changes in fluorescence decay profiles are depicted in Fig. S5.

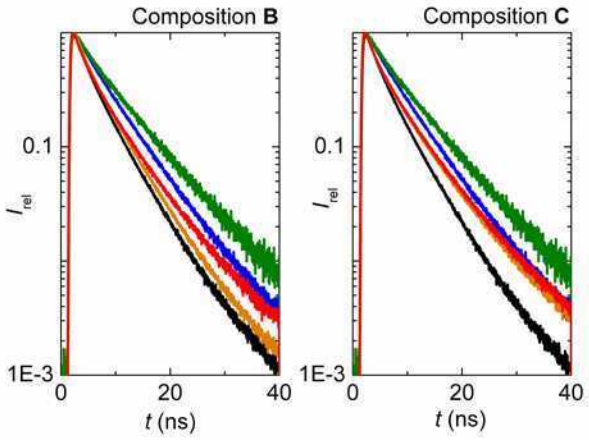

Fig. S5. Fluorescence decay profile of perylene in GUVs formed of lipid mixture **B** (left) and **C** (right) before (orange) and after (red) addition of CTxB. For comparison, perylene decays in the composition **A** without (blue) and with (black) acceptor are given as well as the perylene decay in the L_o phase of the **D** composed GUVs (green). The experimental conditions were the same as were used for the CTxB-488-to-DiD FRET measurements except from the fact that no labeled CTxB was added and instead perylene was present in label-to-lipid ratio 1:200.

The figure shows that in the liposomes composed of the mixture **B**, the donor decay resembles the decay in the composition **A** when both donors and acceptor are homogeneously distributed in the Sph- free membrane. When CTxB is added, perylene decay starts to deviate towards longer lifetimes typical for the L_o phase. In contrast, in

the composition **C**, the longer decay component is present already before adding of the crosslinker and after its addition almost no decay change was detected.

We are aware of the fact that the decay of perylene is subjected not only to presence of FRET and phase it resides, but it also reflects lipid composition and cholesterol content. In addition, it tends to dimer/excimer formation that may cause additional energy transfers.[9] Therefore, in this work, we did not apply the MC simulations as we did in the case of CTxB-488-to-DiD FRET and restrict ourselves to qualitative data interpretation.

Calculation of collision rates

In order to explain the crosslinker concentration dependence of the diffusion characteristics observed for the **B** composed membranes, we propose the following model: at low CTxB-647 load, gangliosides GM1 are pentamerized, forming a sphingomyelin-stabilized disks that diffuse freely with a diffusion coefficient $D = 2.6$ $\mu m^2 s^{-1}$, which corresponds to the value of the mean transition time given in Table 2. These disks diffuse freely only until they collide with one another. When the collision occurs, local concentration of sphingomyelin increases favoring transient formation of a larger domain. Lifetime of the domain would then correspond to the confinement time of around 30 ms given in the manuscript. Fraction of time that the disks spend diffusing freely and trapped in the domain is given by the ratio between the confinement time and the average inter-collision time.

To calculate the collision frequency f and the mean time between two collisions, model proposed by Hardt[10] was applied:

$$f = 2\pi N_{av} c^2 D \frac{1}{\ln\left[\left(\pi N_{av} c\right)^{-1/2} \Big/ a \right]}, \qquad \text{Eq. 15}$$

where N_{av} is Avogadro constant, a stays for an encounter radius, which is assumed to be the double of the disk radius (i.e. 10 nm), and c is surface concentration of the disks. The concentration was obtained from the z-scan FCS experiment and the parabolic dependence of the number of particles on the membrane position (Eq. 4). The collision rates and the inter-collision times for the CTxB-647 low and high loaded membrane are

given in Table S3.

	N	*c*	*f*	number of collisions in focus	mean intercollision time
		[mol/m^2]	[mol/m^{2}s^{-1}]	[s^{-1}]	[ms]
B-low load	0.2	1.7E-12	7.0E-12	0.8	778
B-high load	4	3.4E-11	4.5E-09	527.1	31

Table S3. Theoretical collision parameters for CTxB-647-crosslinked GM1 in the membrane composed of lipid mixture **B**.

The observed concentration dependence of the diffusion law might result from the fact that at high crosslinker concentration, the protein-lipid disks collide more frequently and thus spend considerably longer time trapped in the domains than in the low concentration case.

References

(1) Benda, A.; Benes, M.; Marecek, V.; Lhotsky, A.; Hermens, W. T.; Hof, M. *Langmuir* **2003**, *19*, 4120-4126.

(2) Palmer, A. G.; Thompson, N. L. *Appl Optics* **1989**, *28*, 1214-1220.

(3) Wawrezinieck, L.; Rigneault, H.; Marguet, D.; Lenne, P. F. *Biophys J* **2005**, *89*, 4029-4042.

(4) Humpolickova, J.; Gielen, E.; Benda, A.; Fagulova, V.; Vercammen, J.; Vandeven, M.; Hof, M.; Ameloot, M.; Engelborghs, Y. *Biophys J* **2006**, *91*, L23-L25.

(5) Digman, M. A.; Caiolfa, V. R.; Zamai, M.; Gratton, E. *Biophys J* **2008**, *94*, L14-L16.

(6) Baumann, J.; Fayer, M. D. *J Chem Phys* **1986**, *85*, 4087-4107.

(7) Johansson, L. B. A.; Engstrom, S.; Lindberg, M. *J Chem Phys* **1992**, *96*, 3844-3856.

(8) Bergenstahl, B. A.; Stenius, P. *J Phys Chem* **1987**, *91*, 5944-5948.

(9) Margineanu, A., J. I. Hotta, R. A. L. Vallee, M. Van der Auweraer, M. Ameloot, A. Stefan, D. Beljonne, Y. Engelborghs, A. Herrmann, K. Mullen, F. C. De Schryver, and J. Hofkens. 2008. Visualization of membrane rafts using a perylene monoimide derivative and fluorescence lifetime imaging. (vol 93, pg 2877, 2007). *Biophys J* 94:715–715.

(10) Hardt, S. L. *Biophys Chem* **1979**, *10*, 239-243.

V

Simultaneous Characterization of Lateral Lipid and Prothrombin Diffusion Coefficients by z-scan Fluorescence Correlation Spectroscopy

Štefl, M., Kulakowska, A., Hof, M.
Biophysical Journal, 97(3), L1-L3, 2009

Simultaneous Characterization of Lateral Lipid and Prothrombin Diffusion Coefficients by Z-Scan Fluorescence Correlation Spectroscopy

Martin Štefl, Anna Kułakowska, and Martin Hof*
J. Heyrovský Institute of Physical Chemistry, v.v.i., Academy of Sciences of the Czech Republic, Prague, Czech Republic

ABSTRACT A new (to our knowledge) robust approach for the determination of lateral diffusion coefficients of weakly bound proteins is applied for the phosphatidylserine specific membrane interaction of bovine prothrombin. It is shown that z-scan fluorescence correlation spectroscopy in combination with pulsed interleaved dual excitation allows simultaneous monitoring of the lateral diffusion of labeled protein and phospholipids. Moreover, from the dependencies of the particle numbers on the axial sample positions at different protein concentrations phosphatidylserine-dependent equilibrium dissociation constants are derived confirming literature values. Increasing the amount of membrane-bound prothrombin retards the lateral protein and lipid diffusion, indicating coupling of both processes. The lateral diffusion coefficients of labeled lipids are considerably larger than the simultaneously determined lateral diffusion coefficients of prothrombin, which contradicts findings reported for the isolated N-terminus of prothrombin.

Received for publication 1 April 2009 and in final form 26 May 2009.

*Correspondence: hof@jh-inst.cas.cz

Several enzymatic processes involving proteins containing γ-carboxyglutamic acid residues require those proteins to be associated with negatively charged membrane surfaces. A paradigm for such processes serves the membrane binding of the blood coagulation protein prothrombin followed by lateral diffusion to the prothrombinase enzyme complex (1). Since those proteins are only weakly binding to relevant membrane surfaces (apparent equilibrium dissociation constants K_d are in the μM range) (2) at physiological protein concentrations, there is a considerable amount of unbound protein and, thus, the lateral protein diffusion coefficients are difficult to access. To our knowledge, an application of total internal reflection with fluorescence pattern photobleaching recovery (TIR/FPPR) to bovine prothrombin fragment 1 (BPF1) binding to supported lipid bilayers (SLBs) is the only successful example of the translational mobility of a protein weakly bound to a membrane surface (3).

Conventional (single-spot) fluorescence correlation spectroscopy (cFCS) has been used recently for the comparison between basic peptides' diffusion with the associated lipid diffusion (4). However, it is now accepted that, mainly due to intrinsic positioning and calibration problems, cFCS is not a reliable tool for the determination of 2-dimensional (2D) diffusion coefficients (5–7). Moreover, 2D cFCS measurements are relying on the assumption that the axial position of highest fluorescence intensity is equal to the laser waist. We have shown that this is not fulfilled when investigating plain SLBs (5). This mismatch might be even more severe when an unbound protein is contributing to the signal. The simplest way to overcome those positioning and calibration problems is the z-scan approach (5) that enables obtainment of artifact-free diffusion coefficients (6). The autocorrelation functions (ACFs) curves are acquired at well-defined axial positions. For 2D diffusion, the divergence of the laser leads to a parabolic dependence of the diffusion times and particle numbers on the distances from the membrane, whereas in the case of 3D diffusion those parameters are position independent. Analysis of the axial dependence of the diffusion times and particle numbers allows the quantitative determination of 2D diffusion coefficients and surface concentrations (5).

In this article, we show that z-scan fluorescence correlation spectroscopy is a simple alternative to the sophisticated TIR/FPPR for the determination of 2D diffusion coefficients of those weakly bound proteins. Moreover, together with pulsed interleaved excitation (PIE) (8), we are able to simultaneously monitor lipid and protein diffusion and thus obtain direct information on possible coupling of both diffusion processes. Specifically, we investigated the calcium-dependent binding of alexa633-labeled bovine prothrombin (BP) to SLBs composed of 1,2-dioleoyl-s*n*-glycero-3-phosphocholine (DOPC) and 1,2-dioleoyl-s*n*-glycero-3-phosphoserine (DOPS). The SLBs of different lipid composition were labeled by atto488-1,2-dioleoyl-s*n*-glycero-3-phosphoethanolamine (atto488-DOPE).

BP was provided from Synapse BV (Maastricht, The Netherlands) and DOPC, DOPS, and DOPE were purchased from Avanti Polar Lipids (Alabaster, AL). Alexa633 and atto488 were obtained from Invitrogen (Eugene, OR) and Attotec (Siegen, Germany), respectively. BP was covalently labeled by alexa633 via primary amines of lysine and arginine residues and then separated from free fluorescent dyes by gel

Editor: Petra Schwille.

doi: 10.1016/j.bpj.2009.05.031

filtration using Sephadex G-25 in 0.01M phosphate buffered saline (pH 7.2). DOPE was covalently labeled by atto488-NHS-ester and purified by adsorption chromatography on silica gel column (Kieselgel 60, Merck, Whitehouse Station, NJ) in chloroform/methanol/water (60/25/4) eluent. The SLBs were prepared by spreading small unilamellar vesicles (labeled/unlabeled lipid ratio 1:100,000) on freshly cleaved mica surface. Mica was attached to a holder 200 μm above the bottom of the cuvette (5). All BP (with a labeled/unlabeled ratio of 1:600) measurements were performed (10 mM Hepes buffer, 150 mM NaCl, 10 mM $CaCl_2$, pH 7.4) at 24°C on a MicroTime 200 confocal microscope (PicoQuant, Berlin, Germany). We excited by two pulsed diode lasers (LDH-P-C-470, 470 nm and LDH-P-635, 635 nm) each of which with a 32 MHz repetition rate in PIE mode, double dichroic mirror Z473/635 RPC and band-pass filters HQ 515/50, HQ 685/50 (both Omega Optical, Brattleboro, VT), and a water immersion objective (1.2 NA, 60×) were used. The low power of 5 μW was chosen to minimize photobleaching and saturation.

ACFs were acquired at axial positions spaced 0.1 μm apart. Because at each axial position membrane bound and unbound BP contribute to the signal and intersystem crossing has to be taken into account, the ACFs were fitted to

$$G(\tau) = 1 + \frac{1}{\mathrm{PN}(1-T)}\left(1 - T\left(1 - e^{-\frac{\tau}{\tau_0}}\right)\right) \cdot \left(\frac{\mathrm{FRa}}{1+\frac{\tau}{\tau_{Da}}} \cdot \frac{1}{\left(1+\frac{\tau}{\tau_{Da}}\left(\frac{w_0}{w_z}\right)^2\right)^{\frac{1}{2}}} + \frac{1-\mathrm{FRa}}{1+\frac{\tau}{\tau_{Db}}}\right), \quad (1)$$

where PN is the particle number of fluorescent molecules within the confocal volume, FRa is the percentage of bound BP molecules within the PN value, τ_{Da} and τ_{Db} are diffusion times of bound (2D) and unbound (3D) BP, respectively, w_0 and w_z are spatial parameters of the confocal volume and T and τ_0 characterize the contribution and kinetics of intersystem crossing. τ_{Db} was determined before each z-scan by focusing on the solution above the SLBs (average value 450 μs ± 10 μs) and fixed in the z-scan evaluation. The resulting dependence of τ_{Da} on the z-position was analyzed as described elsewhere (5):

$$\tau_D = \frac{w_0^2}{4D_2}\left(1 + \frac{\lambda_0^2 \Delta z^2}{\pi^2 n^2 w_0^4}\right), \quad (2)$$

where D_2 is the lateral diffusion coefficient, n is refractive index, λ is the excitation wavelength and Δz is the distance between the sample position z_0 and the position of the beam diameter minimum. Since we used two-color PIE we obtained in a single measurement z-scans for alexa633-BP and atto488-DOPE, respectively (Fig. 1). The latter data set was obtained by the standard 2D z-scan (5). The obtained parabolic z-scan dependencies confirm that we indeed are characterizing 2D processes. In fact, membrane desorption

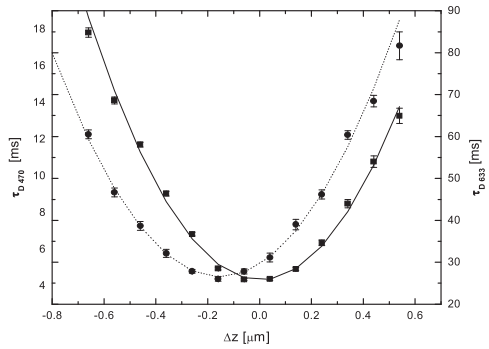

FIGURE 1 Dependence of diffusion times on the *z*-position of the focus for alexa633-BP (●; *dotted line*) and atto488-DOPE (■; *solid line*). Shown are the z-scans for 20% DOPS and 8 μM BP. The distance between the z-focus positions created by the two lasers is ~192 nm ± 19 nm.

of BP occurs on the second timescale (2) and thus does not influence the detected ACFs.

Z-scan fluorescence correlation spectroscopy was used to determine equilibrium dissociation constants (K_d) of the interaction of BP with the DOPS/DOPC SLBs. The number of bound BP molecules Q was plotted versus BP solution concentration $[P]$ and analyzed by Langmuir isotherms corrected for K_d:

$$Q = \frac{Q_{\mathrm{lim}} \times [P]}{K_d + [P]}. \quad (3)$$

The Q values were calculated from z-scan minima of PN multiplied by FRa. Q_{lim} is the limiting value of labeled BP molecules bound to the membrane. Unspecific binding was determined in presence of EDTA and subtracted from the Q values. Obtained K_d values for SLBs composed of different DOPS/DOPC ratio are summarized in Table 1 and correspond to previously published data (2,9). As shown in Table 1, K_d were higher for lower molar fractions of DOPS within the membrane. These results confirm that BP binds to membranes in a phosphatidylserine-specific manner.

Atto488-DOPE lateral diffusion coefficients D_2 were determined for SLBs composed of a different DOPS/DOPC ratio. No significant differences in D_2 were observed with the increasing DOPS content within the membrane. In the range from 0 mol % to 30 mol % DOPS, the average lipid D_2-value was 4.3 ± 0.4 $\mu m^2\ s^{-1}$ (at 10 mM $CaCl_2$). Using the described approach we could investigate a), how the DOPS content and the BP concentration influence the BP lateral diffusion, and b), how is the latter related to the lateral lipid diffusion. Our data shows that with increasing Q (i.e., with

TABLE 1 Equilibrium dissociation constants of BP for different DOPS [mol %] membrane content

	10%	15%	20%	25%	30%
K_d[μM]	4.0 ± 0.9	3.2 ± 0.3	2.6 ± 0.5	2.0 ± 0.3	0.8 ± 0.1

Errors are represented by standard deviations. Note that ~10–15 mol % DOPS and a BP concentration of 1.4 μM are physiological relevant.

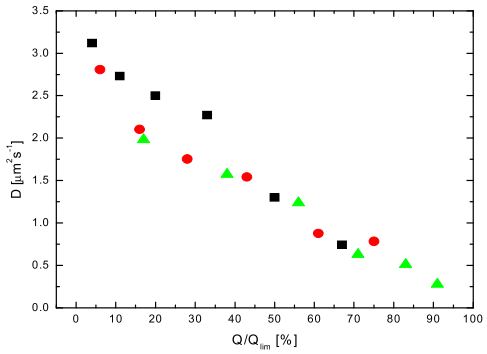

FIGURE 2 Dependence of BP lateral diffusion coefficients on the relative amount of bound BP Q/Q_{lim}. Data were determined for 10 mol % of DOPS (*black*), 20 mol % of DOPS (*red*) and 30 mol % of DOPS (*green*) containing DOPC SLBs. Q/Q_{lim} were calculated via Eq. 3 using K_d values from Table 1.

increasing amount of DOPS or BP used) protein D_2 values decrease (Fig. 2). Similar behavior was found for the BP N-terminus BPF1 missing ~75% of the molecular weight of the native BP (10). Above 30% Q/Q_{lim} the D_2 values obtained for three different DOPS contents overlap perfectly. In this range the observed dependency might be explained by a model based on bound BP molecules acting as impermeable diffusion obstacles (11). Interestingly, in the physiological relevant range ($Q/Q_{lim} < 30\%$) the BP diffusion weakly bound to 10% DOPS SLBs appears to be faster than on SLBs with higher DOPS content, indicating that at the same surface coverage the increasing amount of available DOPS headgroups is slowing down BP lateral diffusion.

Comparison of D_2 values for BP and lipids (Fig. 3) shows that BP diffuses significantly slower, which contradicts previously published TIR/FPPR data for BPF1 diffusion on SLBs claiming identical D_2 values for lipids and proteins (3). However, BP and lipid diffusion display qualitatively the same trends suggesting that both lateral diffusion processes are strongly related with each other. At low (10%) DOPS content and low BP concentration, the difference between protein and lipid diffusion is considerably smaller than at higher DOPS contents.

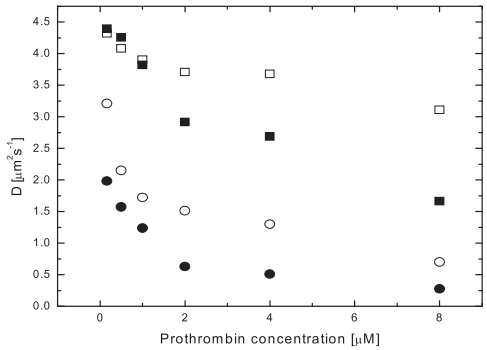

FIGURE 3 Comparison of BP (*circles*) and lipid (*squares*) D_2 values determined for membranes composed of 10 mol % of DOPS (*open symbols*) and 30 mol % of DOPS (*solid symbols*), respectively.

In summary, we found that the lateral diffusion of alexa633-BP is coupled with the diffusion of atto488-DOPE. However, BP is diffusing considerably slower than the lipids. No differences in the lateral diffusion within both layers of the used SLBs were observed (12). Thus, there is no evidence for significantly faster diffusion within the layer facing the support compared to diffusion within the lipid layer binding BP, suggesting that the reason for the difference in D_2 values between BP and lipids might be connected with the mechanism of BP diffusion. However, explanations based on hydrophobic interactions between the nonfragment part of BP and the SLBs (3,9) or a possible exchange of DOPS molecules bound to BP with unbound ones appear at that point as too speculative.

ACKNOWLEDGMENTS

We thank Dr. Aleš Benda, MSc. Radek Macháň as well as Dr. Jan Sýkora for technical support and discussions and Prof. Dr. Jiří Hudeček for his help with protein labeling.

This work has been supported by the Ministry of Education of the Czech Republic (grant LC06063; M.S., A.K.) and the Grant Agency of the Czech Republic (grant 203/08/0114; M.H.).

REFERENCES and FOOTNOTES

1. Lentz, B. R. 2003. Exposure of platelet membrane phosphatidylserine regulates blood coagulation. *Prog. Lipid Res.* 42:423–438.
2. Pearce, K. H., M. Hof, B. R. Lentz, and N. L. Thompson. 1993. Comparison of the membrane-binding kinetics of bovine prothrombin and its fragment-1. *J. Biol. Chem.* 268:22984–22991.
3. Huang, Z. P., K. H. Pearce, and N. L. Thompson. 1994. Translational diffusion of bovine prothrombin fragment 1 weakly-bound to supported planar membranes - measurement by total internal-reflection with fluorescence pattern photobleaching recovery. *Biophys. J.* 67:1754–1766.
4. Golebiewska, U., A. Gambhir, G. Hangyas-Mihalyne, I. Zaitseva, J. Radler, et al. 2006. Membrane-bound basic peptides sequester multivalent (PIP2), but not monovalent (PS), acidic lipids. *Biophys. J.* 91:588–599.
5. Benda, A., M. Benes, V. Marecek, A. Lhotsky, W. T. Hermens, et al. 2003. How to determine diffusion coefficients in planar phospholipid systems by confocal fluorescence correlation spectroscopy. *Langmuir.* 19:4120–4126.
6. Dertinger, T., V. Pacheco, I. von der Hocht, R. Hartmann, I. Gregor, et al. 2007. Two-focus fluorescence correlation spectroscopy: A new tool for accurate and absolute diffusion measurements. *ChemPhysChem.* 8:433–443.
7. Garcia-Saez, A. J., and P. Schwille. 2008. Fluorescence correlation spectroscopy for the study of membrane dynamics and protein/lipid interactions. *Methods.* 46:116–122.
8. Muller, B. K., E. Zaychikov, C. Brauchle, and D. C. Lamb. 2005. Pulsed interleaved excitation. *Biophys. J.* 89:3508–3522.
9. Cutsforth, G. A., R. N. Whitaker, B. R. Lentz, and J. Hermans. 1989. A new model to describe extrinsic protein-binding to phospholipid-membranes of varying composition - application to human coagulation proteins. *Biochemistry.* 28:7453–7461.
10. Huang, Z. P., K. H. Pearce, and N. L. Thompson. 1992. Effect of bovine prothrombin fragment-1 on the translational diffusion of phospholipids in Langmuir-Blodgett monolayers. *Biochim. Biophys. Acta.* 1112:259–265.
11. Forstner, M. B., Ch. K. Yee, A. N. Parikh, and T. Groves. 2006. Lipid lateral mobility and membrane phase structure modulation by protein binding. *J. Am. Chem. Soc.* 128:15221–15227.
12. Przybylo, M., J. Sykora, J. Humpolickova, A. Benda, A. Zan, et al. 2006. Lipid diffusion in giant unilamellar vesicles is more than 2 times faster than in supported phospholipid bilayers under identical conditions. *Langmuir.* 22:9096–9099.